# ABSTRACT

Title of thesis: ELECTROKINETIC TRANSPORT IN NANOCHANNELS GRAFTED WITH BACKBONE CHARGED POLYELECTROLYTE BRUSHES

Vishal Sankar Sivasankar

Thesis directed by: Dr. Siddhartha Das
Department of Mechanical Engineering

In this thesis, we study the electrokinetic transport in nanochannels functionalized with pH-responsive backbone charged polyelectrolyte (PE) brushes modeled using thermodynamically self-consistent augmented strong stretching theory. We investigate the electroosmotic (EOS) transport, induced by the application of external electric field, and the diffusioosmotic (DOS) transport due to applied salt concentration gradient induced electroosmotic transport in brush functionalized and brushless nanochannels with equal surface charge density. We find massive enhancement in the electrokinetic transport in PE brush functionalized nanochannels when compared to brushless nanochannels which can be ascribed to the brush induced localization of the EDL and hence the net EOS body force away from the flow retarding walls. Further, we establish that both EOS and DOS transport in nanochannels grafted with backbone charged PE brushes is larger in magnitude when compared to that in nanochannels grafted with end charged PE brushes.

# ELECTROKINETIC TRANSPORT IN NANOCHANNELS GRAFTED WITH BACKBONE CHARGED POLYELECTROLYTE BRUSHES

by

Vishal Sankar Sivasankar

Thesis submitted to the Faculty of the Graduate School of the
University of Maryland, College Park in partial fulfillment
of the requirements for the degree of
Master of Science
2020

**Advisory Committee:**
Associate Professor Amir Riaz
Assistant Professor Taylor Woehl
Associate Professor Siddhartha Das, Chair/Advisor

Time: 2:00 - 3:00 PM
Date: August 03, 2020 (Monday)

# Acknowledgments

I owe my gratitude to my advisor, Dr. Siddhartha Das, who had given me this wonderful opportunity to pursue research under his guidance. I am grateful for him, as he had always made himself available to help and encourage me during difficult times. I would also like to thank all of my lab mates who had made this transition into graduate research very conducive.

This work has been supported by the Department of Energy Office of Science grant DE-SC0017741.

## Contents

## List of Tables

## List of Figures

# List of Abbreviations

| | |
|---|---|
| AAM | Anodized Alumina membrane |
| B.C | Backbone charged |
| BN | Boron Nitride |
| COS | Chemiosmotic |
| CNT | Carbon nanotube |
| DMA | N,N-dimethylacrylamide (DMA) |
| DNA | Deoxyribonucleic acid |
| DOS | Diffusioosmotic |
| E.C | End-charged |
| EDL | Electric double layer |
| EHD | Electrohydrodynamic |
| EOS | Electroosmotic |
| EV | Excluded volume |
| GMA | glicidyl methacrylate |
| GO | Graphene oxide |
| MAPS | 3-(trimethoxysilyl) propyl methacrylate |
| MD | Molecular dynamics |
| NC | Nanochannel |
| NS | Navier-Stokes |
| PB | Poisson-Boltzmann |
| PCS | Polyelectrolyte chargeable sites |
| PE | Polyelectrolyte |
| PEO | Polyethylene oxide |
| Si | Silicon |
| SST | Strong stretching theory |

# Chapter 1: Introduction

*In this chapter, we discuss the functionalization of surfaces with polymer/polyelectrolyte (PE) brushes and its behavior under various surrounding medium. Subsequently, we review the literature for the liquid transport in such brush functionalized nanochannels. Next, the objective and motivation of this thesis is discussed. Finally, the outline of the thesis is described.*

## *1.1 Functionalization of surfaces with polymer/polyelectrolyte (PE) brushes*

Modification of surfaces by grafting polymer/polyelectrolyte brushes has emerged as an extremely promising tool fora plethora of applications. Such functionalization can be achieved by either grafting the bushes to the solid surface by direct chemical modification, or by having the polymer chains "grafted from" via polymerization reactions [1,2]. In "grafting to" technique, functional groups in the polymer molecules and the modified substrate react to form a polymer chain. In "grafting from" technique, polymerization reaction is initiated on the substrate surface with the help of an initiator [1].

The behavior of polymer chains depends on the conditions of the surrounding

medium such as the solvent quality. For a given polymer, based on the solvent quality solvents could be classified into good solvent, poor solvent, and theta solvent. A good solvent favors polymer-solvent interaction and it results in polymer chain stretching away from the substrate forming a mushroom-like structure. However, in poor solvent, polymer-solvent interactions are not energetically favorable resulting in a coil-like structure. The transition between good and poor solvent occurs at a temperature called theta temperature and the state is called theta state [1, 3].

The polymer chain behavior changes with the change in the grafting density (number of chains grafted per unit area). With sufficiently higher grafting density, the excluded volume interactions, and the elastic interactions within each chain results in the formation of brush-like configuration [4–13]. Polyelectrolyte brushes are these brushes which are charged [3]. For polyelectrolyte brushes, the electrostatic energy contributions become important and it contributes to the equilibrium brush configuration. The charge on the brush in the presence of electrolyte leads to a formation of electric double layer (EDL). This leads to additional interaction energy between the PE brush and the induced EDL. This interaction energy depends on the conditions of the surrounding medium such as the electrolyte concentration, pH of the medium. Another significant contribution for the energy of PE brush is due to the ionization of the brush molecules [12, 13]. These energy contributions determine the configuration and the electrostatics of the PE brush.

## *1.2 Liquid transport in brush functionalized nanochannels*

Liquid transport in nanofluidic system has wide range of applications across the field of fluid mechanics, chemical separation/mixing, bio-medicine, energy conversion [14, 15]. Surface modification using brush functionalizaton of nanofluidic surfaces is an effective tool in many of these applications. Most of the studies on liquid transport in polymer/PE brush grafted nanofluidic systems utilize the brushes in order to retard the liquid transport based on the understanding that the presence of brushes will invariably decreases the flow rate due to the drag force on the fluid flow imparted by the brushes. For instance, studies [16, 17] have shown a massive reduction in liquid flow in nanofluidic capillaries due to the drag force imparted by the grafted polymer. Similarly, the studies [18–20] have shown a large decrease in flow velocity in nanochannels grafted with polymer brushes. Actually, there are few studies on liquid transport in PE brush grafted nanochannels which also show a reduction in the liquid flow rate [21–29]. The framework used in these studies to model the brushes has one major shortcoming. These studies assume that the brush configuration: brush height, and monomer distribution remains independent of salt concentration and pH. However, in recent works [30–32], Das and co-workers overcome some of this limitation by accounting for the changes in the brush height with salt concentration and pH of the electrolyte and they studied the liquid transport in such brush-grafted nanochannels. They found enhancement in the liquid flow rate for sparsely brush-grafted nanochannels and reduction in the flow rate for densely grafted nanochannels. However, these studies have a significant limitation as the

brushes are modeled using Alexander-de-Gennes model which assumes an uniform monomer distribution along the brush height. This leads to overestimation of drag forces resulting in such flow reduction witnessed in densely grafted nanochannels.

## *1.3 Agenda of the thesis*

The main objective of this thesis is to provide a theoretical understanding of two types of liquid transport, namely electroosmotic (EOS) transport and diffusioosmotic (DOS) transport, in a polyelectrolyte brush functionalized nanofluidic channels. For that purpose, we first provide a thermodynamically self-consistent theoretical framework to model the PE brush. Next, we analyze and explain the underlying physics behind the massive enhancement of these liquid transport in such PE brush functionalized nanochannels.

## *1.4 Outline of the thesis*

Chapter 2 of this thesis introduces the formulation of augmented Strong Stretching theory (SST) which include the effects of excluded volume interactions and a generic mass action law. We provide a detailed procedure for obtaining the brush configuration and its electrostatics using variational minimization of free energy of PE brush molecules. Firstly, we study the effect of excluded volume interactions by varying the excluded volume parameters $\nu$ and $\omega$, which represents the "goodness" of the solvent. Subsequently, we investigate the effect of polyelectrolyte chargeable site (PCS) density on the equilibrium PE brush height, monomer distribution along

the length of the brush, and EDL electrostatic potential.

Chapter 3 of this thesis deals with the liquid transport induced by the application of external axial electric field in a nanochannel grafted with pH-responsive backbone charged PE brushes. These brushes are modeled using augmented strong stretching theory (SST) described in the chapter 2. Theoretical basis for such electrokinetic transport, known as electroosmotic transport, and its underlying physics is described in detail. Next, the equations governing the electroosmotic transport are described for both brush-grafted nanochannels and brush-free nanochannels. Following that, we provide a comparison of flow velocity, flux ratio for various brush grafting densities, and pH and concentration of the electrolyte. Subsequently, we provide an extensive comparison of flux for various nanofluidic devices of different size and materials.

Chapter 4 of this thesis deals with the ionic diffusioosmotic transport induced by the application of a salt concentration gradient across the length of the nanochannel filled with electrolyte and grafted with backbone charged pH-responsive PE brushes. These brushes are modeled using augmented strong stretching theory (SST) described in the chapter 2. Theoretical background and the governing equations for the salt concentration gradient based diffusioosmotic flow are explained in detail. Following that we provide a detailed comparison of the DOS induced electric field and its components, ionic and osmotic electric field, for various brush grafting density, and electrolyte pH and concentration. Subsequently, the DOS velocity for various brush-grafted cases and its corresponding brushless cases are compared.

# Chapter 2: Revisiting the strong stretching theory for pH-responsive polyelectrolyte brushes: effects of consideration of excluded volume interactions and an expanded form of the mass action law

*In this chapter*[1]*, we develop a theory to account for the effect of the excluded volume (EV) interactions in the Strong Stretching Theory (SST) based description of the pH-responsive polyelectrolyte (PE) brushes. The existing studies have considered the PE brushes to be present in a $\theta$-solvent and hence have neglected the EV interactions; however, such a consideration cannot describe the situations where the pH-responsive brushes are in a "good" solvent. Secondly, we consider a more expanded form of the mass action law, governing the pH-dependent ionization of the PE molecules, in the SST description of the PE brushes. This expanded form of the mass action law considers different values of $\gamma a^3$ ($\gamma$ is the density of the charge-*

[1] This work was primarily carried out by H. S. Sachar, a Ph.D candidate in the group. Contents of this chapter have been published as: *H. S. Sachar, V. S. Sivasankar, and S. Das, "Revisiting the strong stretching theory for pH-responsive polyelectrolyte brushes: effects of consideration of excluded volume interactions and an expanded form of the mass action law", Soft matter, 15(4), 559-574 (2019).*

*able sites on the PE molecule and a is the PE Kuhn length) and therefore is an improvement over the existing SST models of PE brushes as well as other theories involving pH-responsive PE molecules that always consider* $\gamma a^3 = 1$. *Our results demonstrate that the EV effects enhance the brush height by inducing additional PE inter-segmental repulsion. Similarly, the consideration of the expanded form of the mass action law would lead to a reduced (enhanced) brush height for* $\gamma a^3 < 1$ *(*$\gamma a^3 > 1$*). We also quantify the variables such as the monomer density distribution, distribution of the ends of the PE brush, and the EDL electrostatic potential and explain their differences with respect to those obtained with no EV interactions or* $\gamma a^3 = 1$.

## 2.1 Introduction

Grafting charged, polyelectrolyte (PE) brushes on solid-liquid interfaces have proven to be an excellent way of functionalizing such interfaces for applications such as nanofluidic ion and biosensing [33–37], fabrication of nanofluidic diodes [38,39], current rectifiers [40], and nano-actuators [41], designing surfaces of desired wettability [42], engineering nanoparticles for targeted drug delivery [43], oil recovery [44], and many more. The key to several of these applications is the responsiveness of these brushes to environmental cues (e.g., a change in pH or a change in salt concentration) – as a response to these cues, the PE brushes undergo a change in some of its properties (e.g., configuration, height, etc.) thereby enabling most of these above applications. pH-responsive (or annealed) PE brushes refer to brushes

whose ionization and hence the charging depends on the local pH [22,25,45–47]. For example, poly(meth)acrylic brush is an example of a pH-responsive anionic brush. On the other hand, there are brushes (also known as quenched brushes) whose degree of ionization and hence the charging is independent of pH (e.g., partially sulfonated polystyrene brushes). The purpose of this paper is to provide a detailed thermodynamic self-consistent theoretical model for quantifying such pH-responsive PE brushes.

PE brushes have been modelled extensively. For example, there have been significant efforts aimed at developing scaling laws by balancing the different energies (elastic, electrostatic, and excluded volume) and yielded the brush height as scaled functions of variables such as the grafting density and charge density of the brushes, number of monomers, and the concentration of the added salt [48–55]. Subsequently, a more involved calculation procedure was also attempted where the electrostatics of the induced electric double layer (EDL) was described using the Poisson-Boltzmann (PB) equation [21,30,31,46,47,56–58]. Such studies varied in complexity and rigour depending on the manner in which the monomer interactions were described – there have been several approaches ranging from the use of simple Alexander-de-Gennes model [21,30,31,57] to a more involved parabolic model [56,58] for the brushes. The most complete analytically tractable approach till date, however, has been proposed in a series of seminal papers that employed the Strong Stretching Theory (SST) to describe the PE brushes while the resulting EDL electrostatics was described by the classical PB equation [45,59–62].

The same self-consistent SST and the PB equation have also been employed

to study the configuration of the pH-responsive PE brushes [45]. This study is the state-of-the-art in the SST calculation of the pH-responsive PE brushes. However, this paper considers the PE brushes to be in a $\theta$-solvent and hence neglects all the possible excluded volume (EV) interactions. On the other hand, a vast number of experimental studies involving pH-responsive PE brushes invariably consider the solvent to be a "good" solvent (i.e., a solvent that makes the considerations of the EV interactions between the segments of the PE molecule mandatory) with respect to the PE brush [63–70]. Obviously, for such problems, the theory of Ref. [45] will be inadequate. In order to fill this void, in this paper, we modify the SST for the pH-responsive PE brushes by accounting for the EV interactions between the PE brush segments. Therefore, this study is the first study for the SST of the pH-responsive PE brushes accounting for the effect of the EV interactions. EV interactions have been considered for other theoretical calculations of the PE brushes [71–73], but not in this SST framework used to quantify the behavior of the pH-responsive PE brushes. As a second improvement to the SST model of the pH-responsive PE brushes, we consider a more expanded form of the mass action law for the pH-dependent ionization of the PE molecules valid for all values of $\gamma a^3$ ($\gamma$ is the density of the chargeable sites on the PE molecule and $a$ is the PE Kuhn length) and study the effect of this more expanded form of the mass action law in the SST calculations of PE brushes. Both Ref. [45] as well as other papers describing the pH-responsive PE molecules (not necessarily PE "brushes") [74–78] have considered only a special form of the mass action law where $\gamma a^3 = 1$. Our calculations, therefore, ensure a more generic description of the pH-responsive PE brushes within the general ambit

of the SST model.

Our results demonstrate distinct contributions of the EV interactions and the expanded form of the mass action law in the SST description of the PE brushes. Consideration of the EV interactions imply consideration of additional inter-segmental repulsion for a particular PE brush molecule. Accordingly, the EV effect enhances the brush height. This enhancement is most magnified for large salt concentration (which leads to an enhanced screening of the PE brush charges) and small $pH_\infty$ (i.e., a large bulk $H^+$ ion concentration that weakens the ionization of the brushes). On the other hand, consideration of the generic mass action law implies that one witnesses a decrease (increase) of the PE brush height for $\gamma a^3 < 1$ ($\gamma a^3 > 1$) owing to a reduced (enhanced) charge density of the PE brushes causing a reduced (enhanced) counterion-induced brush swelling [79–81]. We complete the description of the problem by accounting for the effects of the EV interactions and the expanded form of the mass action law in dictating the monomer density distribution, distribution of the end location of the PE brushes, and the EDL electrostatics. In summary, our paper establishes the theory for a much more generic SST-based description of the pH-responsive PE brushes and the resultant EDL electrostatics.

## *2.2 Self-Consistent Field Approach*

### *2.2.1 Free Energy Equations*

We consider a rigid, impenetrable substrate grafted with pH-responsive, weakly poly-acidic (anionic) PE brushes immersed in an electrolyte solution (see Fig. 1).

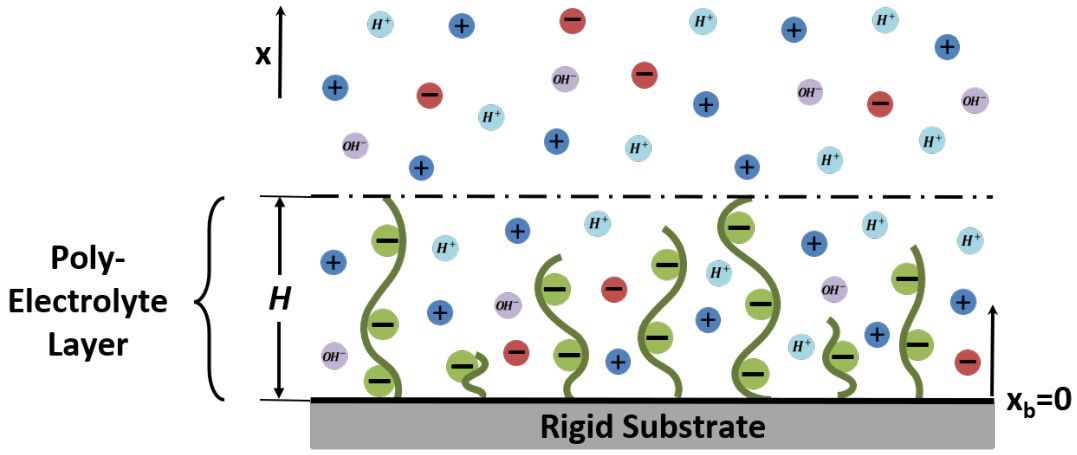


*Fig. 2.1:* Schematic showing the pH-responsive PE brush layer.

The separation between adjacent grafted PE molecules $\ell$ is assumed to be small enough such that the system attains a brush like configuration. Here we would discuss the free energies that dictate the brush equilibrium in a self-consistent field approach. These equations have already been discussed by several previous papers [45, 59, 71]; we repeat them here for the sake of continuity.

The net free energy functional ($F$) of a given PE molecule can be expressed as:

$$\frac{F}{k_BT} = \frac{F_{els}}{k_BT} + \frac{F_{EV}}{k_BT} + \frac{F_{elec}}{k_BT} + \frac{F_{EDL}}{k_BT} + \frac{F_{ion}}{k_BT}, \tag{2.1}$$

where $F_{els}$, $F_{EV}$, $F_{elec}$, $F_{EDL}$ and $F_{ion}$ are the elastic (entropic), excluded volume, electrostatic, electric double layer and ionization contributions to the free energy (per PE molecule) respectively.

In this model, the equilibrium brush height $H$ (to be determined self-consistently

later) refers to the maximum distance of the monomers of the PE brush from the substrate. In order to express the free energy, the system is divided into two regions: region 1 ($0 \leq x \leq H$) forms the interior of the brush and comprises of all the PE chains whereas the region 2 ($H \leq x \leq \infty$) lies exterior to the brush. We consider the case where the electrostatic repulsion between the charged monomers is large enough to ensure that the brush is in a strongly stretched configuration. Therefore this free energy description is the same as the *Strong Stretching Theory* description of the PE brushes.

Following the notation of Zhulina et al. [71], we write:

$$\frac{F_{els}}{k_B T} = \frac{3}{2pa^2} \int_0^H g(x')dx' \int_0^{x'} E(x, x')dx, \tag{2.2}$$

$$\frac{F_{EV}}{k_B T} = \frac{\sigma}{a^3} \int_0^H f_{conc}[\phi(x)]dx, \tag{2.3}$$

where $p$ is the chain rigidity, $a$ is the Kuhn length, and $\sigma \sim \ell^2$ is the grafted area per chain. Also, $E(x, x') = \frac{dx}{dn}$ is the local stretching at a distance $x$ from the surface for a chain whose end is located at a distance of $x'$. Furthermore, g($x'$) is the normalized chain end distribution function, such that

$$\int_0^H g(x')dx' = 1. \tag{2.4}$$

Finally, $\phi(x)$ is the dimensionless monomer distribution profile of a given PE chain and $f_{conc}[\phi(x)]$ is the non-dimensionalized per unit-volume free energy for the excluded volume interactions.

Following [47], $F_{elec} + F_{EDL}$ can be expressed as:

$$\begin{aligned}\frac{F_{elec}}{k_BT} + \frac{F_{EDL}}{k_BT} =& \frac{\sigma}{k_BT}\int_0^\infty \Big[ -\frac{\epsilon_0\epsilon_r}{2}\left|\frac{d\psi}{dx}\right|^2 + e\psi(n_+ - n_- + n_{H^+} - n_{OH^-})\Big]dx \\ &- \frac{\sigma}{k_BT}\int_0^H \Big[e\psi n_{A^-}\phi\Big]dx + \\ &\sigma\int_0^\infty \Big[n_+\Big(ln\Big(\frac{n_+}{n_{+,\infty}}\Big) - 1\Big) + n_-\Big(ln\Big(\frac{n_-}{n_{-,\infty}}\Big) - 1\Big) + n_{H^+}\Big(ln\Big(\frac{n_{H^+}}{n_{H^+,\infty}}\Big) - 1\Big) \\ &+ n_{OH^-}\Big(ln\Big(\frac{n_{OH^-}}{n_{OH^-,\infty}}\Big) - 1\Big) + (n_{+,\infty} + n_{-,\infty} + n_{H^+,\infty} + n_{OH^-,\infty})\Big]dx\end{aligned} \tag{2.5}$$

where $\psi$ is the electrostatic potential, $n_i$ is the number density of the ion $i$ [where $i = \pm, H^+, OH^-$], $n_{i,\infty}$ is the bulk number density of the ion $i$, $n_{A^-}$ is the local number density of the $A^-$ ion, $e$ is the electronic charge, $k_BT$ is the thermal energy, $\epsilon_0$ is the permittivity of free space, and $\epsilon_r$ is the relative permittivity of the solution.

The PE brush ionizes via dissociation of an acid $HA$ producing $H^+$ and $A^-$ ions. $n_{A^-}$ is a function of the hydrogen ion concentration ($n_{H^+}$) as given by the expanded form of the mass action law (see the derivation later).

Following [45], $F_{ion}$ can be expressed as:

$$\begin{aligned}&\frac{F_{ion}}{k_BT} = \frac{\sigma}{a^3}\int_0^H \phi\Bigg[\Big(1 - \frac{n_{A^-}}{\gamma}\Big)ln\Big(1 - \frac{n_{A^-}}{\gamma}\Big) + \frac{n_{A^-}}{\gamma}ln\Big(\frac{n_{A^-}}{\gamma}\Big) \\ &+ \frac{n_{A^-}}{\gamma}\Big(\frac{\mu^0_{H^+} + \mu^0_{A^-} - \mu^0_{AH}}{k_BT} + ln(c_{H^+,\infty})\Big)\Bigg]dx \\ \implies &\frac{F_{ion}}{k_BT} = \frac{\sigma}{a^3}\int_0^H \phi\Bigg[\Big(1 - \frac{n_{A^-}}{\gamma}\Big)ln\Big(1 - \frac{n_{A^-}}{\gamma}\Big) + \frac{n_{A^-}}{\gamma}ln\Big(\frac{n_{A^-}}{\gamma}\Big) + \frac{n_{A^-}}{\gamma}ln\Big(\frac{n_{H^+,\infty}}{K'_a}\Big)\Bigg]dx\end{aligned} \tag{2.6}$$

where $K'_a = 10^3 N_A K_a$, $N_A$ is the Avogadro number and $K_a$ is the ionization constant of the reaction $HA \rightarrow H^+ + A^-$. Also $K_a = \exp\Big(-\frac{\mu^0_{H^+}+\mu^0_{A^-}-\mu^0_{AH}}{k_B T}\Big)$, where $\mu^0_i$ represents the standard chemical potential of species i. $n_{H^+,\infty} = 10^3 N_A c_{H^+,\infty}$ and $\gamma$ $(1/m^3)$ is the maximum density of polyelectrolyte chargeable sites (PCS).

Substituting eqs.(2.2,2.3,2.5,2.6) in eq.(2.1), $F$ can be written as:

$$\begin{aligned}\frac{F}{k_B T} =& \frac{3}{2pa^2}\int_0^H g(x')dx' \int_0^{x'} E(x,x')dx + \frac{\sigma}{a^3}\int_0^H f_{conc}[\phi(x)]dx + \frac{\sigma}{k_B T}\int_0^\infty \Big[-\frac{\epsilon_0\epsilon_r}{2}\Big|\frac{d\psi}{dx}\Big|^2 \\ &+ e\psi(n_+ - n_- + n_{H^+} - n_{OH^-})\Big]dx - \frac{\sigma}{k_B T}\int_0^H \Big[e\psi n_{A^-}\phi\Big]dx \\ &+ \sigma\int_0^\infty \Big[n_+\Big(ln\Big(\frac{n_+}{n_{+,\infty}}\Big)-1\Big) + n_-\Big(ln\Big(\frac{n_-}{n_{-,\infty}}\Big)-1\Big) + n_{H^+}\Big(ln\Big(\frac{n_{H^+}}{n_{H^+,\infty}}\Big)-1\Big) \\ &+ n_{OH^-}\Big(ln\Big(\frac{n_{OH^-}}{n_{OH^-,\infty}}\Big)-1\Big) + (n_{+,\infty}+n_{-,\infty}+n_{H^+,\infty}+n_{OH^-,\infty})\Big]dx \\ &+ \frac{\sigma}{a^3}\int_0^H \phi\Bigg[\Big(1-\frac{n_{A^-}}{\gamma}\Big)ln\Big(1-\frac{n_{A^-}}{\gamma}\Big) + \frac{n_{A^-}}{\gamma}ln\Big(\frac{n_{A^-}}{\gamma}\Big) + \frac{n_{A^-}}{\gamma}ln\Big(\frac{n_{H^+,\infty}}{K'_a}\Big)\Bigg]dx\end{aligned} \tag{2.7}$$

This energy needs to be minimized in presence of the following conditions (constraints):

$$N = \int_0^{x'} \frac{dx}{E(x,x')}, \tag{2.8}$$

$$N = \frac{\sigma}{a^3}\int_0^H \phi(x)dx, \tag{2.9}$$

where $N$ is the number of monomers per chain.

Also $\phi$(x) is related to the functions $g$ and $E$ as:

$$\phi(x) = \frac{a^3}{\sigma}\int_x^H \frac{g(x')dx'}{E(x,x')}. \tag{2.10}$$

Accounting for the constraints, the elastic component of free energy can be expressed in terms of Lagrange multipliers [$\lambda_1$ and $\lambda_2(x')$] as:

$$\begin{aligned}\frac{F'_{els}}{k_BT} =& \frac{3}{2pa^2}\int_0^H g(x')dx' \int_0^{x'} E(x,x')dx + \lambda_1\Big[\frac{\sigma}{a^3}\int_0^H \phi(x)dx - N\Big] \\ &+ \int_0^H \lambda_2(x')dx'\Big[\int_0^{x'} \frac{dx}{E(x,x')} - N\Big].\end{aligned} \tag{2.11}$$

Therefore, the net free energy ($F'$) accounting for all the constraints is:

$$\frac{F'}{k_BT} = \frac{F'_{els}}{k_BT} + \frac{F_{EV}}{k_BT} + \frac{F_{elec}}{k_BT} + \frac{F_{EDL}}{k_BT} + \frac{F_{ion}}{k_BT} \tag{2.12}$$

### *2.2.2 Variational Formalism*

We would like to obtain the governing equations dictating the problem by carrying a variational minimization of eq.(2.12). Variation of eq.(2.12), i.e.,

$$\frac{\delta F'}{k_BT} = \frac{\delta F'_{els}}{k_BT} + \frac{\delta F_{EV}}{k_BT} + \frac{\delta F_{elec}}{k_BT} + \frac{\delta F_{EDL}}{k_BT} + \frac{\delta F_{ion}}{k_BT} = 0. \tag{2.13}$$

The condition $\delta F'$=0 leads to the following equations (see appendix A for the detailed derivation), which stem from the fact that $\delta E(x,x') \neq 0$, $\delta g(x') \neq 0$, $\delta\psi \neq 0$, $\delta n_{A^-} \neq 0$, $\delta n_{\pm} \neq 0$, $\delta n_{H^+} \neq 0$, $\delta n_{OH^-} \neq 0$:

$$\begin{aligned}&\frac{3g(x')}{2a^2} - \frac{\lambda_2(x')}{E^2(x,x')} - \Bigg(\frac{\delta f_{conc}}{\delta\phi} + \lambda_1 - \frac{ea^3\psi}{k_BT}n_{A^-} + \Big(1-\frac{n_{A^-}}{\gamma}\Big)ln\Big(1-\frac{n_{A^-}}{\gamma}\Big) \\ &+ \frac{n_{A^-}}{\gamma}ln\Big(\frac{n_{A^-}}{\gamma}\Big) + \frac{n_{A^-}}{\gamma}ln\Big(\frac{n_{H^+,\infty}}{K'_a}\Big)\Bigg)\frac{g(x')}{E^2(x,x')} = 0,\end{aligned} \tag{2.14}$$

$$\int_0^{x'}\left[\frac{3E(x,x')}{2a^2}+\left(\frac{\delta f_{conc}}{\delta\phi}+\lambda_1-\frac{ea^3\psi}{k_BT}n_{A^-}+\Big(1-\frac{n_{A^-}}{\gamma}\Big)ln\Big(1-\frac{n_{A^-}}{\gamma}\Big)+\frac{n_{A^-}}{\gamma}ln\Big(\frac{n_{A^-}}{\gamma}\Big)\right.\right.$$
$$\left.\left.+\frac{n_{A^-}}{\gamma}ln\Big(\frac{n_{H^+,\infty}}{K'_a}\Big)\right)\frac{1}{E(x,x')}\right]dx=0, \tag{2.15}$$

$$-\gamma a^3\frac{e\psi}{k_BT}-ln\Big(1-\frac{n_{A^-}}{\gamma}\Big)+ln\Big(\frac{n_{A^-}}{\gamma}\Big)+ln\Big(\frac{n_{H^+,\infty}}{K'_a}\Big)=0$$
$$\implies n_{A^-}=\frac{K'_a\gamma}{K'_a+n_{H^+,\infty}\exp\big(-\gamma a^3\frac{e\psi}{k_BT}\big)} \tag{2.16}$$

$$\epsilon_0\epsilon_r\Big(\frac{d^2\psi}{dx^2}\Big)+e\Big(n_+-n_-+n_{H^+}-n_{OH^-}-n_{A^-}\phi\Big)=0 \qquad (0\le x\le H)$$
$$\epsilon_0\epsilon_r\Big(\frac{d^2\psi}{dx^2}\Big)+e(n_+-n_-+n_{H^+}-n_{OH^-})=0 \qquad (H\le x\le\infty), \tag{2.17}$$

$$n_\pm=n_{\pm,\infty}exp\Big(\mp\frac{e\psi}{k_BT}\Big), \tag{2.18}$$

$$n_{H^+}=n_{H^+,\infty}exp\Big(-\frac{e\psi}{k_BT}\Big), \tag{2.19}$$

$$n_{OH^-}=n_{OH^-,\infty}exp\Big(\frac{e\psi}{k_BT}\Big), \tag{2.20}$$

Eq. (2.16) is the expanded form of the mass action law that we shall use here. On the other hand, all the existing studies have invariably considered $\gamma = 1/a^3$ and accordingly, have considered a form of the mass action law expressed as [45]:

$$n_{A^-}=\frac{K'_a\gamma}{K'_a+n_{H^+,\infty}\exp\big(-\frac{e\psi}{k_BT}\big)}. \tag{2.21}$$

This study, therefore, will reveal for the first time the effect of consideration of the mass action law in dictating the strong stretching behavior of the pH-responsive PE brushes.

Now, from eq.(2.14), we get:

$$E(x,x')=\sqrt{U_1(x')-U_2(x)}, \tag{2.22}$$

where

$$U_1(x') = \frac{2a^2}{3}\frac{\lambda_2(x')}{g(x')}, \tag{2.23}$$

$$U_2(x) = \frac{2a^2}{3}\Bigg( - \frac{\delta f_{conc}}{\delta\phi} - \lambda_1 + \frac{ea^3\psi}{k_BT}n_{A^-} - \Big(1 - \frac{n_{A^-}}{\gamma}\Big)ln\Big(1 - \frac{n_{A^-}}{\gamma}\Big) - \frac{n_{A^-}}{\gamma}ln\Big(\frac{n_{A^-}}{\gamma}\Big) - \frac{n_{A^-}}{\gamma}ln\Big(\frac{n_{H^+,\infty}}{K_a'}\Big)\Bigg). \tag{2.24}$$

Since there is no extension at the brush ends, $E(x,x) = 0$. Therefore, $U_1(x) = U_2(x) = U(x)$. Hence,

$$E(x,x') = \sqrt{U(x') - U(x)}. \tag{2.25}$$

The normalization condition of eq.(2.8) serves as an integral equation for $U(x')$. One can check that this integral equation is satisfied if:

$$U(x) = \frac{\pi^2 x^2}{4N^2} \tag{2.26}$$

Consequently,

$$E(x,x') = \frac{\pi}{2N}\sqrt{x'^2 - x^2}. \tag{2.27}$$

Now we can re-write eq.(2.15) as:

$$\int_0^{x'} \Big[E(x,x') - \frac{U(x)}{E(x,x')}\Big]dx = 0. \tag{2.28}$$

Eq.(2.28) is equally satisfied with these stated forms of $U(x)$ and $E(x,x')$. To obtain $\phi(x)$ we can employ eq.(2.24), but prior to that we would need the functional dependence of $f$ on $\phi$. Considering the virial expansion for the non-dimensionalised per-unit volume free energy of volume interactions, we can write [71]:

$$f_{conc}[\phi(x)] \approx \nu\phi^2 + \omega\phi^3 + ..., \tag{2.29}$$

where $\nu$ and $\omega$ are the virial coefficients.

Considering the first two terms of the expansion of $f_{conc}[\phi(x)]$, we can use eq. (2.24) to obtain $\phi(x)$ in terms of $\psi(x)$ by solving a quadratic equation:

$$\begin{aligned}\phi(x) =&\frac{\nu}{3\omega}\Bigg[\Bigg\{1+\kappa^2\Bigg(\lambda - x^2 + \beta\frac{K_a'\gamma}{K_a' + n_{H^+,\infty}\exp\big(-\gamma a^3\frac{e\psi}{k_BT}\big)}\psi \\ &-\rho\Big(1-\frac{K_a'}{K_a' + n_{H^+,\infty}\exp\big(-\gamma a^3\frac{e\psi}{k_BT}\big)}\Big)ln\Big(1-\frac{K_a'}{K_a' + n_{H^+,\infty}\exp\big(-\gamma a^3\frac{e\psi}{k_BT}\big)}\Big) \\ &-\rho\frac{K_a'}{K_a' + n_{H^+,\infty}\exp\big(-\gamma a^3\frac{e\psi}{k_BT}\big)}ln\Big(\frac{K_a'}{K_a' + n_{H^+,\infty}\exp\big(-\gamma a^3\frac{e\psi}{k_BT}\big)}\Big) \\ &-\rho\frac{K_a'}{K_a' + n_{H^+,\infty}\exp\big(-\gamma a^3\frac{e\psi}{k_BT}\big)}ln\Big(\frac{n_{H^+,\infty}}{K_a'}\Big)\Bigg)\Bigg\}^{1/2} - 1\Bigg],\end{aligned} \tag{2.30}$$

where,

$$\kappa^2 = \frac{9\pi^2\omega}{8N^2a^2\nu^2}, \tag{2.31}$$

$$\rho = \frac{8a^2N^2}{3\pi^2}, \tag{2.32}$$

$$\lambda = -\lambda_1\rho = -\lambda_1\frac{8a^2N^2}{3\pi^2}, \tag{2.33}$$

$$\beta = \frac{8N^2ea^5}{3\pi^2k_BT}. \tag{2.34}$$

Using eqs. (2.16), (2.18), (2.19), (2.20) and (2.30), we can re-write the equations

governing $\psi$ as:

$$\epsilon_0\epsilon_r\Big(\frac{d^2\psi}{dx^2}\Big)+e\Bigg(n_{+,\infty}\exp\Big(-\frac{e\psi}{k_BT}\Big)-n_{-,\infty}\exp\Big(\frac{e\psi}{k_BT}\Big)+n_{H^+,\infty}\exp\Big(-\frac{e\psi}{k_BT}\Big)$$
$$-n_{OH^-,\infty}exp\Big(\frac{e\psi}{k_BT}\Big)-\frac{K_a'\gamma}{K_a'+n_{H^+,\infty}\exp\big(-\gamma a^3\frac{e\psi}{k_BT}\big)}$$
$$\frac{\nu}{3\omega}\Bigg[\Bigg\{1+\kappa^2\Bigg(\lambda-x^2+\beta\frac{K_a'\gamma}{K_a'+n_{H^+,\infty}\exp\big(-\gamma a^3\frac{e\psi}{k_BT}\big)}\psi$$
$$-\rho\Big(1-\frac{K_a'}{K_a'+n_{H^+,\infty}\exp\big(-\gamma a^3\frac{e\psi}{k_BT}\big)}\Big)ln\Big(1-\frac{K_a'}{K_a'+n_{H^+,\infty}\exp\big(-\gamma a^3\frac{e\psi}{k_BT}\big)}\Big)$$
$$-\rho\frac{K_a'}{K_a'+n_{H^+,\infty}\exp\big(-\gamma a^3\frac{e\psi}{k_BT}\big)}ln\Big(\frac{K_a'}{K_a'+n_{H^+,\infty}\exp\big(-\gamma a^3\frac{e\psi}{k_BT}\big)}\Big)$$
$$-\rho\frac{K_a'}{K_a'+n_{H^+,\infty}\exp\big(-\gamma a^3\frac{e\psi}{k_BT}\big)}ln\Big(\frac{n_{H^+,\infty}}{K_a'}\Big)\Bigg)\Bigg\}^{1/2}-1\Bigg]\Bigg)=0 \qquad (0\le x\le H),$$

$$\epsilon_0\epsilon_r\Big(\frac{d^2\psi}{dx^2}\Big)+e\Bigg(n_{+,\infty}\exp\Big(-\frac{e\psi}{k_BT}\Big)-n_{-,\infty}\exp\Big(\frac{e\psi}{k_BT}\Big)+n_{H^+,\infty}\exp\Big(-\frac{e\psi}{k_BT}\Big)$$
$$-n_{OH^-,\infty}\exp\Big(\frac{e\psi}{k_BT}\Big)\Bigg)=0 \qquad (H\le x\le\infty). \tag{2.35}$$

Eqs.(29,35) establish that the equations governing the monomer distribution and the EDL electrostatic potential involve the parameters ($\nu$, $\omega$) dictating the excluded volume interactions enabling for the first time the inclusion of the excluded volume interactions in the SST description of the pH-responsive PE brushes. As has been already discussed, the state of the art SST invariably neglect the EV effects, i.e., consider the brushes to be always in a $\theta$-solvent, which might be scenario far from reality.

The boundary conditions for solving $\psi$ are:

$$(\psi)_{x=H^-} = (\psi)_{x=H^+},\ \left(\frac{d\psi}{dx}\right)_{x=H^-} = \left(\frac{d\psi}{dx}\right)_{x=H^+},\ \left(\frac{d\psi}{dx}\right)_{x=0} = 0,\ (\psi)_{x\to\infty} = 0. \tag{2.36}$$

From eq.(2.35) we can solve for $\psi$ for a given H, provided we know $\lambda$. $\lambda$ is obtained by using the normalization condition provided by eq.(2.9). In other words, we shall need to solve eqs.(2.35,2.9) simultaneously, as well as employ eq.(2.30) to obtain $\phi$, $\psi$ and $\lambda$. Now that we have $\phi(x)$, $\psi(x)$, $n_{A^-}(\psi)$, $n_\pm = n_\pm(\psi)$, $n_{H^+} = n_{H^+}(\psi)$, $n_{OH^-} = n_{OH^-}(\psi)$ we can obtain the net unbalanced charge ($q_{net}$) in the system as a function of H.

$$q_{net} = e\sigma \int_0^\infty (n_+ - n_- + n_{H^+} - n_{OH^-} - \phi n_{A^-})dx \tag{2.37}$$

In order to obtain the equilibrium brush height H, which is $H_0$, we will obtain the resulting equation (in terms of $H_0$) by writing:

$$\left(q_{net}\right)_{H=H_0} = 0 \tag{2.38}$$

Finally, we can obtain g($x$) by inverting the integral equation provided by eq.(2.10) in presence of eq.(2.27) as:

$$g(x) = \frac{x\sigma}{Na^3}\left[\frac{\phi(H)}{\sqrt{H^2 - x^2}} - \int_x^H \frac{d\phi(x')}{dx'}\frac{dx'}{\sqrt{x'^2 - x^2}}\right] \tag{2.39}$$

## 2.3 Results

### 2.3.1 Effects of consideration of excluded volume interactions

The state-of-the-art SST calculations for describing the pH-responsive PE brushes neglect the EV interactions, i.e., assume that the brushes are in a $\theta$-solvent. However, a more generic consideration must account for the possibilities that the brushes might be present in a "good" solvent, so that there is a finite EV interactions between brush segments. In the present case, we account for such a generic consideration and consider varying extent of the "goodness" of the solvent, quantified by the different values of the parameters $\nu$ and $\omega$. For simplicity, we define a given solvent using different values of $\nu$ and a given value of $\omega$. Obviously, the results corresponding to $\nu = 0$ ,$\omega = 0$ represent the case of the $\theta$-solvent [45].

In Fig. 2(a), we elucidate the variation of the brush height as a function of the extent of the EV interactions (quantified by different values of $\nu$ and a given value of $\omega$). Larger EV interactions, characterized by larger values of $\nu$ and $\omega$, would enforce a larger separation between the segments of the PE brushes, and accordingly lead to a larger value of the brush height [see Fig. 2(a)]. Of course, the case of $\nu = 0,\ \omega = 0$ is the case where the EV interactions have been ignored. We have checked that the results $\nu = 0,\ \omega = 0$ from our calculations is exactly identical to that obtained by Zhulina and Borisov [45], who consider a $\theta$-solvent (no EV interactions). An increase in the salt concentration reduces the brush height for all the values of $\nu$ and $\omega$. A larger salt concentration leads to a smaller EDL

thickness and hence there is a screening of the electrostatic repulsion over much shorter distance, eventually reducing the brush height with the salt concentration, as has been revealed previously [21, 54]. On the other hand, a larger $pH_\infty$ or a smaller value of bulk $H^+$ ion concentration leads to a stronger ionization reaction (i.e., there is an enhancement of the reaction that produces $H^+$ ions) and hence a larger charge of the PE brushes ensuring a larger counterion-induced osmotic swelling [79–81] causing to a larger brush height for all values of $\nu$ and $\omega$. The relative contribution of the EV interactions in altering the brush height (quantified by the ratio $\Delta H_0/H_0$) has been probed in Fig. 2(b). We find that the maximum percentage difference occurs for the case of larger salt concentration and smaller $pH_\infty$. Larger salt concentration (or a smaller EDL thickness) and smaller $pH_\infty$ (or a larger $H^+$ ion concentration leading to a weakened PE ionization) ensure weakened charging of the PE brushes and hence weakened counterion-induced osmotic swelling of the brushes. Under such circumstances, therefore, the relative contribution of the EV-interactions (and the resulting inter segment repulsions) in enhancing the brush height becomes more important as reflected by the larger values of $\Delta H_0/H_0$ for such concentration and $pH_\infty$ values. This is the first key finding of the paper: the EV interactions, neglected in all previous studies of SST for pH-responsive PE brushes [45], become extremely important in dictating the brush height for large salt concentration and small $pH_\infty$ values.

Fig. 3 provides the variation of the monomer distribution ($\phi$) along the brush height modelled considering finite EV interactions of varying magnitude (quantified by different values of $\nu$ and a given value of $\omega$) and no EV interactions (i.e.,

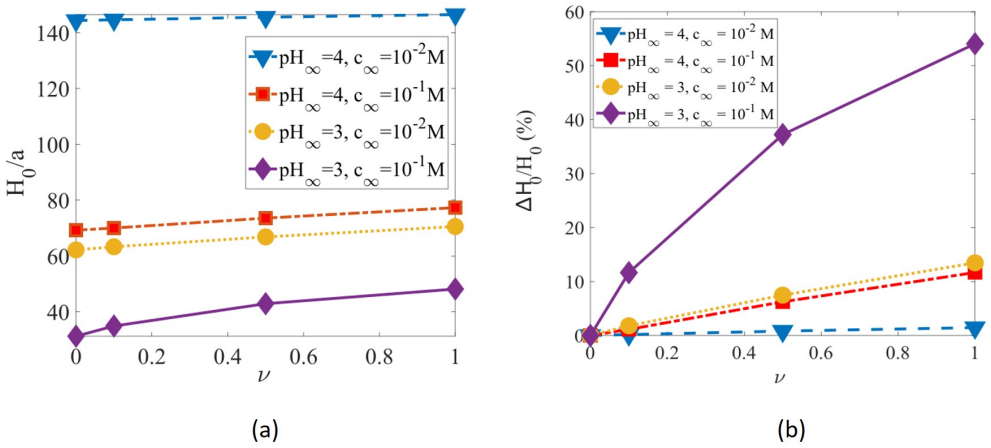


*Fig. 2.2:* Variation of (a) non-dimensional equilibrium brush height $H_0/a$ ($a$ is the PE Kuhn length) and (b) percentage increase in equilibrium brush height $\Delta H_0/H_0$ (where $\Delta H_0 = H_0 - H_{0,\nu=0,\omega=0}$) with the first virial coefficient $\nu$ for different $pH_\infty$ and $c_\infty$ values. The case of Ref. [45] is the one where $\nu = 0,\ \omega = 0$ – we recover exactly the results of Ref. [45] when $\nu = 0,\ \omega = 0$. Other parameters for this figure are $\omega = 0.1$, $pK_a = 3.5$, $a = 1nm$, $\gamma = 1/a^3$ (1 PCS per kuhn monomer), $N = 662$, $\ell = 40nm$, $k_B = 1.38 \times 10^{-23} J/K$, $T = 298K$, $e = 1.6 \times 10^{-19} C$, $\epsilon_0 = 8.854 \times 10^{-12} F/m$, $\epsilon_r = 79.8$, $pK_w = 14$, $pOH_\infty = pK_w - pH_\infty$, $c_{+,\infty} = c_\infty$, $c_{H^+,\infty} = 10^{-pH_\infty}$, $c_{OH^-,\infty} = 10^{-pOH_\infty}$, $c_{-,\infty} = c_\infty + c_{H^+,\infty} - c_{OH^-,\infty}$.

$\nu = \omega = 0$). This latter case is exactly identical to the predictions by Zhulina et al. [45]. Smaller $H_0$ for the case where EV effects have been neglected ensure a denser monomer concentration near to the wall, and accordingly, driven by the need to ensure a constant N, a smaller monomer concentration away from the wall. Deviation of the brush height due to the consideration of the EV interactions is maximum for larger $c_\infty$ and smaller $pH_\infty$ [see Fig. 2(b)]. Accordingly, for such $c_\infty - pH_\infty$ combinations, the variation in $\phi$ with and without the EV effects is maximum. Therefore this variation in $\phi$ between the cases of with and without the EV effects is witnessed to the largest extent in Fig. 3(d) ($c_\infty = 0.1\ M$ and $pH_\infty = 3$) and to the least extent in Fig. 3(a) ($c_\infty = 0.01\ M$ and $pH_\infty = 4$).

Fig. 4 provides the variation of the end distribution $g$ of the PE brushes considering finite EV interactions of varying magnitude (quantified by different values of $\nu$ and a given value of $\omega$) and no EV interactions (i.e., $\nu = \omega = 0$; this case is that of Ref. [45]). Given that the case without the EV effects lead to a larger concentration of the monomers at near-wall locations, we witness a larger value of g at such near wall locations for the case without the EV effects. On the other hand, an increase in the EV effects, leading to a flatter distribution of $\phi$ (see Fig. 3), ensures a larger $g$ value much away from the wall. Very much like Figs. 2 and 3, here too the maximum difference between the cases of with and without the EV interactions is witnessed for the condition of large $c_\infty$ and small $pH_\infty$.

Fig. 5 provides the transverse variation of the EDL electrostatic potential considering both finite EV interactions of varying magnitude between the PE brush segments (quantified by different values of $\nu$ and a given value of $\omega$) as well as

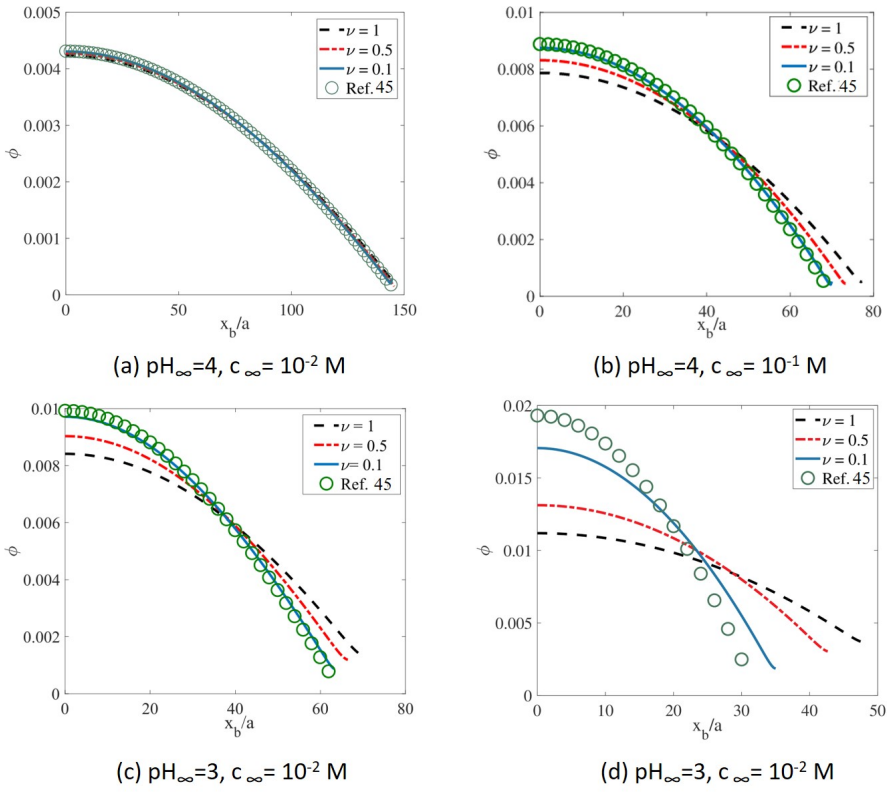


*Fig. 2.3:* Comparison of monomer distribution profiles ($\phi$) as a function of the dimensionless transverse distance along the brush ($x_b/a$, $a$ is the Kuhn length) obtained for different values of the first virial coefficient $\nu$ using our theory and theory of [45] for different $pH_\infty$ and $c_\infty$ values. All other parameters are identical to that used in Fig. 2.2.

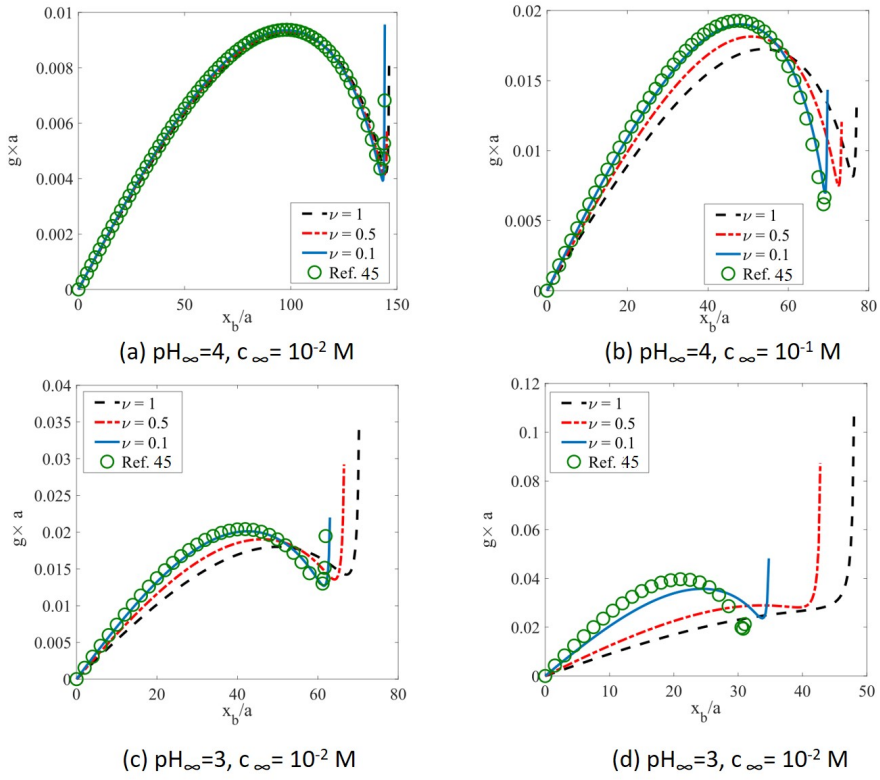


*Fig. 2.4:* Comparison of non-dimensional chain end distribution profiles ($g \times a$, $a$ is the Kuhn length) as a function of the dimensionless transverse distance along the brush ($x_b/a$) obtained for different values of the first virial coefficient $\nu$ using our theory and theory of [45] for different $pH_\infty$ and $c_\infty$ values. All other parameters are identical to that used in Fig. 2.2.

no EV interactions (i.e., $\nu = \omega = 0$; this case is that of Ref. [45]). The case of no EV interactions correspond to a shorter height of the brush implying a larger per unit volume charge density of the monomers, which in turn would ensure a larger magnitude of the EDL electrostatic potential at near-wall locations. At the same time, the presence of the shorter brushes imply that the brushes extend to smaller distances away from the grafting wall. Accordingly, there is no longer any charge from the brush at some finite distance away from the wall. These two factors simultaneously ensure that the electrostatic potential at near-wall locations is much larger and steeper for the case without the EV effects. The consideration of the EV effects makes the electrostatic potential much smaller and flatter. Here too this difference between the cases that consider or neglect the EV interactions is parimaril manifested for large $c_\infty$ and small $pH_\infty$.

### *2.3.2 Effects of consideration of an expanded form of the mass action law*

We have discussed previously that eq.(16) represents the expanded form of the mass action law and not eq.(21), which has been invariably used in most of the existing studies, but is only a special case of the expanded form of the mass action law obtain for the specific condition of $\gamma = 1/a^3$. In this subsection, we provide results dictating the PE brush configuration and the resultant EDL electrostatics for different values of $\gamma$, i.e., study the effect of the consideration of the expanded form of the mass action law. Fig. 6 shows the variation of the equilibrium brush height as a function of $\gamma a^3$. Increase in $\gamma$ or $\gamma a^3$ implies that the PE molecules has a larger backbone charge density. As a consequence, a larger number of counterions will get

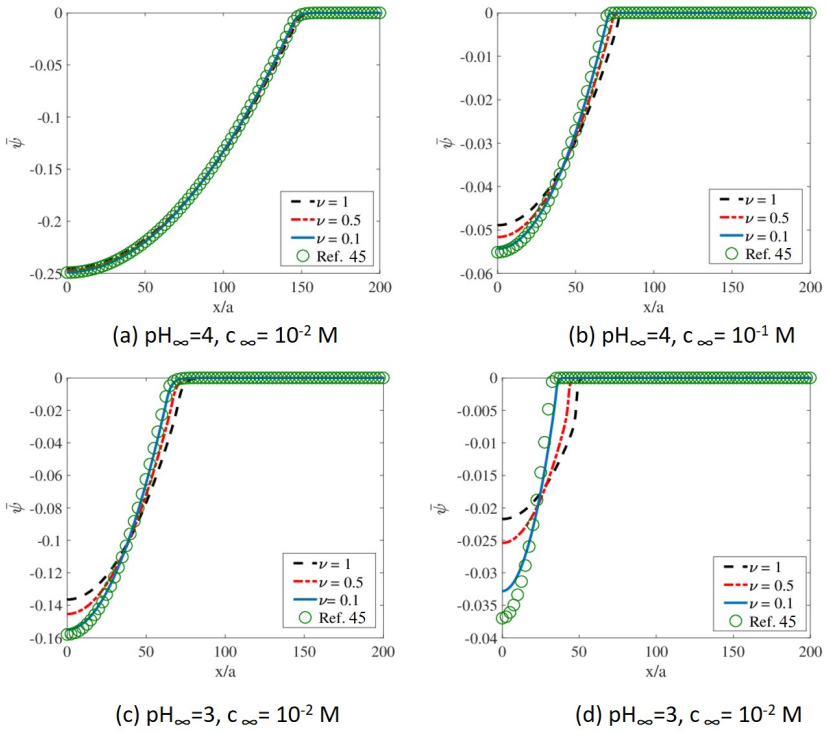


*Fig. 2.5:* Comparison of non-dimensional electrostatic potential profiles ($\bar{\psi} = e\psi/(k_B T)$) as a function of the dimensionless transverse distance along the nanochannel half height ($x/a$) obtained for different values of the first virial coefficient $\nu$ using our theory and theory of [45] for different $pH_\infty$ and $c_\infty$ values. All other parameters are identical to that used in Fig. 2.2.

localized within the brush in order to screen the larger magnitude of the PE charge. This, in turn, will lead to a larger counterion-induced osmotic swelling of the brushes (reflecting the tendency of the counterions to maximize their entropy by increasing the brush volume), eventually leading to a larger brush height [79–81]. Also, here too, the lowering of the salt concentration (i.e., increasing the EDL thickness, which in turn would lead to a screening of the PE backbone charge over a larger length) and an increase in the $pH_\infty$ (leading to a larger ionization and hence a greater charging of the PE molecule inducing a larger counterion-induced osmotic swelling) will cause an increase of the PE brush height. Here we also account for the EV interactions quantified by $\nu = 0.1$ and $\omega = 0.01$.

Fig. 7 provides the variation of the monomer density along the brush height for different values of $\gamma$. It was discussed Fig. 3, a shorter brush would imply a larger (smaller) monomer density close to (away from) the wall in comparison to the cases with larger brush height. This is also the case here – hence we witness a larger (smaller) monomer density close to (away from) the wall for smaller $\gamma$ values as well as the cases for larger salt concentration and smaller $pH_\infty$ values.

Fig. 8 provides the variation of the end distribution $g$ along the brush height for different values of $\gamma$. It was revealed in Fig. 4 that the case of smaller brush height leads to a larger concentration of the monomers close to the wall and results in a larger value of $g$ close to the wall and it decays quickly away from the wall. On the other hand, for the case of larger brush height, $g$ is much smaller at near wall locations and decays much more slowly away from the wall. This is the case here as well – hence we witness a larger (at near wall locations) and a steeply decaying $g$

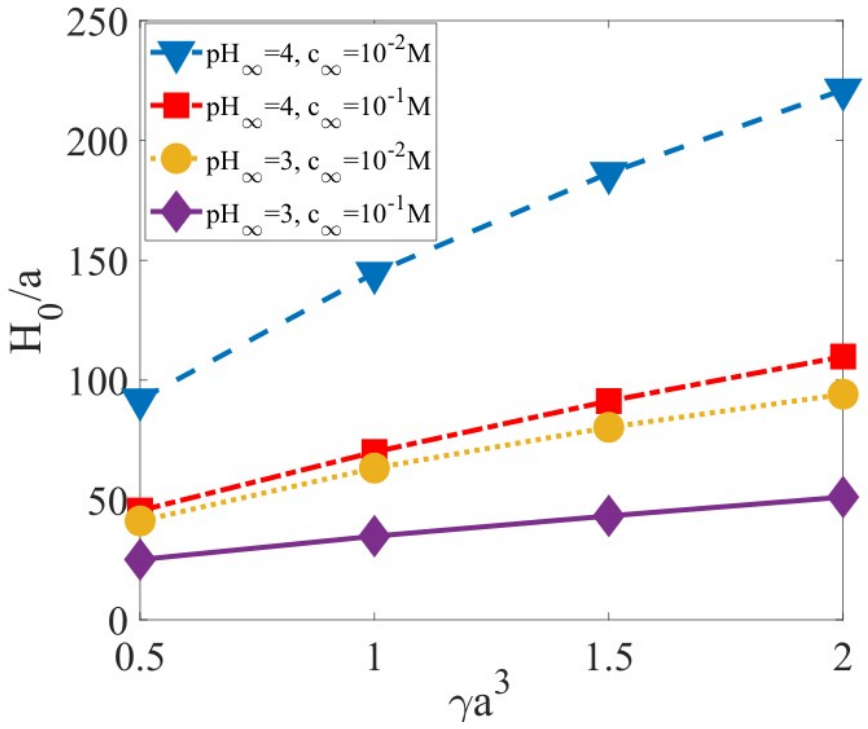


*Fig. 2.6:* Variation of non-dimensional equilibrium brush height $H_0/a$ with number of PCS per kuhn monomer $\gamma a^3$ for different $pH_\infty$ and $c_\infty$ values. $\nu = 0.1$, $\omega = 0.01$. All other parameters are identical to that used in Fig. 2.2.

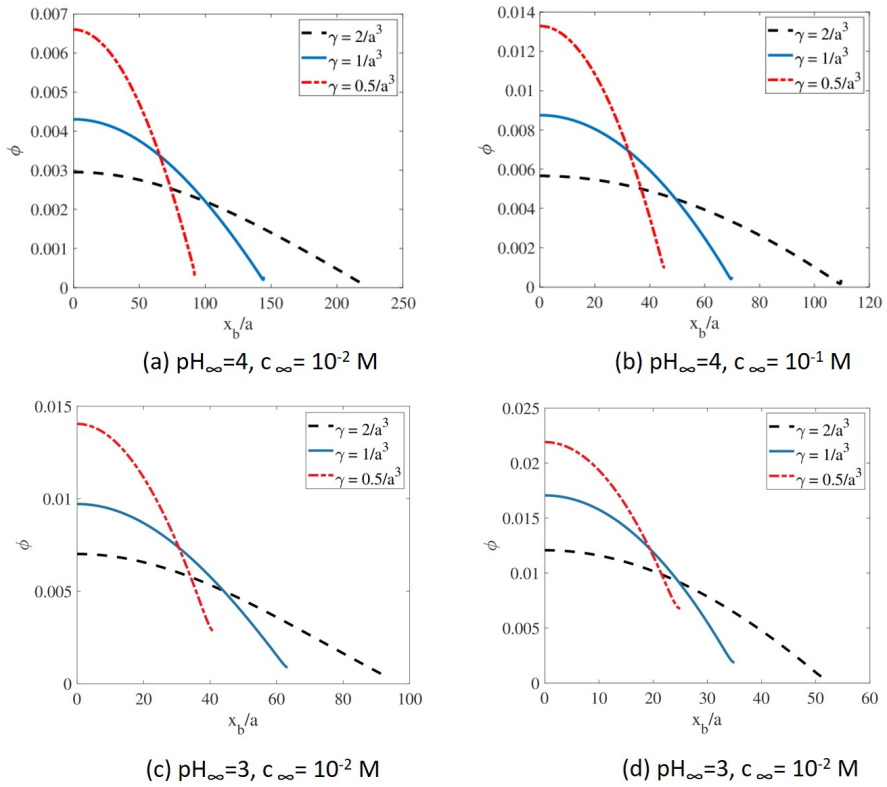


*Fig. 2.7:* Comparison of monomer distribution profiles ($\phi$) as a function of the dimensionless transverse distance along the brush ($x_b/a$, $a$ is the Kuhn length) obtained for different values of PCS number density $\gamma$ using our theory and theory of [45] for different $pH_\infty$ and $c_\infty$ values. $\nu = 0.1$, $\omega = 0.01$. All other parameters are identical to that used in Fig. 2.2.

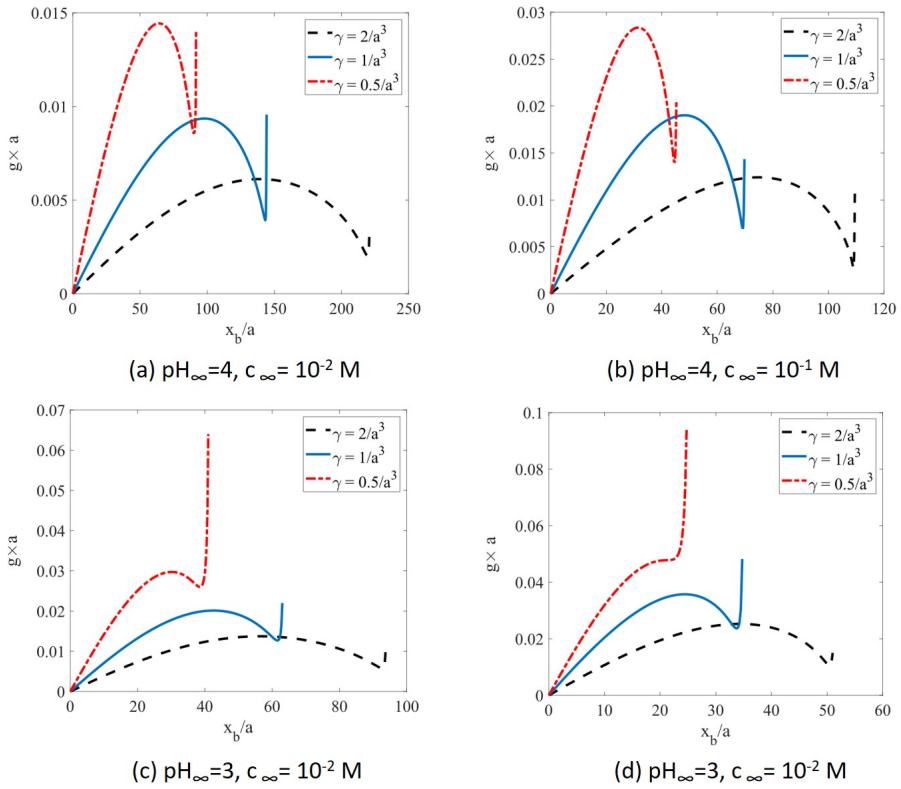


*Fig. 2.8:* Comparison of non-dimensional chain end distribution profiles ($g \times a$, $a$ is the Kuhn length) as a function of the dimensionless transverse distance along the brush ($x_b/a$) obtained for different values of PCS number density $\gamma$ using our theory and theory of [45] for different $pH_\infty$ and $c_\infty$ values. $\nu = 0.1$, $\omega = 0.01$. All other parameters are identical to that used in Fig. 2.2.

for the case with small $\gamma$ (i.e., the case that corresponds to smaller brush height, see Fig. 5), but a smaller and more weakly decaying $g$ for larger $\gamma$ (i.e., the condition that leads to taller brushes).

Finally, Fig. 9 provides the transverse variation of the EDL electrostatic potential for different values of $\gamma$. Smaller $\gamma$ implies both weakened charge density of the brushes as well as shorter brushes. Accordingly, for smaller $\gamma$, the EDL elec-

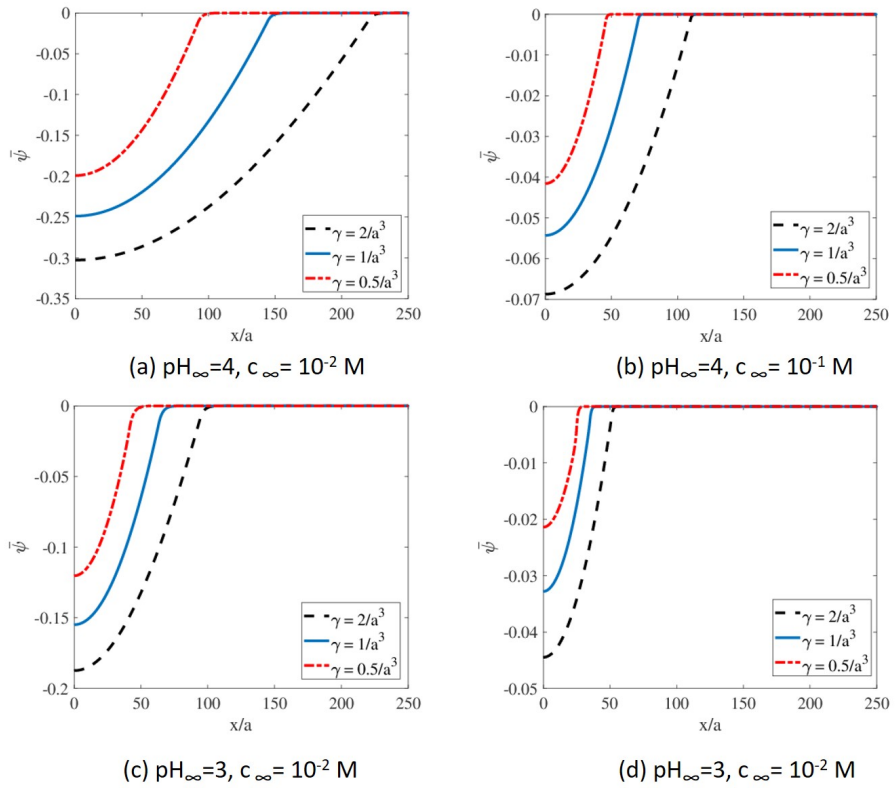


*Fig. 2.9:* Comparison of non-dimensional electrostatic potential profiles ($\bar{\psi} = e\psi/(k_B T)$) as a function of the dimensionless transverse distance along the nanochannel half height ($x/a$) obtained for different values of PCS number density $\gamma$ using our theory and theory of [45] for different $pH_\infty$ and $c_\infty$ values. $\nu = 0.1$, $\omega = 0.01$. All other parameters are identical to that used in Fig. 2.2.

trostatic potential is also weak and also decays quickly (since the brush height is small). Of course, for a given $\gamma$, a larger EDL electrostatic potential (magnitude) is invariably witnessed for lower $c_\infty$ (weakened screening of the charge of the PE brushes) and larger $pH_\infty$ (more enhanced ionization of the PE brushes).

## 2.4 Discussions

### 2.4.1 Applicability of the Proposed Theory

The proposed theory is directly applicable to all the systems that involve planar, pH-responsive PE brushes. Such brushes have been extensively employed for several applications such as nanochannel ion selectivity [27] and ion detection [82], fabrication of ionic valves [83,84], nanofluidic diodes [85], and surfaces of controllable wetting properties [86], and many more. The theory provides a new prediction of the EDL electrostatic potential distribution and consequently a new prediction for the number density distribution of the electrolyte, hydrogen, and hydroxyl ions for cases where the EV interactions between the PE segments become important and the PE brushes are so charged that $\gamma a^3 \neq 1$. This would imply that the corresponding changes in the ionic current or the current-voltage characteristics (in presence of an applied voltage), which in turn would dictate several of these applications [27,82–85], would be significantly different as compared to that obtained with the existing theory [45]. Similarly, the prediction of a new monomer distribution would critically affect the drag and the resulting fluid flow in brush-grafted nanochannels, which would impact the problems dictated by such fluid flows in brush-grafted nanochannels [22, 25, 87].

The present model, while describes the planar brushes, would also motivate developing models that account for the appropriate EV interactions and the expanded form of the mass action law for the pH-responsive spherical [156] or cylindrical PE

brushes (i.e., PE brushes grafted to spheres and cylinders) that have been employed in many applications such as the use of nanoparticles grafted with pH-responsive brushes for targeted drug delivery [89], protein binding [90], synthesis of magnetic nanoparticles [91], etc. Finally, the use of the generic mass action law would be useful to improve the theoretical predictions of not only the pH-responsive planar and curved PE brushes, but also all those calculations that involve generic pH-responsive PE molecules and gels [74–78].

### *2.4.2 Limitations and Scope of Improvement of the Proposed Theory*

In this paper, we employ the strong stretching theory (SST) framework which assumes the brushes to be in a strongly stretched configuration. Hence we ignore the effects of lateral variation of monomer distribution profile and bending back of chain ends. The approximation holds good for systems with high grafting density. For other systems, an advanced numerical self-consistent field theory (SCFT) model [92] needs to be implemented.

The second important issue is that we invariably assume that the EDLs are always thin enough to ensure that $\ell \gg 2\lambda_D$ ($\ell$ is the distance between the adjacent grafted chains and $\lambda_D$ is the EDL thickness) and there is no overlap between the EDLs formed by the adjacent brushes. In case such an approximation does not hold, one would need to assume a 2D (and not a 1D) model for the brush EDL electrostatics and alter the SST accordingly [93].

Thirdly, no non-PB component (e.g. finite ion size effect [94, 95], solvent polarization effect [96], or ion-ion correlation effect [97]) has been considered in the

description of the EDL. These effects would become important for large $\psi$ and large salt concentration and would significantly impact the overall self-consistent field approach.

Fourthly, our theory also does not consider the correlations due to the connectivity of the polymer charges. Such correlations can be specially significant for pH-responsive systems (like pH-responsive PE brushes). For example, there are chances that the effective $pK_a$ of the polymer chain might get significantly altered due to the connected charges of the pH-responsive PE chain [98]. Such alteration of the $pK_a$ and its resulting connotations in all the presented results have been obviously neglected in the present study.

Finally, we shall like to emphasize that given the fact that we have used mean-field calculations in this paper, the capability of the present model to quantify the exact influence of the EV effects will be limited. This stems from the fact that the mean field assumptions extend to the EV effect consideration as well. This has been described in detail by Alexander-Katz et al. [99]. In this paper [99], the authors studied confined polymer solutions and used the density profiles to obtain the effective correlation length $\xi_{eff}$ quantifying the non-mean-field polymer correlations and obtained the results to the mean field theory predictions. While for small EV parameters, the $\xi_{eff}$ was well described by the mean-field theory results, for larger EV parameters $\xi_{eff} \sim C^{-3/4}$ ($C$ is the polymer solution concentration), a result that the mean-field theory could not predict. In essence, therefore, chances are that the inherently mean-field approach of the our calculations would imply that some of the predictions of the effect of considering the EV interactions will be

limited.

## 2.5 Conclusions

In this paper, we develop a self-consistent field approach (modified SST) to probe the behavior of the pH-responsive brush system by accounting for (a) the EV interactions between the PE segments and (b) a more expanded form of the mass action law valid for $\gamma a^3 \neq 1$. Results indicate an enhancement of the brush height due to the consideration of the EV interaction driven PE inter-segmental repulsion and an increase (decrease) of the brush height for $\gamma a^3 > 1$ ($\gamma a^3 < 1$) due to increased (decreased) counterion-induced osmotic swelling of the brushes. We also establish that these typical height variations get reflected in the corresponding variations of the monomer density profile, distributions of the PE brush ends, and the corresponding EDL electrostatic potential distribution. This model, which can be considered as the most generic SST model for the pH-responsive PE brushes, will not only be critical for explaining several experiments that invariably consider the PE brushes to be in a "good" solvent, but will also help to better interpret a large number of problems that involve pH-responsive PE molecules (not necessarily in a "brush" configuration) and gels and where a more expanded form of the mass action law with $\gamma a^3 \neq 1$ may be more applicable.

In the end, we shall like to point out that there exist very few experimental studies that have probed the equilibrium structure and configuration of pH-responsive polyelectrolyte (PE) brushes [100,101]. Mahalik et al. [63] made the first attempt to com-

pare experimental results for planar PE brushes with theoretical models such as the Strong Stretching Theory (SST) [45] and Self- consistent Field Theory (SCFT) [92]. However, they used a multivariate optimization-based approach to fit several parameters like the degree of polymerization, Kuhn length, bulk salt concentration, etc. to obtain the best match between the theoretical and experimental monomer distribution profiles. This approach has several limitations (the best fit parameters do not necessarily agree with the experimental conditions) and was used since the existing experimental studies are not able to specify the precise values of several brush-related parameters. For example, it is very difficult to pinpoint the degree of polymerization, grafting density and polydispersity index for PE brushes prepared using SI-ATRP (Surface-initiated atom transfer radical polymerization). Moreover, it is difficult to quantify the exact value of the excluded volume parameter for experimental studies. All these factors negate the possibility of comparing our analytical results with the existing experimental studies.

## *2.6 Appendix*

### *Derivation of eqs.(2.14-2.20)*

We employ variational calculus to carry out the minimization of the free energy functional [eq.(12)]. Assuming that the chain is flexible (p=1) and taking the variation of each free energy component w.r.t. $\mathrm{E}(x, x')$, $\mathrm{g}(x')$, $\psi$, $n_{A^-}$, $n_{\pm}$, $n_{H^+}$ and

$n_{OH^-}$, we shall get:

$$\begin{aligned}\frac{\delta F'_{els}}{k_BT} =&\frac{3}{2a^2}\Big[\int_0^H g(x')dx'\int_0^{x'}\delta E(x,x')dx+\int_0^H \delta g(x')dx'\int_0^{x'}E(x,x')dx\Big]\\&+\lambda_1\frac{\sigma}{a^3}\int_0^H\delta\phi(x)dx-\int_0^H\lambda_2(x')dx'\int_0^{x'}\frac{\delta E(x,x')}{E^2(x,x')}dx\end{aligned}\tag{A1}$$

$$\frac{\delta F_{EV}}{k_BT}=\frac{\sigma}{a^3}\int_0^H\Big(\frac{\delta f_{conc}}{\delta\phi}\Big)\delta\phi dx\tag{A2}$$

$$\begin{aligned}\frac{\delta F_{elec}}{k_BT}+\frac{\delta F_{EDL}}{k_BT} =&\frac{\sigma}{k_BT}\int_0^\infty\Big[-\frac{\epsilon_0\epsilon_r}{2}\delta\Big|\frac{d\psi}{dx}\Big|^2+e\delta\psi(n_+-n_-+n_{H^+}-n_{OH^-})\\&+e\psi(\delta n_+-\delta n_-+\delta n_{H^+}-\delta n_{OH^-})\Big]dx-\frac{\sigma}{k_BT}\int_0^H\delta\Big[e\psi n_{A^-}(x)\phi\Big]dx\\&+\sigma\int_0^\infty\delta\Big[n_+\Big(ln\Big(\frac{n_+}{n_{+,\infty}}\Big)-1\Big)+n_-\Big(ln\Big(\frac{n_-}{n_{-,\infty}}\Big)-1\Big)\\&+n_{H^+}\Big(ln\Big(\frac{n_{H^+}}{n_{H^+,\infty}}\Big)-1\Big)+n_{OH^-}\Big(ln\Big(\frac{n_{OH^-}}{n_{OH^-,\infty}}\Big)-1\Big)\\&+(n_{+,\infty}+n_{-,\infty}+n_{H^+,\infty}+n_{OH^-,\infty})\Big]dx\end{aligned}$$

$$\begin{aligned}=&\frac{\sigma}{k_BT}\int_0^\infty\Big[\epsilon_0\epsilon_r\Big(\frac{d^2\psi}{dx^2}\Big)\delta\psi+e\delta\psi(n_+-n_-+n_{H^+}-n_{OH^-})+\\&e\psi(\delta n_+-\delta n_-+\delta n_{H^+}-\delta n_{OH^-})\Big]dx-\frac{\sigma}{k_BT}\int_0^H\Big[e\phi\Big(\frac{K'_a\gamma}{K'_a+n_{H^+}}\Big)\delta\psi\\&-e\phi\psi\frac{K'_a\gamma}{(K'_a+n_{H^+})^2}\delta n_{H^+}+e\psi\Big(\frac{K'_a\gamma}{K'_a+n_{H^+}}\Big)\delta\phi\Big]dx\\&+\sigma\int_0^\infty\Big[\delta n_+ln\Big(\frac{n_+}{n_{+,\infty}}\Big)+\delta n_-ln\Big(\frac{n_-}{n_{-,\infty}}\Big)+\delta n_{H^+}ln\Big(\frac{n_{H^+}}{n_{H^+,\infty}}\Big)\\&+\delta n_{OH^-}ln\Big(\frac{n_{OH^-}}{n_{OH^-,\infty}}\Big)\Big]dx\end{aligned}\tag{A3}$$

$$\frac{\delta F_{ion}}{k_BT} = \frac{\sigma}{a^3}\int_0^H \delta\phi \left[\Big(1-\frac{n_{A^-}}{\gamma}\Big)ln\Big(1-\frac{n_{A^-}}{\gamma}\Big)+\frac{n_{A^-}}{\gamma}ln\Big(\frac{n_{A^-}}{\gamma}\Big)+\frac{n_{A^-}}{\gamma}ln\Big(\frac{n_{H^+,\infty}}{K'_a}\Big)\right]dx$$
$$+\frac{\sigma}{a^3}\int_0^H \phi\,\delta\left[\Big(1-\frac{n_{A^-}}{\gamma}\Big)ln\Big(1-\frac{n_{A^-}}{\gamma}\Big)+\frac{n_{A^-}}{\gamma}ln\Big(\frac{n_{A^-}}{\gamma}\Big)+\frac{n_{A^-}}{\gamma}ln\Big(\frac{n_{H^+,\infty}}{K'_a}\Big)\right]dx$$

$$=\frac{\sigma}{a^3}\int_0^H \delta\phi \left[\Big(1-\frac{n_{A^-}}{\gamma}\Big)ln\Big(1-\frac{n_{A^-}}{\gamma}\Big)+\frac{n_{A^-}}{\gamma}ln\Big(\frac{n_{A^-}}{\gamma}\Big)+\frac{n_{A^-}}{\gamma}ln\Big(\frac{n_{H^+,\infty}}{K'_a}\Big)\right]$$
$$+\frac{\sigma}{a^3}\int_0^H \phi\,\delta n_{A^-}\left[-\frac{1}{\gamma}ln\Big(1-\frac{n_{A^-}}{\gamma}\Big)+\frac{1}{\gamma}ln\Big(\frac{n_{A^-}}{\gamma}\Big)+\frac{1}{\gamma}ln\Big(\frac{n_{H^+,\infty}}{K'_a}\Big)\right]dx \tag{A4}$$

Substituting eq.(A1), (A2), (A3) and (A4) in (2.13), we get:

$$\frac{\delta F'}{k_BT} = \frac{3}{2pa^2}\Big[\int_0^H g(x')dx'\int_0^{x'}\delta E(x,x')dx+\int_0^H \delta g(x')dx'\int_0^{x'}E(x,x')dx\Big]$$
$$+\lambda_1\frac{\sigma}{a^3}\int_0^H\delta\phi(x)dx-\int_0^H\lambda_2(x')dx'\int_0^{x'}\frac{\delta E(x,x')}{E^2(x,x')}dx+\frac{\sigma}{a^3}\int_0^H\Big(\frac{\delta f_{conc}}{\delta\phi}\Big)\delta\phi dx$$
$$+\frac{\sigma}{k_BT}\int_0^\infty\Big[\epsilon_0\epsilon_r\Big(\frac{d^2\psi}{dx^2}\Big)\delta\psi+e\delta\psi(n_+-n_-+n_{H^+}-n_{OH^-})+e\psi(\delta n_+-\delta n_-$$
$$+\delta n_{H^+}-\delta n_{OH^-})\Big]dx-\frac{\sigma}{k_BT}\int_0^H\Big[e\phi n_{A^-}\delta\psi+e\phi\psi\delta n_{A^-}+e\psi n_{A^-}\delta\phi\Big]dx$$
$$+\sigma\int_0^\infty\Big[\delta n_+ln\Big(\frac{n_+}{n_{+,\infty}}\Big)+\delta n_-ln\Big(\frac{n_-}{n_{-,\infty}}\Big)+\delta n_{H^+}ln\Big(\frac{n_{H^+}}{n_{H^+,\infty}}\Big)+\delta n_{OH^-}ln\Big(\frac{n_{OH^-}}{n_{OH^-,\infty}}\Big)\Big]dx$$
$$+\frac{\sigma}{a^3}\int_0^H\delta\phi\left[\Big(1-\frac{n_{A^-}}{\gamma}\Big)ln\Big(1-\frac{n_{A^-}}{\gamma}\Big)+\frac{n_{A^-}}{\gamma}ln\Big(\frac{n_{A^-}}{\gamma}\Big)+\frac{n_{A^-}}{\gamma}ln\Big(\frac{n_{H^+,\infty}}{K'_a}\Big)\right]dx$$
$$+\frac{\sigma}{a^3}\int_0^H\delta n_{A^-}\phi\left[-\frac{1}{\gamma}ln\Big(1-\frac{n_{A^-}}{\gamma}\Big)+\frac{1}{\gamma}ln\Big(\frac{n_{A^-}}{\gamma}\Big)+\frac{1}{\gamma}ln\Big(\frac{n_{H^+,\infty}}{K'_a}\Big)\right]dx \tag{A5}$$

Variation of eq.(2.10) gives:

$$\delta\phi(x)=\frac{a^3}{\sigma}\int_x^H\Big[\frac{\delta g(x')}{E(x,x')}-\frac{g(x')\delta E(x,x')}{E^2(x,x')}\Big]dx' \tag{A6}$$

Substituting eq.(A6) in (A5) and rearranging gives:

$$\frac{\delta F'}{k_BT} = \int_0^H dx' \int_0^{x'} \delta E(x,x') \Bigg[ \frac{3g(x')}{2pa^2} - \frac{\lambda_2(x')}{E^2(x,x')} - \Bigg( \frac{\delta f_{conc}}{\delta\phi} + \lambda_1 - \frac{ea^3\psi}{k_BT} n_{A^-} + \Big(1 - \frac{n_{A^-}}{\gamma}\Big) ln\Big(1 - \frac{n_{A^-}}{\gamma}\Big) + \frac{n_{A^-}}{\gamma} ln\Big(\frac{n_{A^-}}{\gamma}\Big) + \frac{n_{A^-}}{\gamma} ln\Big(\frac{n_{H^+,\infty}}{K'_a}\Big) \Bigg) \frac{g(x')}{E^2(x,x')} \Bigg] dx$$

$$+ \int_0^H dx' \delta g(x') \int_0^{x'} \Bigg[ \frac{3E(x,x')}{2pa^2} + \Bigg( \frac{\delta f_{conc}}{\delta\phi} + \lambda_1 - \frac{ea^3\psi}{k_BT} n_{A^-} + \Big(1 - \frac{n_{A^-}}{\gamma}\Big) ln\Big(1 - \frac{n_{A^-}}{\gamma}\Big) + \frac{n_{A^-}}{\gamma} ln\Big(\frac{n_{A^-}}{\gamma}\Big) + \frac{n_{A^-}}{\gamma} ln\Big(\frac{n_{H^+,\infty}}{K'_a}\Big) \Bigg) \frac{1}{E(x,x')} \Bigg] dx$$

$$+ \frac{\sigma}{\gamma a^3} \int_0^H \delta n_{A^-} \phi \Bigg[ - \gamma a^3 \frac{e\psi}{k_BT} - ln\Big(1 - \frac{n_{A^-}}{\gamma}\Big) + ln\Big(\frac{n_{A^-}}{\gamma}\Big) + ln\Big(\frac{n_{H^+,\infty}}{K'_a}\Big) \Bigg] dx$$

$$+ \frac{\sigma}{k_BT} \int_0^H \delta\psi \Big[ \epsilon_0\epsilon_r \Big(\frac{d^2\psi}{dx^2}\Big) + e\Big(n_+ - n_- + n_{H^+} - n_{OH^-} - n_{A^-}\phi\Big) \Big] dx$$

$$+ \frac{\sigma}{k_BT} \int_H^\infty \delta\psi \Big[ \epsilon_0\epsilon_r \Big(\frac{d^2\psi}{dx^2}\Big) + e(n_+ - n_- + n_{H^+} - n_{OH^-}) \Big] dx$$

$$+ \sigma \int_0^\infty \delta n_+ \Big[ \frac{e\psi}{k_BT} + ln\Big(\frac{n_+}{n_{+,\infty}}\Big) \Big] dx + \sigma \int_0^\infty \delta n_- \Big[ - \frac{e\psi}{k_BT} + ln\Big(\frac{n_-}{n_{-,\infty}}\Big) \Big] dx$$

$$+ \sigma \int_0^\infty \delta n_{H^+} \Big[ \frac{e\psi}{k_BT} + ln\Big(\frac{n_{H^+}}{n_{H^+,\infty}}\Big) \Big] dx + \sigma \int_0^\infty \delta n_{OH^-} \Big[ - \frac{e\psi}{k_BT} + ln\Big(\frac{n_{OH^-}}{n_{OH^-,\infty}}\Big) \Big] dx \tag{A7}$$

Equating $\delta F'$=0 yields the desired eqs.(2.14-2.20) since $\delta E(x,x') \neq 0$, $\delta g(x') \neq 0$, $\delta\psi \neq 0$, $\delta n_{A^-} \neq 0$, $\delta n_\pm \neq 0$, $\delta n_{H^+} \neq 0$, $\delta n_{OH^-} \neq 0$.

# Chapter 3: Theoretical study on the massively augmented electroosmotic water transport in polyelectrolyte brush functionalized nanoslits

*In this chapter*[1]*, we demonstrate that functionalizing nanoslits with pH-responsive polyelectrolyte (PE) brushes can lead to extremely fast electroosmotic (EOS) water transport, where the maximum centreline velocity and the volume flow rate can be an order of magnitude larger than these quantities in identically charged brush-free nanochannels for a wide range of system parameters. Such an enhancement is most remarkable given that the brushes have been known to retard the transport by imparting additional drag on the fluid flow. We argue that this enhancement stems from the localization of the charge density of the brush-induced electric double layer (and hence the EOS body force) away from the nanochannel wall (or the location of the wall-induced drag force). This ensures a much larger impact of the EOS body force triggering such fast water transport. Finally, the calculated flux values for the present brush-grafted nanochannels are found to be significantly larger than*

[1] Contents of this chapter have been published as: *V. S. Sivasankar, S. A. Etha, H. S. Sachar, and S. Das, "Theoretical study on the massively augmented electro-osmotic water transport in polyelectrolyte brush functionalized nanoslits", Phys. Rev. E , 102, 013103 (2020).*

*those for a wide range of nanofluidic membranes and channels, suggesting that the brush functionalization can be considered as a mechanism for enabling such superfast nanofluidic transport.*

## *3.1 Introduction*

Nanofluidic transport of liquids and ions [102–104] has been critical to a large number of disciplines ranging from energy generation, conversion, and utilization [105,106], sensing and separation [107,108], and gating of ion and liquids [83,109] to the understanding of the behavior of biological systems for developing biomimetic and bioinspired applications [110, 111]. Very often, these applications necessitate modifying the properties and/or working principles of these nanochannels. Grafting the nanochannels with PE brushes that are sensitive to the environmental stimuli has served as one of the most popular techniques for modifying the nanochannel functionality enabling applications like ion and biosensing [112, 113], fabrication of ionic diodes [39] and current rectifiers [34, 114], etc. Most of these applications of the PE-brush grafted nanochannels rely on the brush-induced alteration of the ionic current and is aided by the fact that the corresponding liquid transport is severely weakened due to the brush-induced additional drag force [22]. Such a reduction in liquid transport in micro/nanochannels by grafting the channel walls with polymer/PE molecules is a well-documented phenomenon. For example, Bruin et al. in their experimental study reported a decrease in the electroosmotic (EOS) flow in fused-silica capillaries with walls grafted with with $\gamma$-glycidoxypropyltrimethoxy-

silane and polyethylene glycol [115]. Fung and Yeung showed that the dynamic coating of polyethylene oxide (PEO) in bare-silica capillary columns was able to significantly reduce the EOS flow, which in turn enabled high-speed DNA sequencing [16]. A thorough study by Monteferrante et al. [17] combined experiments and theory to clearly establish that liquid flow velocity is significantly reduced in a capillary coated with a copolymer consisting of N,N-dimethylacrylamide (DMA), glycidyl methacrylate (GMA), 3-(trimethoxysilyl) propyl methacrylate (MAPS), and N,N-dimethyl aminoethyl acrylamide: they associated this velocity reduction to the large frictional forces imparted by the grafted polymer molecules. In addition to these experimental studies, there have been a plethora of simulation studies that employ sophisticated molecular dynamics (MD) simulations and establish such a significant flow reduction in nanochannels grafted with polymer/PE molecules and brushes due to the enhanced drag force imparted by these polymer molecules and brushes on the fluid flow [18–20, 116, 117]. In this paper we describe a complete paradigm reversal in the context of the liquid transport in the PE brush-grafted nanochannels. We establish a wide range of parameter space where the grafting of nanochannels with pH-responsive, backbone-charged PE brushes can ensure an electroosmotic (EOS) water transport that is much more augmented as compared to that in equally charged, brush-free nanochannels. Such superfast water transport manifests as, for some parameter combinations, channel centreline velocities and volume flow rates in brush-grafted nanochannels that are an order of magnitude larger than those for the similarly charged brush-free nanochannels. The brushes ensure that the effective centre of the charge is away from the nanochannel wall,

which implies that the effective centre of the charge density of the brush-induced EDL (electric double layer) is also away from the wall. As a consequence, when an external axial electric field is employed to drive an EOS flow, the EOS body force (resulting from the interaction of this EDL charge density and the applied electric field) is localized away from the nanochannel wall (see Fig. 3.1). Therefore, there is a spatial difference in the location of the EOS body force and the wall induced drag. Such a difference augments the influence of the EOS body force, which in turn induces, particularly for conditions that increase the brush height, such an augmentation of the velocity field in comparison to that in the similarly charged brush-free nanochannels.

In a series of previous studies [30–32, 57], we have established such EDL-localization-induced enhanced electrokinetic transport in nanochannels grafted with *end-charged PE brushes*. However, these studies did not manifest such massive augmentation in the flow field as they overestimated the drag (particularly for the tall brushes) from the brushes modelled using the simplistic Alexander-de-Gennes model [4–6] that assumes a uniform monomer distribution. On the other hand, the present study considers a much more rigorous augmented Strong Stretching Theory (SST) description of the PE brushes [118,119], which ensures a much larger monomer density at near-wall, low-velocity locations [118,119] leading to a smaller overall drag contribution (the local brush-induced drag force is proportional to thfe local fluid velocity and the drag coefficient is proportional to the square of the monomer density) from the brushes. Therefore, we can infer that the present study is different from the study of Chen and Das [30] in two critical aspects. First the present study consid-

ers a much more realistic system (a fully backbone-charged PE brush as compared to an end-charged brush) and provides a significantly more rigorous description (augmented SST model [118, 119] instead of the simplistic Alexander de-Gennes model [4–6]) of the PE brushes in modelling the EOS transport in brush-grafted nanochannels. Second, this more rigorous description of the PE brushes ensures that we do not overestimate the PE-brush-imparted drag force that occurs when the Alexander de-Gennes model, which considers a uniform monomer distribution, is employed to describe the PE brushes. Under such circumstances, we establish that in presence of the experimentally realizable values of the applied axial electric fields ($10^4$–$5\times10^4$ V.m$^{-1}$) [120], the EOS water flux values obtained for the present case of the PE-brush-grafted nanochannels can be significantly larger than the flux values obtained for nanochannel/nanopassage/nanotube-based membranes [121–132] and nanofluidic systems [133–135] and less than one order of magnitude smaller than the tremendously high fluxes observed in graphene nanochannels and carbon nanotubes [136, 137].

## *3.2 Theory*

We consider a nanochannel of height $2h$ ($-h \leq y \leq h$) grafted with pH-responsive, backbone-charged PE brushes [see Fig. 3.1(b)]. This section provides the information to obtain the steady and fully-developed EOS flow field in the PE-brush-grafted nanochannel.

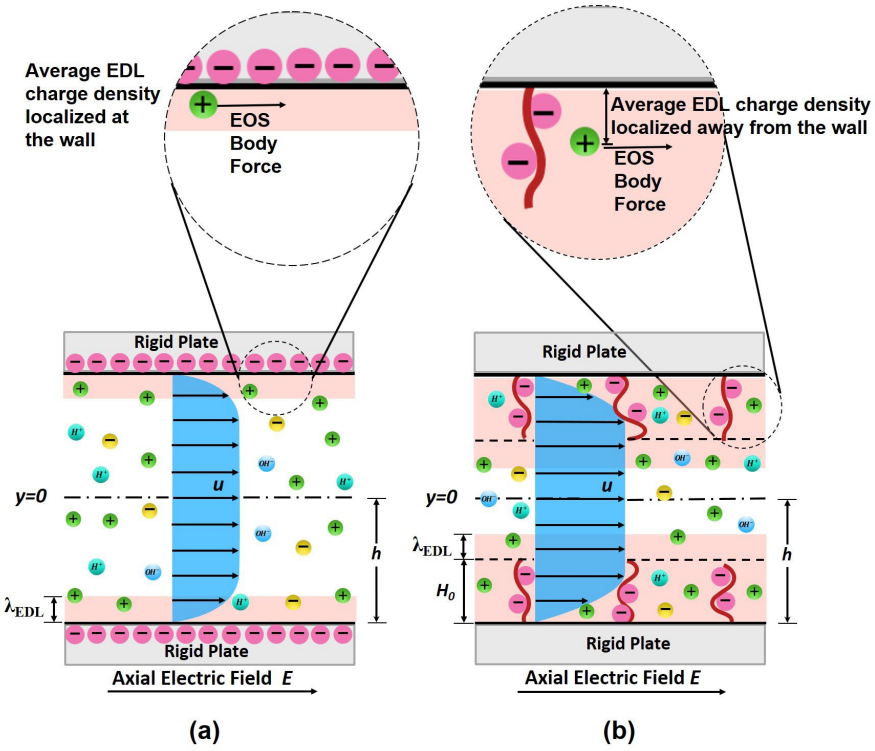


*Fig. 3.1:* Schematic comparing the EOS transport (due to the axial electric field) in (a) brush-free and (b) brush-grafted nanochannel. The brushes enforce the localization of the EDL charge density away from the wall enforcing the EOS body force to be localized away from the wall (location of the drag force). Here, $\lambda_{EDL}$ denotes the EDL thickness.

### 3.2.1 *Electroosmotic Transport in Brush-Functionalized Nanochannels: Theoretical Model*

Once the equilibrium brush configuration and the brush-induced EDL electrostatics have been obtained, we use this information to obtain the steady and fully-developed EOS flow field in the PE-brush-grafted nanochannel. The fluid flow is described by the following equation:

$$\begin{aligned}
&\eta\frac{d^2u}{dy^2} + eE\left(\Sigma_i n_i z_i\right) - \frac{\eta}{\kappa_d}u = 0 \quad (-h \le y \le -h + H_0),\\
&\eta\frac{d^2u}{dy^2} + eE\left(\Sigma_i n_i z_i\right) = 0 \quad (-h + H_0 \le y \le 0),
\end{aligned} \tag{3.1}$$

in presence of the boundary conditions expressed as:

$$\begin{aligned}
&(u)_{y=-h} = 0, \;\; (u)_{y=(-h+H_0)^+} = (u)_{y=(-h+H_0)^-},\\
&\left(\frac{du}{dy}\right)_{y=0} = 0, \;\; \left(\frac{du}{dy}\right)_{y=(-h+H_0)^+} = \left(\frac{du}{dy}\right)_{y=(-h+H_0)^-}
\end{aligned} \tag{3.2}$$

In the above equations, which consider the flow field only in the bottom half of the nanochannel (i.e., $-h \le y \le 0$), $H_0$ is the equilibrium brush height, $\eta$ is the dynamic viscosity of water, $E$ is the applied axial electric field, $u$ is the velocity field, $n_i$ and $z_i$ are the number density distribution and valence of ion $i$ ($i = \pm$, $H^+$, $OH^-$; "+" and "−" denote the cations and anions of the electrolyte), and $\eta/\kappa_d$ represents the per unit volume drag coefficient. Here, following the analysis of de Gennes [138] and Freed and Edwards [139], one can express

$$\kappa_d = a^2/\phi^2 = a^2\left(\frac{H_0}{\sigma a^3 N\bar{\phi}}\right)^2 \tag{3.3}$$

and

$$\bar{\phi} = \frac{\phi H_0}{\sigma a^3 N}. \tag{3.4}$$

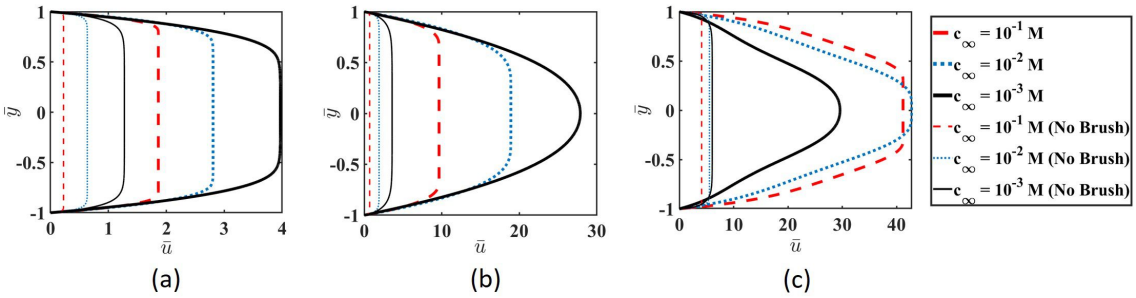


*Fig. 3.2:* Transverse variation of the non-dimensional velocity profile $\bar{u}[\bar{u} = \frac{u}{u_0}$, where $u_0 = \left(\frac{k_B T}{e}\right)\frac{\epsilon_0 \epsilon_r E}{\eta}$ is the velocity scale, $k_B T$ is the thermal energy, $\epsilon_0$ is the permittivity of free space and $\epsilon_r$ is the relative permittivity of water.] with bulk salt concentration $c_\infty$ for PE brush-grafted nanochannel for (a) $pH_\infty = 3$, $\ell = 60$ nm, (b) $pH_\infty = 4$, $\ell = 60$ nm, and (c) $pH_\infty = 3$, $\ell = 10$ nm. Here we consider the flow profiles for the equilibrium-brush-EDL configurations (see chapter 2 for the equations and Refs. [118, 119] for the figures) obtained using $N = 400$, $h = 100$ nm, $a = 1$ nm (Kuhn length), $k_B = 1.38$ x $10^{-23}$ J.K$^{-1}$, $T = 298$ K, $e = 1.6 \times 10^{-19}$ C (electronic charge), $\epsilon_0 = 8.8$ x $10^{-12}$ Fm$^{-1}$, $\epsilon_r = 79.8$, $\gamma a^3 = 1$, $pK_a = 3.5$, $\nu = 0.5$, $\omega = 0.1$. $pK_w$ =14, $pOH_\infty = pK_w$ - $pH_\infty$, $c_{+,\infty} = c_\infty$, $c_{H^+,\infty} = 10^{-pH_\infty}$, $c_{OH^-,\infty} = 10^{-pOH_\infty}$, and $c_{-,\infty} = c_\infty + c_{H^+,\infty} - c_{OH^-,\infty}$. The definitions of all the terms and parameters are provided in chapter 2.

In the above equations, $a$ is the PE brush Kuhn length, $N$ is the number of monomers of a brush molecule, $\phi$ is the monomer distribution profile, and $\sigma$ is the PE brush grafting density (please see [22,119] for more details). The augmented SST analysis provides an expression for the equilibrium brush height $H_0$, monomer distribution $\phi$, brush-end distribution $g(y)$, and also relates $n_i$ to the electrostatic potential $\psi$ through the Boltzmann distribution (please see the previous subsection). These informations close eqs.(3.1,3.2), which when solved yields the velocity distribution for the EOS transport in nanochannels with uncharged walls but grafted with backbone-charged, pH-responsive PE brushes. These velocity profiles are compared with those obtained for charged, brush-free nanochannels. The second equation of eq.(3.1), valid for $-h < y < 0$, and the first and third conditions of eq.(3.2) describe the EOS transport in such brush-free nanochannels having the same equivalent (bare-wall) surface charge density ($\sigma_{c,eq}$) as that of the corresponding brush-grafted nanochannels. We can write:

$$\sigma_{c,eq} = -e \int_{-h}^{-h+H_0} \phi n_{A^-} dy, \tag{3.5}$$

where $n_{A^-}$ is expressed in eq.(2.16).

## *3.3 Results and Discussions*

We consider brush-grafted nanochannels with small ($\ell$=60 nm) and large ($\ell$=10 nm) grafting densities. Here $\ell$ is the lateral separation between the grafted

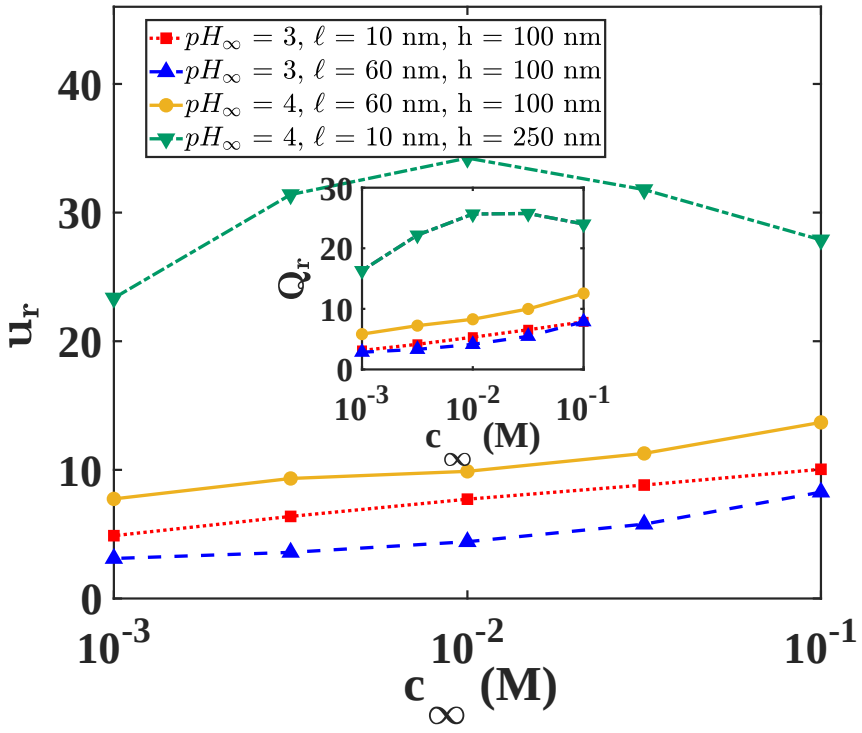


*Fig. 3.3:* Ratio of the maximum centreline velocities ($u_r = u_{max,B}/u_{max,NB}$) and volume flow rates ($Q_r = Q_B/Q_{NB}$) (inset) with $c_\infty$ for different combinations of $\ell$, $h$ and $pH_\infty$. All other parameters are same as those in Fig. 3.2

brushes with $\ell = 1/\sqrt{\sigma}$. $\sigma_{c,eq}$ of the brush-free nanochannels (defined above) vary depending on the brush-grafted nanochannels against which their results are compared. Fig. 3.2 compares the velocity profiles for the brush-grafted and the corresponding (i.e., with identical charge content) brush-free nanochannels revealing three key issues. First, the channel centreline maximum velocity for the brush-grafted nanochannel ($u_{max,B}$) is always larger than that of the corresponding brush-free nanochannel ($u_{max,NB}$). Second, an increase in salt concentration, in general, increases the ratio $u_r = u_{max,B}/u_{max,NB}$ for a given $pH_\infty$ and $\ell$. These two results signify the massive velocity enhancement effect of the brushes caused by the localization of the EOS body force away from the location of the wall-imparted drag force. For the brush-free nanochannels, the EDL and hence the EOS body force is localized at the same location as the wall-induced drag [see Fig. 3.1(a)] and hence such augmentation in the velocity field is not possible. For a larger salt concentration, the EDL is thinner. Therefore this effect of the EDL localization becomes even stronger. For a more diffuse EDL (corresponding to smaller salt concentration), the EDL will spread out to near-wall locations, nullifying this overall effect of the EDL localization. As a consequence, $u_r$ is larger for a larger salt concentration (also see Fig. 3.3), with the exception of long brushes($\ell$=10 nm) at large salt concentration($c_\infty = 10^{-2} - 10^{-1}$ M) and high $pH_\infty$. The third important result in this context is the significant gradient in the velocity for the brush-grafted nanochannels for small $\ell$ or large $pH_\infty$ (i.e., the conditions that cause a larger brush height, see [118, 119]). The larger brush height imparting a drag over a larger distance from the wall enforces such a gradient in the originally plug-like EOS flow

profile (always witnessed for the brush-free nanochannels).

In Fig. 3.3, we compare the ratio $u_r$ (defined previously). $u_r$ profile confirms an extraordinary enhancement of the centreline velocities (or equivalently the generation of ultrafast water transport with $u_r > 10$ for several cases) for the brush-grafted nanochannels. Finally in the inset of Fig. 3.3, we provide the ratio $Q_r = Q_B/Q_{NB}$ (where $Q_B = w\int_{-h}^{h} u_B dy$ and $Q_{NB} = w\int_{-h}^{h} u_{NB} dy$ are the volume flow rates in brush-grafted and brush-free nanochannels, $w$ is the nanochannel width, and $u_B$ and $u_{NB}$ are the velocity fields in brush-grafted and brush-free nanochannels). $Q_r$ also shows an equally impressive increase and can even become $> 10$ for certain parameter choices. For the studied set of parameters, both $u_r$ and $Q_r$ show the maximum enhancement for the nanochannel ($h = 250$ nm) with very tall (corresponding to small $\ell$ and large $pH_\infty$) PE brushes at intermediate salt concentration ($c_\infty = 10^{-2}$ M). Of course, for such very tall brushes (corresponding to $\ell$=10 nm and $pH_\infty = 4$) at large salt concentration, the effect of EDL localization is superceded by the corresponding decrease in the brush height (due to enhanced inter-segmental screening). As a result, $u_r$ and $Q_r$ decreases in the range $c_\infty = 10^{-2} - 10^{-1}$ M. On the other hand, for other cases of not so tall brushes, $u_r$ and $Q_r$ increases monotonically with the salt concentration due to the dominating influence of the EDL localization effect.

In a recent study [30], we found an increase in the EOS velocity for nanochannels grafted with *end-charged* PE brushes. In Fig. 3.4, we compare $Q_r$ and the flux of the present study with that of the study of Ref. [30]. We clearly find that the present case shows a larger value of $Q_r$ and the flux. The previous study [30]

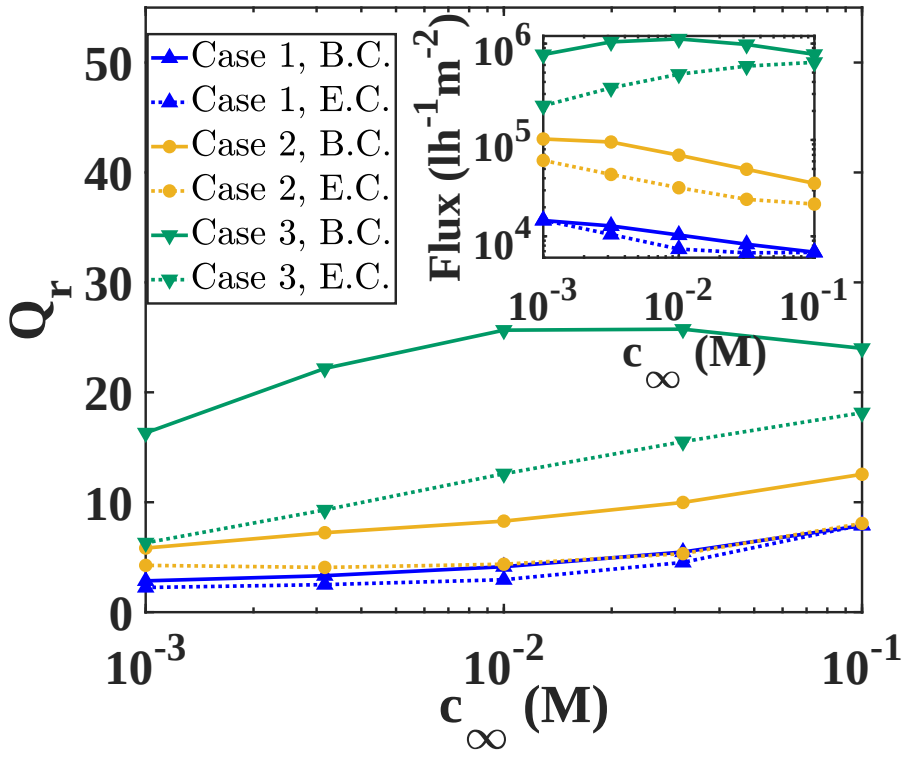


*Fig. 3.4:* Comparison of the ratio $Q_r$ and the actual flux value (see the inset) between the present case (EOS transport in nanochannels grafted with backbone-charged brushes) and Ref. 18 (EOS transport in nanochannels grafted with end-charged brushes). We consider three cases in the main figure: Case 1: $pH_\infty = 3$, $\ell$=60 nm, $h$=100 nm; Case 2: $pH_\infty = 4$, $\ell$=60 nm, $h$=100 nm; Case 3: $\mathrm{pH}_\infty = 4$, $\ell$=10 nm, $h$=250 nm. In the inset we compare the actual flux values for these three cases for an applied electric field $E$=500 V.cm$^{-1}$. In order to ensure that we are considering the same charge content of the PE brushes as the present case, the charge density for the end-charged PE brushes is considered to be $\sigma_{c,eq}$ (see the discussions following eqs. 1 and 2 for the definition of $\sigma_{c,eq}$). In the legend, "B.C" and "E.C" denote the cases of EOS transport in nanochannels grafted with backbone-charged (present case) and the end-charged (Ref. 18) brushes.

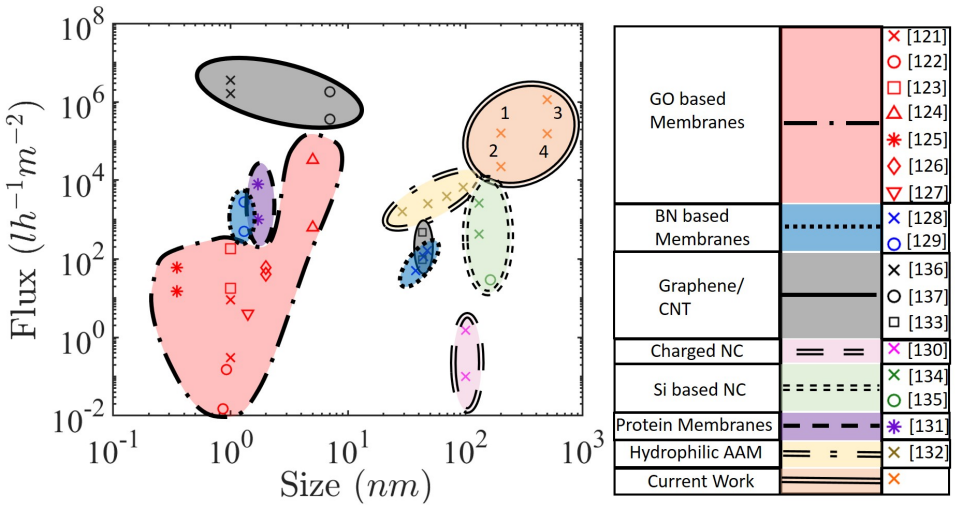


*Fig. 3.5:* Comparison of flux for various nanofluidic devices. Points 1 to 4 provide the results for the present case of PE-brush-grafted nanochannel. 1:pH$_\infty$ = 3, $c_\infty$ = $10^{-2}$ M, $\ell$ = 10 nm, $h$ = 100 nm, $E$ = 500 V.cm$^{-1}$; 2:pH$_\infty$ = 3, $c_\infty$ = $10^{-3}$ M, $\ell$ = 10 nm, $h$ = 100 nm, $E$ = 100 V.cm$^{-1}$; 3:pH$_\infty$ = 4, $c_\infty$ = $10^{-2}$ M, $\ell$ = 10 nm, $h$ = 250 nm, $E$ = 500 V.cm$^{-1}$; 4:pH$_\infty$ = 4, $c_\infty$ = $10^{-3}$ M, $\ell$ = 10 nm, $h$ = 250 nm, $E$ = 100 V.cm$^{-1}$. For the current work, $\eta = 8.9 \times 10^{-4}$ Pa.s, all other parameters are same as Fig. 3.2. In Table 3.1, we discuss the manner in which the fluxes are for the different experimental studies (cited here) are calculated. Here GO - Graphene Oxide, BN - Boron Nitride, CNT - Carbon Nanotube, Si - Silicon, AAM - Anodized Alumina Membrane, NC - Nanochannel.

considered a simplistic model of the PE brushes, where the brushes were described using the Alexander-de-Gennes model making the monomers uniformly distributed along the length of the brush. On the other hand, for the present case we invoke a much more rigorous and realistic model where the brushes are described using the augmented SST [118]: this leads to a more appropriate distribution of the monomers where the monomer density is much larger at near-wall locations than at locations far away from the wall. In both the present and the previous studies [30], we attribute the increase in fluxes to the localization of the EDL charge density and the resulting EOS body force away from the wall (which is the location of the wall-induced drag force). Such localization of the EOS body force away from the location of wall-induced drag force leads to a much larger effect of the EOS body force causing such enhancement in the fluxes. In addition to this wall-induced drag, there is also the drag force resulting from the presence of the brushes themselves. The coefficient of the brush-induced drag force varies quadratically with the monomer distribution (see the discussions following eq. 1). The simplistic model of our previous paper [30] assumes a uniform monomer distribution; hence it has the same number of monomers (and hence the same drag coefficient) at near-wall location as well as the location where the EOS body force is localized. On the other hand, for the present case, the consideration of a much more rigorous and realistic monomer distribution implies that the monomer distribution is significantly larger at near-wall locations and hence significantly weaker at the location where the EOS body force is localized (i.e., at a location away from the wall). Accordingly, for the present case, at the locations where the EOS body force is effectively localized, the

coefficient of the brush-induced drag force is significantly smaller. *In other words, for the present case the EOS body force is localized at a location that is significantly deviated from the location of both the wall-induced and the brush-induced drag forces, while for the previous study [30] the EOS body force is localized at a location that is only deviated from the location of the wall-induced drag force but not from the location of the brush-induced drag force.* This in turn ensures a much larger value of the flux and $Q_r$ for the present case as compared to our previous study [30].

Finally in Fig. 3.5, we seek answer to the following question: *How large is the flux in the brush-grafted nanochannels in the context of the large volume of studies on nanofluidic transport?* For that purpose, we try to compare the fluxes obtained for the brush-grafted nanochannels against the fluxes obtained in different nanochannel-based membranes, nanotubes, and nanofluidic systems (or isolated nanochannels). Most remarkably, the fluxes for the present case is remarkably high: we provide the results for different nanochannel height, brush height, and applied (and experimentally feasible) axial electric field combinations (see Table 1 for all the relevant details). and find that the fluxes in the PE-brush-grafted nanochannels can be much larger than that for a wide variety of different nanofluidic or nanochannel-membrane systems. In fact, the fluxes are so large that they become comparable (or slightly smaller) than the fluxes obtained in CNTs or nanoporous single-layer graphene known for extremely large flow velocities.

## *3.4 Conclusions*

To summarize, we have shown the attainment of the superfast EOS water transport in nanochannels by grafting nanochannels with pH-responsive, PE brushes. This enhancement makes the corresponding water flux much larger than the water flux obtained with most of the state-of-the-art nanofluidic and nanochannel-membrane systems. Such a finding establishes that brush functionalization, completely contrary to the general notion of the universal flow-reducing ability of the brushes, can serve as a strong promoter of the nanofluidic transport for a wide range of parameter values. Of course, for other parameter combinations (not studied here), the brush functionalization might retard the transport. The universal need to achieve enhanced transport and enhanced separation in nanochannels via energy efficient means cuts across the disciplines of fluid mechanics, materials science, biotechnology, nanotechnology, separation science, etc. We have achieved precisely that in this study by the facile means of PE brush functionalization.

## *3.5 Appendix*

| **Reference** | **Material** | **Pore Space (nm)** | **Flux** ($lm^{-2}h^{-1}$) | **Notes** |
|---|---|---|---|---|
| Chong et al. [121] | GO membrane | 1 | 0.3-9 | This flux is calculated by using the capillary pressure in the GO membrane to be 6 bar (see Fig. 1d in [121]) |
| Zhou et al. [122] | GO membrane | 0.86-0.92 | 0.015-0.15 | This flux corresponds to a flux of 150 $gm^{-2}h^{-1}$ (see Fig. 1f in [122]) |
| Chong et al. [123] | GO membrane | 0.7-1.4 ($\sim 1$) | 18-180 | This flux is calculated by using the 10 bar pressure (Fig. 5 in [123]) |
| Liu et al.[124] | Nanostrand-channelled graphene oxide membranes | 3-5 | 625-33000 | See Fig. 3a and the result for flux at 1.5 MPa pressure in [124] |
| Han et al. [125] | Free-standing ultrathin rGO membrane | 0.35 | 15-60 | See Fig. 3A in [125] |

| | | | | |
|---|---|---|---|---|
| Huang et al. [126] | Graphene Oxide Nanofiltration Membrane Intercalated by CNT | 0.5-2 | 40 – 60 | We obtain this flux by multiplying the pressure (5 bar) with the flux data (see Table 1 in [126]) |
| Yang et al. [127] | Ultrathin graphene-based membrane | 1.25-1.5 | 0.3-4 | See Fig. 2b for water. The pressure is 1 bar (see the Methods section in [127]) |
| Tang et al. [128] | Polysulfone (PSf)-based mixed matrix membranes (MMMs) incorporated with two-dimensional boron nitride nanosheet (BNNS) | 34.5-47.5 | 49.32-160.28 | See Table 3 in [128]. The variation in the flux is due to the variation in the BNNS percentage content of the matrix |
| Chen et al. [129] | Functionalized boron nitride (FBN) membranes | 0.8-1.8 | 500 - 2800 | See Fig. 3b in [129]. The value is for water. The experiments are conducted with a pressure of 1 bar. The variation in the flux is due to the variation in the FBN membrane thickness |

| | | | | |
|---|---|---|---|---|
| Surwade et al. [136] | Nano-porous Single Layer Graphene | D $\sim$ 1 | $1.6 \times 10^6$ - $3.6 \times 10^6$ | Initial flux given as $7 \times 10^{-15}$ g $s^{-1}$ $atm^{-1}$ per pore with pressure difference of 50 atm. Flux given as $\sim 1 \times 10^6$ g.$m^{-2}s^{-1}$. |
| Majumder et al. [137] | CNT | D = 7 | $3.6 \times 10^5$ – $1.8 \times 10^6$ | See Table 1 in [137]. Calculated from velocities |
| Whitby et al. [133] | Nanoscale carbon pipes | 40-45 | 100-600 | We have a maximum total water flow rate of 0.15 ml/min (see Fig. 4 in [133]).Number of pores in measured area (1 $cm^2$) = $1.07 \times 10^{10}$. Flow in a single pore = $\frac{0.15ml/min}{1.07 \times 10^{10}}$. |
| Yang et al. [130] | 3.5 (PSS/PAH) coated 100 nm nano-channel membranes | 100 | 0.1-1.5 | Calculated from a flux value of 120 $\mu$ mol/min (See Fig. 6 in [130]) |
| Mathwig et al. [134] | Silicon nitride nanochannels | 2h = 130 | 430-2585 | Flow rate for a single channel is 28 pL/min (see Fig. 5 in [134]). Therefore the flux is $\frac{28 \times 10^{-12} \times 60}{(w \times 2h)}$ = $\frac{28 \times 10^{-12} \times 60}{(5 \times 10^{-6}) \times (130 \times 10^{-9})} \approx 2585$ |
| Lee et al. [135] | Si chips | 2h = 163 | 29.5 | Flow rate for a single channel is 400 fL/min (see Fig. 2 in [135]). Therefore the flux is $\frac{400 \times 10^{-15} \times 60}{(w \times 2h)}$ = $\frac{400 \times 10^{-15} \times 60}{(5 \times 10^{-6}) \times (163 \times 10^{-9})} \approx 29.5$ |

| | | | | |
|---|---|---|---|---|
| Peng et al. [131] | Water permeation through protein membranes | D ∼1.7 | 1000-8000 | See Fig. 2b in [131] |
| Lee et al. [132] | Hydrophilic AAM | D = 30-100 | 1500-7000 | Calculated using enhancement factors (See Table 2 in [132]) |
| | Current Work | 2h = 200-500 | 1450-$1.12\times10^6$ | Based on velocity |

*Tab. 3.1:* Flux values obtained from experimental studies on liquid transport in different nanofluidic systems.

# Chapter 4: Ionic diffusioosmotic transport in nanochannels grafted with pH-responsive polyelectrolyte brushes modeled using augmented strong stretching theory

*In this chapter*[1]*, we study the diffusioosmotic (DOS) transport in a nanochannel grafted with pH-responsive polyelectrolyte (PE) brushes and establish brush-functionalization-driven enhancement in induced nanofluidic electric field and electrokinetic transport. The PE brushes are modelled using our recently developed augmented strong stretching theory (SST). We consider the generation of the DOS transport due to the imposition of a salt concentration gradient along the length of the nanochannel. The presence of the salt concentration gradient induces an electric field that has an osmotic (associated with the flow-driven migration of the ions in the induced electric double layer) and an ionic (associated with the conduction current) component. These two components evolve in a manner such that the electric field in the brush-grafted nanochannel is larger (smaller) in magnitude*

[1] Contents of this chapter have been published as: *V. S. Sivasankar, S. A. Etha, H. S. Sachar, and S. Das, "Ionic diffusioosmotic transport in nanochannels grafted with pH-responsive polyelectrolyte brushes modeled using augmented strong stretching theory", Phys. Fluids 32, 042003 (2020).*

*than that in the brush-less nanochannels for the case where the electric field is positive (negative). Furthermore, we quantify the DOS flow velocity and establish that for most of the parameter choices, the DOS velocity, which is a combination of the induced pressure-gradient-driven chemiosmotic component and the induced electric field driven electroosmotic transport, is significantly larger for the nanochannels grafted with backbone-charged PE brushes (i.e., brushes where the charge is distributed along the entire length of the brushes) as compared to brush-free nanochannels or nanochannels grafted with PE brushes containing charges on their non-grafted ends.*

## *4.1 Introduction*

Liquid and ion transport in nanochannels and nanopores [15,102–104,140,141] is central to a variety of emerging applications in energy research [105,106], development of ionic sensors, biosensors, and ionic gating [83,107–109], fabrication of novel biomedical and drug delivery platforms [142,143], as well as our endeavor to better understand a myriad of biological systems for fabricating different biomimetic systems [110,111]. Several strategies have been devised to enhance the electrohydrodynamic fluxes in nanochannels and nanopores. These strategies involve tuning the external forces (e.g., electric field and magnetic field) driving the transport and/or functionalizing the walls of these nanochannels/nanopores with entities that interplay with the liquid and ions that are being transported. For example, in a recent work, an enhanced electro-osmotic (EOS) flux was reported in a charged nanochan-

nel with alternating slipping surface [144]. Other recent related studies report enhancement in flow by controlling the zeta potential, wall slip coefficient [145], and aspect ratio of pH-regulated nanochannel [146]. Functionalizing micro-nanochannels by grafting their inner walls with environmental-stimuli sensitive polymer and polyelectrolyte (PE) molecules has emerged as an extremely popular strategy that have found applications in a large number of disciplines ranging from ion sensing and biosensing [112, 113] to fabrication of diodes and current rectifiers [34, 39, 114, 147]. For instance, in a recent study, Sadhegi discussed the manipulation of EOS flow velocity by varying thickness of the Polyelectrolyte layer (PEL) coating in a microchannel [148]. These polymer and PE molecules are often grafted densely enough so that they stretch out away from the grafting surface forming "brush"-like configurations [3–5, 7–9, 149, 150]. These brushes change their configurations as functions of the ion concentration and pH of the solution and accordingly enabling the micro-nanochannels to be employed for such wide variety of applications.

While there has been extensive research on probing the behavior of the PE brushes and their responses to different factors (e.g., salt concentration, pH, and solvent quality) [21, 48–50, 52, 52–56, 58–64], significantly less has been done in probing the electrohydrodynamic (EHD) transport in such PE-brush-functionalized nanochannels. The initial group of studies effectively considered a decoupled problem: they probed the EHD transport in such nanochannels assuming a constant (pH and salt concentration independent) brush height and monomer distribution [22–26, 28, 87, 151–159]. The brush height and the monomer distribution severely affect the fluid flow. Disregard of the dependence of these parameters on the salt

concentration and pH meant that the appropriate dependence of the fluid flow on salt concentration and pH also got disregarded. In order to address these lacunae, Das and co-workers in a series of recent papers [30–32, 57], considered for the first time a simplistic yet coupled EHD model on PE-brush-grafted nanochannel where the salt concentration dependence of the brush height was accounted for. The model was simplistic in the sense that it considered end-charged PE brushes with the brushes being modelled using the Alexander-de-Gennes model [4, 5] (where one considers a uniform monomer density along the length of the brush). In a couple of recent studies, Das and co-workers extended their theory to probe the EHD transport in such PE-brush-grafted nanochannels with the brushes being modelled by the augmented Strong Stretching Theory (SST) [118, 160]. This augmented SST was recently developed by Das and co-workers [119] and improved the well-known SST for the PE brushes [59–62] (used for modelling the thermodynamics, configuration, and electrostatics of the PE brushes) by accounting for the influence of the excluded volume interactions and a more complete form of the mass action law. These studies [118, 160], therefore, represent the most comprehensive theoretical analysis of the problem of EHD transport in brush-grafted nanochannels till date where the brushes have been appropriately modelled and an appropriate connection between the brush configuration and the EHD transport has been considered.

In this paper, we study the diffusioosmotic (DOS) transport in nanochannels grafted with the pH-responsive PE brushes modelled using our recently developed augmented SST [118, 119, 160]. The DOS transport, which is a form of induced electro-soluto-hydrodynamic transport, is triggered here by applying a salt concen-

tration gradient along the length of the nanochannel. The presence of this gradient interplays with the charge distribution and the charge imbalance of the electric double layer (EDL). As a consequence, there is the generation of an induced electric field. This electric field interacts with the EDL charge density and induces (and also gets influenced by) an electroosmotic (EOS) transport. Additionally, the imposed salt concentration gradient induces a pressure-gradient and there is a resulting pressure-driven transport, which is also referred to as a chemiosmotic (COS) transport. Therefore, the DOS effect is a manifestation of three things: generation of an induced electric field, generation of a pressure gradient, and generation of liquid transport that is a combination of the EOS and COS transport. There has been extensive previous studies probing the DOS transport either by the imposition of a salt concentration gradient [161–172] or an uncharged solute gradient [135,173–179]. In addition to giving rise to the highly intriguing fluid mechanics of induced electro-soluto-hydrodynamic DOS transport, such DOS transport has been extensively employed for a large number of applications ranging from triggering microfluidic and interfacial transport [175,178] to designing novel strategies for sensing [179], phase separation [180], and particle manipulation [181]. In a recent study, Hoshyargar et al. studied the diffusioosmotic flow of an analyte solution in a charged microchannel and discussed its potential application in the separation of analytes [180]. In fact, in our recent study [31], we probed the DOS transport in nanochannels grafted with the end-charged PE brushes with the brushes being described by the simplistic Alexander-de-Gennes model [4,5]. In the present paper, we consider a much more realistic system, where the brushes contain charges along their entire backbone and

these charges are pH-responsive. More importantly, the brushes are modelled using the augmented SST. Such a description ensures that we are considering the most advanced description till date of an induced EHD transport (namely DOS transport) in a pH-responsive PE-brush-grafted nanochannel.

Our results firstly establish that the presence of the PE brush grafting significantly enhances (with respect to the brush-free nanochannels having identical charge content as the brush-grafted nanochannels) the diffusioosmotically-induced electric field for all the different choices of the salt concentration, pH, and grafting density values. This induced electric field is a combination of the osmotic component (electric field developed due to the downstream migration of the EDL ions in presence of the background DOS transport) and the ionic component (electric field that is generated due to the conduction current). We perform detailed analysis to show the relative variation of these individual components (osmotic and ionic) of the electric field as functions of the strength of the DOS transport, localization of the EDL charge density by the brushes away from the nanochannel wall enforcing a larger magnitude of the background flow to be responsible for the downward osmotic migration of the ions [118], and the varying diffusivity of the positive and negative ions (dictating different strengths of the cationic and anionic conduction). These analyses explain such augmented electric field generation by the brush-grafted nanochannels, establishing brush-grafting as a novel mechanism for inducing (through the facile route of applying a salt concentration gradient) energetically favorable scenarios. The second key finding of this study is the discovery that the DOS water transport is significantly enhanced in presence of the brush grafting for most of the parameter

combination. We explain that the DOS transport is a combination of the induced pressure-driven transport (triggered by the pressure gradient induced by the applied salt concentration gradient) also known as the chemiosmotic (COS) transport and the induced electroosmotic (EOS) transport triggered due to the induced electric field. For the choice of the positive value of the salt concentration gradient, the induced pressure-gradient is negative triggering a COS liquid transport from right-to-left in the nanochannel. The EOS transport, therefore, augments (retards) the COS transport for cases where the induced electric field is negative (positive) triggering an EOS transport from right-to-left (left-to-right) in the nanochannel. Such an understanding, coupled with the knowledge that the the presence of the brushes localizes the EOS body force away from the nanochannel wall and ensures a larger manifestation of the effect of the EOS body force, helps to explain the overall DOS velocity profiles in brush-grafted and brush-free nanochannels. For this case too, the brushes emerge as an enabler of a significant increase in the overall DOS nanofluidic water transport. Finally, we provide a thorough comparison between the present study and our previous study [31]. Both these studies probe the DOS transport in brush grafted nanochannel; however, while the present study considers the brushes to be backbone-charged (i.e., containing charges distributed along their entire backbone), our previous study [31] considered brushes that contain charges only at their non-grafted ends. The comparison reveals that for most of the parameter choices, the strength of the DOS velocity is significantly larger for the present case: we associate such an occurrence to the significantly smaller brush-induced drag force at the location where the different driving forces (EOS and COS body forces) are localized,

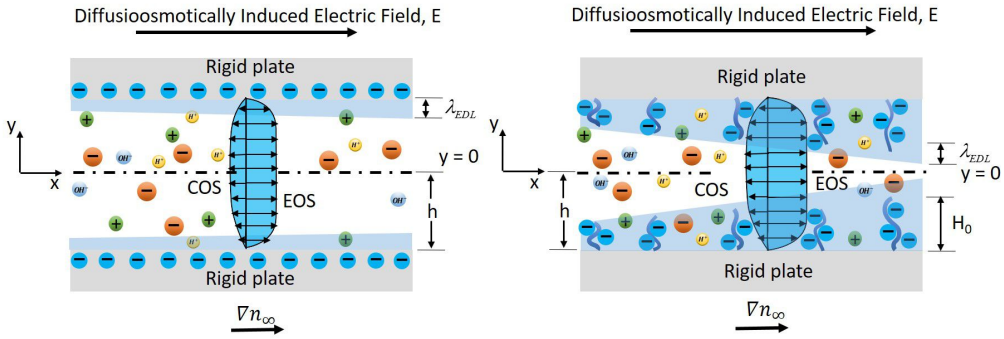


*Fig. 4.1:* Schematic representing the salt concentration gradient induced flow in a) Brush free nanochannel b) Backbone charged PE brush grafted nanochannel. The schematic shows a typical situation where the COS and the EOS flows oppose each other for the case where the diffusioosmotically induced electric field is positive (i.e., from left to right). The other situation, where the COS and the EOS flows support each other with the diffusioosmotically induced electric field being negative (i.e., from right to left) is equally possible.

as compared to that of the present study. Therefore, the present study establishes that functionalizing nanochannels with backbone-charged PE brushes indeed leads to a significantly enhanced (diffusioosmosis) form of induced electrokinetic nanofluidic transport as compared to either brush-free nanochannels or nanochannels grafted with end-charged PE brushes.

## *4.2 Theory*

We consider the ionic DOS transport in a nanochannel of half height $h$ and length $L$ and grafted with backbone-charged, pH-responsive PE brushes [see Fig.

4.1(b)]. The nanochannel walls do not contain any charge. This implies that $\sigma$, which is the net charge density at the wall is zero; given that $\sigma \propto d\psi/dy$ (where $\psi$ is the EDL electrostatic potential), at the nanochannel wall, $d\psi/dy = 0$. On the other hand, all the charges are present on the brushes. The nanochannel is connected to microfluidic reservoirs (not shown in the schematic). $n_\infty$ and $n_{H^+,\infty}$ are the bulk number densities of the electrolyte salt ions and $H^+$ ions inside these reservoirs. We model the PE brushes using our recently developed augmented SST [118, 119, 160]. Use of such a model decides the brush height, the monomer distribution along the length of the brush, and the corresponding EDL electrostatic potential distribution in a thermodynamically self-consistent fashion. Consequently, the model for the DOS transport includes these thermodynamically self-consistent description of the brush height, monomer distribution, and the ion distribution. We consider that the ionic DOS transport is generated by employing a constant axial concentration gradient of the salt ions, namely $\nabla n_\infty = dn_\infty/dx$. Here $dn_\infty/dx$ is so chosen that $L\frac{dn_\infty}{dx}/n_\infty \ll 1$. The presence of this $dn_\infty/dx$ implies that the brush height, the monomer distribution along the brush height, the corresponding drag coefficient that depends on the monomer distributions, and the electrostatic potential and the ion distributions within the brush-induced EDL will all have a weak gradient in the axial direction. The DOS transport is quantified by the corresponding diffusioosmotically-induced electric field and the DOS velocity field. The DOS velocity is a combination of the COS flow (generated by the induced pressure-gradient) and the electroomsotic (flow) (generated by the diffusioosmotically-induced electric field) [see Fig. 4.1(b)]. In this paper, such diffusioosmotically-induced electric

field and the DOS velocity field for the brush-grafted nanochannel are compared with those in brush-free nanochannels having identical surface charge as that of the brush-grafted nanochannels. In this section, we provide the theory for the DOS transport in such brush-grafted nanochannels.

### *4.2.1 DOS transport in brush-grafted nanochannels*

The flow in the nanochannel is triggered by applying a salt concentration (or salt number density) gradient along the length of the channel, as discussed earlier. The resulting flow is considered to be steady, fully developed, and unidirectional. The DOS transport of the electrolyte in the nanochannel is governed by the following Navier Stokes (NS) equations. The pressure field is obtained from the NS equation in $y$-direction and by using the Boltzmann distributions [see eqs.(6-8)] for the ion number densities:

$$\begin{aligned}
&\frac{\partial p}{\partial y} + e(n_+ - n_- + n_{H^+} - n_{OH^-})\frac{\partial \psi}{\partial y} = 0 \Rightarrow \\
&\partial p = -k_B T(n_+ - n_- + n_{H^+} - n_{OH^-})\partial \bar{\psi} \Rightarrow \\
&p = p_{atm} + 2k_B T(n_\infty + n_{H^+,\infty})(cosh(\bar{\psi}) - 1). \qquad (4.1)
\end{aligned}$$

In the above equation, $\bar{\psi} = e\psi/(k_B T)$. Also, $n_{+,\infty} = n_\infty$, $n_{-,\infty} = n_\infty + n_{H^+,\infty} - n_{OH^-,\infty}$, where $n_\infty = 10^3 N_A c_\infty$, and $n_{H^+,\infty} = 10^{3-pH_\infty} N_A$, $n_{OH^-,\infty} = 10^{3-pOH_\infty} N_A$ ($pOH_\infty = 14 - pH_\infty$). This also implies $\nabla n_\infty = \frac{dn_\infty}{dx} = \frac{dn_{+,\infty}}{dx} = \frac{dn_{-,\infty}}{dx}$. The starting point of eq.(4.1) comes from the simplification of the y-momentum conservation equation by considering the *Space Charge Theory* [182–185] (please see the Appendix for more details). Consequently, in presence of the applied axial gradients

in electrolyte ion concentrations, we can write:

$$\frac{\partial p}{\partial x} = 2k_B T \frac{dn_\infty}{dx}\left[\cosh\left(\bar{\psi}\right) - 1\right] + 2k_B T(n_\infty + n_{H^+,\infty})\left[\sinh\left(\bar{\psi}\right)\frac{\partial \bar{\psi}}{\partial x}\right]. \tag{4.2}$$

This pressure-gradient, as can be seen, is dictated by the imposed gradient in the salt concentration.

The x-momentum equation, on the other hand, for the bottom half of the nanochannel can be expressed as (considering a steady and fully-developed flow):

$$\begin{aligned}
\eta\frac{\partial^2 u}{\partial y^2} &= \frac{\partial p}{\partial x} + \frac{\eta}{\kappa_d}u - e(n_+ - n_- + n_{H^+} - n_{OH^-})(E - \frac{\partial \psi}{\partial x}) \quad (-h \le y \le -h + H_0), \\
\eta\frac{\partial^2 u}{\partial y^2} &= \frac{\partial p}{\partial x} - e(n_+ - n_- + n_{H^+} - n_{OH^-})(E - \frac{\partial \psi}{\partial x}) \quad (-h + H_0 \le y \le 0).
\end{aligned} \tag{4.3}$$

In eq.(4.3), $u$ is the velocity profile, $\eta$ is the dynamic viscosity of the electrolyte, $E$ is the induced electric field, $\frac{\partial p}{\partial x}$ is the pressure gradient induced due to the employed salt concentration gradient [expressed in eq.(4.2)] and $\kappa_d = a^2/\phi(y)^2 = a^2\left(\frac{H_0}{\sigma a^3 N \bar{\phi}}\right)^2$. Here $\bar{\phi} = \frac{\phi H_0}{\sigma a^3 N}$ is the normalized profile for the monomer distribution $\phi$ [expressed in eq.(2.30) using the augmented SST calculations]. Eq.(4.3) establishes that there are two driving forces for the DOS transport: the induced pressure gradient that drives an induced chemiosmotic transport and the induced electric field that drives an induced electroosmotic transport. $\kappa_d$, which is inversely related to the drag coefficient can be obtained from the works of de Gennes [138] and Freed and Edwards [139]. These works [138, 139] showed that the drag coefficient varies as $K^2$, where $K^{-1}$ is the length that screens the flow inside the polymer coil in a semi-dilute polymer solution. Given that for this problem too the flow inside the brushes is

significantly lowered as compared to that outside the brushes, we can use this theory of de Gennes [138] and Freed and Edwards [139], to express the drag coefficient in terms of $K^{-1}$. As $\kappa_d$ varies inversely as the drag coefficient, we can write $\kappa_d \sim K^{-2}$. Furthermore, $K \sim \phi/a$. Therefore, $\kappa_d \sim a^2/\phi^2$.

Using eq.(4.2), we can re-write eq.(4.3) in dimensionless form as:

$$\begin{aligned}
\frac{\partial^2 \bar{u}}{\partial \bar{y}^2} &= A\bar{n}_1'(cosh(\bar{\psi}) - 1) + \frac{h^2}{\kappa_d}\bar{u} + A(1 + \bar{n}_{H^+,\infty}) \sinh(\bar{\psi})\bar{E} \quad (-1 \le \bar{y} \le -1 + \bar{H}_0), \\
\frac{\partial^2 \bar{u}}{\partial \bar{y}^2} &= A\bar{n}_1'(cosh(\bar{\psi}) - 1) + A(1 + \bar{n}_{H^+,\infty}) \sinh(\bar{\psi})\bar{E} \quad (-1 + \bar{H}_0 \le \bar{y} \le 0). \qquad (4.4)
\end{aligned}$$

In eq.(4.4), $\bar{u} = \frac{u}{U}$, $A = \frac{2k_BTn_\infty h^2}{\eta UL}$, $\bar{n}_1' = L\frac{dn_\infty}{dx}/n_\infty$, $U = \frac{2k_BT\lambda^2}{\eta}(\frac{dn_\infty}{dx})$, $\bar{\psi} = \frac{e\psi}{k_BT}$, $\bar{E} = \frac{E}{E_0}$, where $E_0 = \frac{k_BT}{eL}$ is the scale of electric field, $\bar{n}_{i,\infty} = \frac{n_{i,\infty}}{n_\infty}$ (i=$\pm$, $H^+$, $OH^-$), $\bar{y} = \frac{y}{h}$, $\bar{H}_0 = \frac{H_0}{h}$, $\bar{\lambda} = \frac{\lambda}{h}$, and $\lambda = \sqrt{\epsilon_0\epsilon_r k_BT/(2e^2(n_\infty + n_{H^+,\infty}))}$ is the Debye screening length of the electric double layer (EDL).

In order to solve for $\bar{u}$ from eq.(4.4), we need to first obtain the dimensionless electric field $\bar{E}$. The electric field $E$ is obtained from the condition:

$$\int_{-h}^{h} (J_+ + J_{H^+} - J_- - J_{OH^-})\, dy = 0, \qquad (4.5)$$

where $J_+$ and $J_-$ are the fluxes of the electrolyte cation and anion and $J_{H^+}$ and $J_{OH^-}$ are the ionic fluxes of the $H^+$ and $OH^-$ ions. We can express these fluxes as follow:

$$J_\pm = -D_\pm \left[\frac{\partial n_\pm}{\partial x} \pm \frac{e}{k_BT} n_\pm (\nabla\psi - E)\right] + n_\pm u, \qquad (4.6)$$

$$J_{H^+} = -D_{H^+} \left[\frac{\partial n_{H^+}}{\partial x} + \frac{e}{k_BT} n_{H^+} \left(\frac{\partial \psi}{\partial x} - E\right)\right] + n_{H^+} u, \qquad (4.7)$$

$$J_{OH^-} = -D_{OH^-} \left[\frac{\partial n_{OH^-}}{\partial x} - \frac{e}{k_BT} n_{OH^-} \left(\frac{\partial \psi}{\partial x} - E\right)\right] + n_{OH^-} u.$$

In the above equations, $D_i$ are the diffusivities of species $i$ ($i = \pm, H^+, OH^-$).

Using eqs.(4.6,4.7,4.8) as well as eqs.(2.18-2.20) in eq.(4.5), we can eventually obtain the dimensionless electric field as:

$$\begin{aligned}\bar{E} =& \frac{Pe\int_{-1}^{1}\bar{u}\Big[-\bar{n}_{+,\infty}\exp(-\bar{\psi})+\bar{n}_{-,\infty}\exp(\bar{\psi})-\bar{n}_{H^+,\infty}\exp(-\bar{\psi})+\bar{n}_{OH^-,\infty}\exp(\bar{\psi})\Big]d\bar{y}}{\int_{-1}^{1}\Big[R_+\bar{n}_+ + R_-\bar{n}_- + R_{H^+}\bar{n}_{H^+} + R_{OH^-}\bar{n}_{OH^-}\Big]d\bar{y}} + \\ & \frac{\bar{n_1'}\int_{-1}^{1}\Big[R_+\exp(-\bar{\psi})-R_-\exp(\bar{\psi})\Big]d\bar{y}}{\int_{-1}^{1}\Big[R_+\bar{n}_+ + R_-\bar{n}_- + R_{H^+}\bar{n}_{H^+} + R_{OH^-}\bar{n}_{OH^-}\Big]d\bar{y}} \\ & = \bar{E}_{osm} + \bar{E}_{ion} = \bar{E}_{osm,+} + \bar{E}_{osm,-} + \bar{E}_{osm,H^+} + \bar{E}_{osm,OH^-} + \bar{E}_{p,ion} - \bar{E}_{m,ion}.\end{aligned} \tag{4.8}$$

where $\bar{E}_{osm} = \bar{E}_{osm,+} + \bar{E}_{osm,-} + \bar{E}_{osm,H^+} + \bar{E}_{osm,OH^-}$ with $\bar{E}_{osm,i}$ being the osmotic contribution associated with ion $i$ and $\bar{E}_{ion} = \bar{E}_{p,ion} - \bar{E}_{m,ion}$ (with $\bar{E}_{p,ion}$ and $\bar{E}_{m,ion}$ being the ionic components of the electric field associated with the positive and negative salt ions). Also, we can express this different components as (with $z_i$ being the valence of ion of type $i$):

$$\bar{E}_{osm} = \frac{Pe\int_{-1}^{1}\bar{u}\Big[-\bar{n}_{+,\infty}\exp(-\bar{\psi})+\bar{n}_{-,\infty}\exp(\bar{\psi})-\bar{n}_{H^+,\infty}\exp(-\bar{\psi})+\bar{n}_{OH^-,\infty}\exp(\bar{\psi})\Big]d\bar{y}}{\int_{-1}^{1}\Big[R_+\bar{n}_+ + R_-\bar{n}_- + R_{H^+}\bar{n}_{H^+} + R_{OH^-}\bar{n}_{OH^-}\Big]d\bar{y}}, \tag{4.9}$$

$$\bar{E}_{osm,i} = \frac{Pe\int_{-1}^{1}\bar{u}\Big[-\frac{z_i}{|z_i|}\bar{n}_{i,\infty}\exp(-\frac{z_i}{|z_i|}\bar{\psi})\Big]d\bar{y}}{\int_{-1}^{1}\Big[R_+\bar{n}_+ + R_-\bar{n}_- + R_{H^+}\bar{n}_{H^+} + R_{OH^-}\bar{n}_{OH^-}\Big]d\bar{y}}, \tag{4.10}$$

$$\bar{E}_{ion} = \frac{\bar{n}_1'\int_{-1}^{1}\Big[R_+\exp(-\bar{\psi})-R_-\exp(\bar{\psi})\Big]d\bar{y}}{\int_{-1}^{1}\Big[R_+\bar{n}_+ + R_-\bar{n}_- + R_{H^+}\bar{n}_{H^+} + R_{OH^-}\bar{n}_{OH^-}\Big]d\bar{y}}, \tag{4.11}$$

$$\bar{E}_{p,ion} = \frac{\bar{n}_1'\int_{-1}^{1}\Big[R_+\exp(-\bar{\psi})\Big]d\bar{y}}{\int_{-1}^{1}\Big[R_+\bar{n}_+ + R_-\bar{n}_- + R_{H^+}\bar{n}_{H^+} + R_{OH^-}\bar{n}_{OH^-}\Big]d\bar{y}}, \tag{4.12}$$

$$\bar{E}_{m,ion} = \frac{\bar{n}_1' \int_{-1}^{1} \left[ R_- \exp(\bar{\psi}) \right] d\bar{y}}{\int_{-1}^{1} \left[ R_+ \bar{n}_+ + R_- \bar{n}_- + R_{H^+} \bar{n}_{H^+} + R_{OH^-} \bar{n}_{OH^-} \right] d\bar{y}}. \tag{4.13}$$

In eq.(4.8), $Pe = \frac{UL}{D_+ + D_- + D_{H^+} + D_{OH^-}}$, is the Peclet number for the flow, $R_i = \frac{D_i}{D_+ + D_- + D_{H^+} + D_{OH^-}}$ is the dimensionless diffusivities of each species $i$, where $i = \pm$, $H^+$, $OH^-$. Eq.(4.8) expresses $\bar{E}$ in terms of $\bar{u}$. Therefore, if we use eq.(4.8) to replace $\bar{E}$ in eq.(4.4), we shall eventually get an integro-differential equation in $\bar{u}$. This resulting equation in $\bar{u}$ is solved numerically in presence of the following boundary conditions to obtain $\bar{u}$.

$$\begin{aligned} &(\bar{u})_{\bar{y}=-1} = 0; \ \left(\frac{\partial \bar{u}}{\partial \bar{y}}\right)_{\bar{y}=0} = 0; \quad (\bar{u})_{\bar{y}=(-1+\bar{H})^-} = (\bar{u})_{\bar{y}=(-1+\bar{H})^+}; \\ &\left(\frac{\partial \bar{u}}{\partial \bar{y}}\right)_{\bar{y}=(-1+\bar{H})^-} = \left(\frac{\partial \bar{u}}{\partial \bar{y}}\right)_{\bar{y}=(-1+\bar{H})^+}. \end{aligned} \tag{4.14}$$

## 4.3 Results and Discussions

### 4.3.1 Variation of the diffusioosmotically-induced electric field

We first study the variation of the diffusioosmotically-induced dimensionless electric field $\bar{E}$ with salt concentration $c_\infty$ in presence of an axially employed salt number density gradient $dn_\infty/dx$ (see Fig. 4.2). Results are shown for six different cases: three different cases of DOS transport in brush grafted nanochannels and three more cases of the DOS transport in brush-free nanochannel, having the same surface charge density as a given brush grafted nanochannel. For example, the three cases of the brush-grafted nanochannels are the following – case 1: $pH_\infty = 3$, $\ell = 60\ nm$; case 2: $pH_\infty = 3$, $\ell = 10\ nm$; case 3: $pH_\infty = 4$, $\ell = 60\ nm$. The three cases for the brush-free nanochannels will be the cases where the nanochannels have an

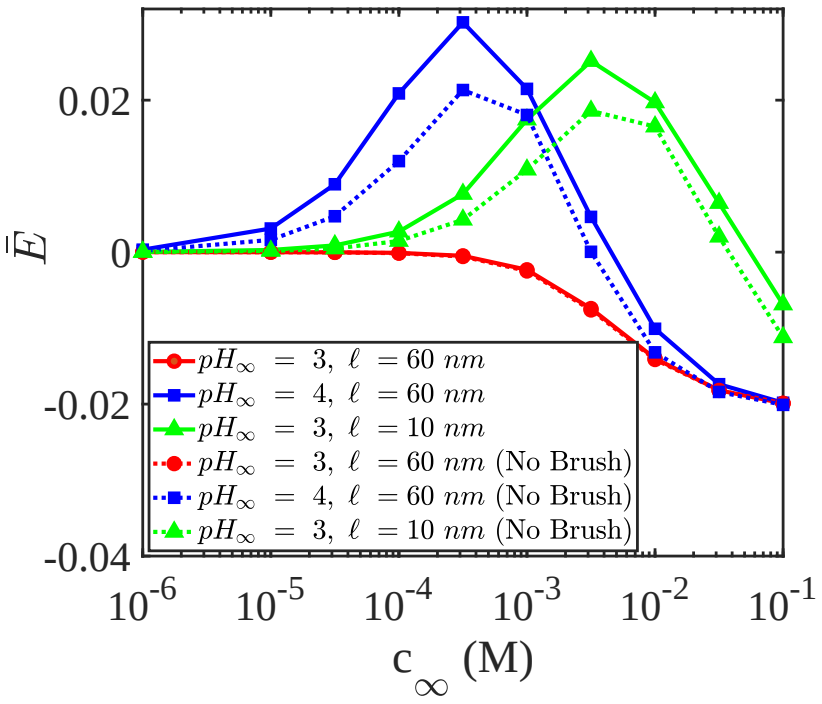


*Fig. 4.2:* Diffusioosmotically-induced electric field in presence of an applied concentration gradient of $\nabla n_\infty = dn_\infty/dx = 10^4 n_\infty$. The obtained electric field is calculated for the brush configuration using $N = 400$, $h = 100\,nm$, $a = 1\,nm$ (Kuhn length), $k_B = 1.38$ x $10^{-23} JK^{-1}$, $T = 298\ K$, $e = 1.6 \times 10^{-19}\ C$ (electronic charge), $\epsilon_0 = 8.8$ x $10^{-12}\ Fm^{-1}$(permittivity of free space), $\epsilon_r = 79.8$ (relative permittivity of water), $\gamma a^3 = 1$, $pK_a = 3.5$, $\nu = 0.5$, $\omega = 0.1$. Other parameters are $\bar{n}_1' = 0.1$, $D_+ = 1.330 \times 10^{-9}\ m^2/s$, $D_- = 2.030 \times 10^{-9}\ m^2/s$, $D_{H^+} = 9.310 \times 10^{-9}\ m^2/s$, $D_{OH^-} = 5.270 \times 10^{-9}\ m^2/s$ [186].

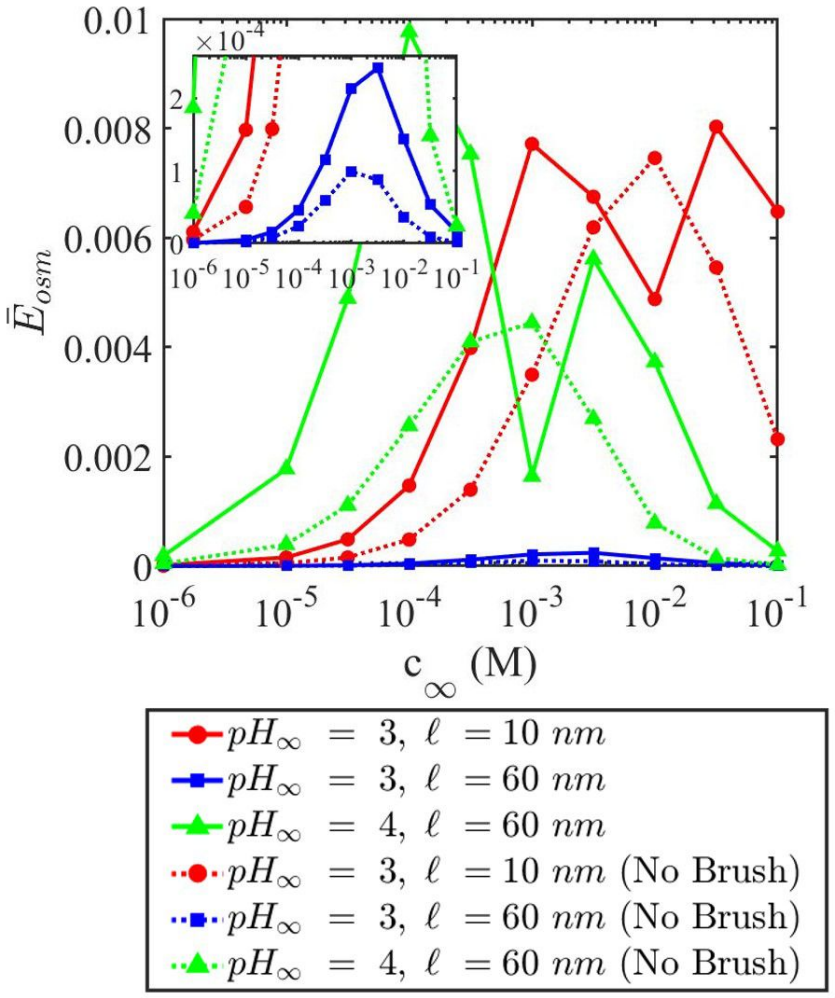


*Fig. 4.3:* Variation of the dimensionless osmotic ($\bar{E}_{osm}$) component of the diffusioosmotically-induced electric field with $c_\infty$ in presence of an applied salt number density gradient of $\nabla n_\infty = dn_\infty/dx = 10^4 n_\infty$. for both brush-grafted and brush-free nanochannels for different combinations of $\ell$ and $pH_\infty$ values. In the inset, we magnify the results for the case of $pH_\infty = 3,\ \ell = 60\ nm$ for both the cases of brush-free and brush-grafted nanochannels. Other parameters are identical to those used in Fig. 4.2.

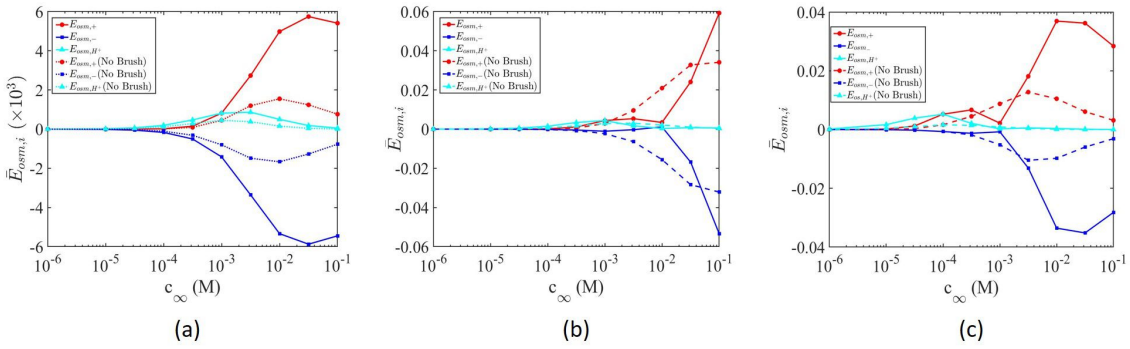


*Fig. 4.4:* Variation of the different components ($\bar{E}_{osm,i}$) of $\bar{E}_{osm}$ with $c_\infty$ shown for both brush-free and brush-grafted nanochannels for a) $pH_\infty = 3,\ \ell = 60\ nm$, (b) $pH_\infty = 3,\ \ell = 10\ nm$, and (c) $pH_\infty = 4,\ \ell = 60\ nm$. Other parameters are identical to those used in Fig. 4.2. In none of the subfigures, we show the contribution associated with the osmotic migration of $OH^-$ ions as it is very small.

equivalent surface charge density as that of a given brush-grafted nanochannel case: for example, "$pH_\infty = 3,\ \ell = 60\ nm$ (No Brush)" in the legend of Fig. 4.2, as well as in the legend of the subsequent figures, implies that we are considering the DOS transport in a brush-free nanochannel having the same surface charge density as the brush-grafted nanochannel with $pH_\infty = 3,\ \ell = 60\ nm$. This equality in the surface charge densities is ensured by employing the condition $\sigma_{c,eq} = -e\int_{-h}^{-h+H_0} \phi n_{A^-} dy$ (where $\sigma_{c,eq}$ is the equivalent surface charge density of the brush-free nanochannels and $\phi$ and $n_{A^-}$ are defined in chapter 2).

The diffusioosmotically-induced electric field is a combination of the osmotic ($\bar{E}_{osm}$) and the ionic ($\bar{E}_{ion}$) contributions (i.e., $\bar{E} = \bar{E}_{osm} + \bar{E}_{ion}$, see eqs. 23-28). The osmotic contribution to the electric field, $\bar{E}_{osm}$, is due to the downstream mi-

gration of the mobile ions of the electric double layer (EDL) in the presence of the diffusioosmotically induced velocity field. We shall later discuss in details the variation of this DOS velocity field. Fig. 4.3 compares $\bar{E}_{osm} - vs - c_\infty$ variation for the different cases for the brush-free and brush-grafted nanochannels. For the majority of the $c_\infty$ values, $\bar{E}_{osm}$ is larger for the brush-grafted nanochannel. There are two interrelated factors that ensure such enhanced $\bar{E}_{osm}$ for brush-grafted nanochannels. Firstly, for brush-grafted nanochannels, the DOS velocity field is significantly enhanced, as compared to that in the corresponding brush-free nanochannels across wide ranges of salt concentration and pH values (see Figs. 4.8-4.11 below). Only for a very few conditions this might not be true: e.g., for $c_\infty = 10^{-3}\ M$ for the case of $pH_\infty = 4,\ \ell = 60\ nm$ or for $c_\infty = 10^{-2}\ M$ for the case of $pH_\infty = 3,\ \ell = 10\ nm$. Secondly, the presence of the brushes localizes the net charge of the EDL away from the wall. The strength of a velocity field is much larger at locations away from the nanochannel wall. Accordingly, the contribution of the background flow that drives the EDL charges, thereby leading to the development of $\bar{E}_{osm}$, gets enhanced. These two effects interplay to dictate the final value of $\bar{E}_{osm}$. Accordingly, we mostly find $\left(\bar{E}_{osm}\right)_{Brush} > \left(\bar{E}_{osm}\right)_{No\ Brush}$ (see Fig. 4.3). However, this is not true for those particular cases where $(u_{DOS})_{Brush} < (u_{DOS})_{No\ Brush}$; this happens, for example, for $c_\infty = 10^{-3}\ M,\ pH_\infty = 4,\ \ell = 60\ nm$ and $c_\infty = 10^{-2}\ M,\ pH_\infty = 3,\ \ell = 10\ nm$. The contribution of the osmotic migration of the different ions ($\pm,\ H^+,\ OH^-$) to $\bar{E}_{osm}$ has been provided in Fig. 4.4 (also see eq. 4.10). The osmotic migration associated with the $H^+$ ions primarily contribute to $\bar{E}_{osm}$ for small salt concentrations. An increase in the salt concentration progressively increases the contribution associ-

ated with the osmotic migration of both salt cation and anion. These contributions negate each other. Such behaviors are true for both the brush-free and brush-grafted nanochannels. Under these circumstances, we eventually obtain a $\bar{E}_{osm}$ distribution that first increases and then decreases with $c_\infty$ for both the brush-grafted and brush-free nanochannels. In Fig. 4.4, we do not show the contribution associated with the osmotic migration of $OH^-$ ions as it is very small.

Here we first try to attempt to understand the significantly non-monotonic variation of $\bar{E}_{osm,i}$ with $c_\infty$. As evident from eq.(4.10), one can express:

$$\bar{E}_{osm,i} = \frac{Advection - based\ Electric\ Field}{Diffusion - based\ Electric\ Field} = \frac{2\bar{E}_{osm,i,adv}}{2\bar{E}_{osm,diff}}, \tag{4.15}$$

where

$$\bar{E}_{osm,i,adv} = Pe \int_{-1}^{0} \bar{u}\Big[ - \frac{z_i}{|z_i|}\bar{n}_{i,\infty} \exp(-\frac{z_i}{|z_i|}\bar{\psi})\Big] d\bar{y}, \tag{4.16}$$

and

$$\bar{E}_{osm,diff} = \int_{-1}^{0} \Big[R_+\bar{n}_{+,\infty} \exp(-\bar{\psi}) + R_-\bar{n}_{-,\infty} \exp(\bar{\psi}) + R_{H^+}\bar{n}_{H^+,\infty} \exp(-\bar{\psi}) + R_{OH^-}\bar{n}_{OH^-,\infty} \exp(\bar{\psi})\Big] d\bar{y}. \tag{4.17}$$

In Fig. 4.5, we plot the variation of $\bar{E}_{osm,diff}$ and $\bar{E}_{osm,i,adv}$ (for $i = \pm, H^+$) with $c_\infty$. Given that $\bar{E}_{osm,i}$ is simply the ratio of $\bar{E}_{osm,i,adv}$ and $\bar{E}_{osm,diff}$, all we have to do to shed light on the variation of $\bar{E}_{osm,i}$ with $c_\infty$ (see Fig. 4.4) is to better understand the corresponding variation of $\bar{E}_{osm,i,adv}$ and $\bar{E}_{osm,diff}$. It can be seen that $\bar{E}_{osm,diff}$ decreases monotonically with an increase in the salt concentration [see Fig. 4.5(a)]. In the lower salt concentration regime ($c_\infty \leq 10^{-pH_\infty}$), $\bar{E}_{osm,diff}$ primarily depends on the overall diffusion of the $H^+$ ions (dictated by the product of the dimensionless number density $\bar{n}_{H^+} = \frac{n_{H^+}}{n_\infty}$ and the dimensionless diffusivity

$R_{H^+}$), given that $H^+$ ions has significantly larger diffusivity among all the ions. Therefore, as the salt concentration increases, i.e., $n_\infty$ increases (in this weak salt concentration regime), a progressive lowering of the ratio $\bar{n}_{H^+} = \frac{n_{H^+}}{n_\infty}$ is encountered leading to a steep decrease in $\bar{E}_{osm,diff}$. This decrease is further augmented by the fact that the EDL potential decreases in magnitude monotonically with an increase in salt concentration [118] resulting in a smaller value of $n_{H^+}$. On the other hand, for much larger values of the salt concentration, i.e., when $c_\infty > 10^{-pH_\infty}$ and $|\bar{\psi}| \ll 1$ [118], we can simplify $\bar{E}_{osm,diff}$ as (with $\bar{n}_{+,\infty} = n_\infty/n_\infty = 1$, $\bar{n}_{-,\infty} = (n_\infty + n_{H^+,\infty})/n_\infty = 1 + \bar{n}_{H^+,\infty}$, neglecting $\bar{n}_{OH^-,\infty}$, and $\exp(\pm\bar{\psi}) \approx 1 \pm \bar{\psi} \approx 1$):

$$\begin{aligned}\bar{E}_{osm,diff} &\approx \int_{-1}^{0} \Big[R_+ + R_- \left(1 + \bar{n}_{H^+,\infty}\right) + R_{H^+}\bar{n}_{H^+,\infty} + R_{OH^-}\bar{n}_{OH^-,\infty}\Big] d\bar{y} \\ &= \Big[R_+ + R_- \left(1 + \bar{n}_{H^+,\infty}\right) + R_{H^+}\bar{n}_{H^+,\infty} + R_{OH^-}\bar{n}_{OH^-,\infty}\Big] \approx (R_+ + R_-) \quad (4.18)\end{aligned}$$

Therefore, for such larger values of $c_\infty$, we observe that $\bar{E}_{osm,diff}$ becomes constant and does not vary with $c_\infty$. On increasing $pH_\infty$, when all other parameters are kept constant, $\bar{E}_{osm,diff}$ decreases owing to the decrease in the bulk hydrogen ion number density. On the other hand, an increase in the grafting density (decreasing $\ell$) leads to an increased magnitude of the EDL potential due to larger overall charge of the PE brush. This in turn increases $\bar{n}_{H^+}$, which has the highest diffusivity among all the given ions, which enhances the $\bar{E}_{osm,diff}$.

We next study the variation of the advection-based field $\bar{E}_{osm,+,adv}$ [see Fig. 4.5(b)]. From eq.(4.16), we find that $\bar{E}_{osm,+,adv}$ depends on the Peclet number (Pe) (or characteristic velocity U), EDL potential, and the fluid velocity (with $\bar{n}_{+,\infty} = n_\infty/n_\infty = 1$). Using the definitions of $Pe$ [see below eq.(4.16)] and $U$

[see below eq.(4.14)] as well as the condition $dn_\infty/dx = 10^4 n_\infty$, we can express, $Pe \propto \frac{1}{1+\bar{n}_{H^+,\infty}}$. Therefore, for small $c_\infty$ (i.e., $c_\infty \ll 10^{-pH_\infty}$), $Pe \propto n_\infty/n_{H^+,\infty}$, implying that $Pe$ increases linearly with $n_\infty$. On the other hand, for much larger $c_\infty$ (i.e., $c_\infty \gg 10^{-pH_\infty}$), $Pe \approx \frac{10^4 \epsilon_0 \epsilon_r (k_B T)^2 L}{\eta e^2 (D_+ + D_- + D_{H^+} + D_{OH^-})}$, i.e., $Pe$ does not vary with salt concentration. Accordingly, for smaller salt concentrations, variation of $\bar{E}_{osm,+,adv}$ with $c_\infty$ is mostly dictated by the corresponding variation of $Pe$ (which varies linearly with $c_\infty$ for such small concentration values, see above), while for larger salt concentration, where $Pe$ no longer varies with $c_\infty$ (see above), variation of $\bar{E}_{osm,+,adv}$ with $c_\infty$ is mostly dictated by the corresponding variation of the dimensionless diffusioosmotic velocity profile $\bar{u}$. Of course, $|\bar{\psi}|$ monotonically decreases with $c_\infty$ [118] and that also contributes to the overall variation of $\bar{E}_{osm,+,adv}$ with $c_\infty$. Under such circumstances, for the case $pH_\infty = 4$ and $\ell = 60\ nm$, $\bar{E}_{osm,+,adv}$ increases mononotonically with $c_\infty$ for smaller $c_\infty$ values reflecting the dominant influence of $Pe$. At larger concentrations ($c_\infty > 10^{-pH_\infty}$), i.e., when the effect of $\bar{u}$ starts to dominate the variation of $\bar{E}_{osm,+}, adv$, we see a very large decrease in velocity [see Fig. 4.8(c)] as we move from $c_\infty$ of $10^{-4}M$ to $10^{-3}M$ (for the case of $pH_\infty = 4$ and $\ell = 60\ nm$) which is reflected by a steep decrease in $\bar{E}_{osm,+}, adv$. As we further move from $c_\infty$ of $10^{-3}M$ to $10^{-2}M$, it can be seen that there is an increase in $\bar{E}_{osm,+}, adv$ due to similar increase in $\bar{u}$. Finally, moving from $c_\infty$ of $10^{-2}M$ to $10^{-1}M$ the velocity decreases slightly, which is reflected by a slight decrease in $\bar{E}_{osm,+,adv}$. On the other hand, if we consider the case of $pH_\infty = 3$ and $\ell = 10\ nm$, we find this monotonic increase of $\bar{E}_{osm,+,adv}$ with $c_\infty$ (due to the corresponding increase of $Pe$ with $c_\infty$) for upto $c_\infty = 10^{-3}\ M$; subsequently, there is a steep decrease in $\bar{E}_{osm,+,adv}$ with

$c_\infty$ as we move from $c_\infty$ of $10^{-3}M$ to $10^{-2}M$ [due to a significantly smaller $\bar{u}$ at $c_\infty = 10^{-2}$ $M$, see Fig. 4.8(b)]; $\bar{E}_{osm,+,adv}$ increases with $c_\infty$ as we move from $c_\infty$ of $10^{-2}M$ to $10^{-1}M$ due to the corresponding enhanced value of $\bar{u}$ [see Fig. 4.8(b)]. Finally, for the case of $pH_\infty = 3$ and $\ell = 60$ $nm$, we do find a monotonic increase in $\bar{E}_{osm,+,adv}$ with $c_\infty$ for smaller $c_\infty$ values; however, no drastic variation in the corresponding $\bar{u}$ profile (as witnessed for cases of $pH_\infty = 4$ and $\ell = 60$ $nm$ and $pH_\infty = 3$ and $\ell = 10$ $nm$) implies that for larger salt concentrations (i.e., where $Pe$ does not vary with $c_\infty$), $\bar{E}_{osm,+,adv}$ does not show significant variation with $c_\infty$ except for a slight decrease in the range from $c_\infty = 10^{-2} - 10^{-1}$ $M$ (due to a noticeable lowering of $\bar{u}$ [see Fig. 4.8(a)]). We can use these information on $\bar{E}_{osm,diff}$ [see Fig. 4.5(a)] and $\bar{E}_{osm,+,adv}$ [see Fig. 4.5(b)] for interpreting the variation of $\bar{E}_{osm,+}$ for the three different cases. For example using these variations, we can straightaway explain the steep increases in $\bar{E}_{osm,+}$ for majority of salt concentration and small decrease in the range from $c_\infty = 10^{-2} - 10^{-1}$ $M$ for the case of $pH_\infty = 3$ and $\ell = 60$ $nm$ [see Fig. 4.4(a)]. Similarly, for the case of $pH_\infty = 3$ and $\ell = 10$ $nm$, we can easily justify an increase, then a decrease (in the range from $c_\infty = 10^{-3} - 10^{-2}$ $M$), and then again an increase (for $c_\infty \geq 10^{-2}$ $M$) in $\bar{E}_{osm,+}$ from the corresponding variation of $\bar{E}_{osm,+,adv}$ and $\bar{E}_{osm,diff}$ [see Fig. 4.4(b)]. Finally, for the case of $pH_\infty = 4$ and $\ell = 60$ $nm$, this studied variation for $\bar{E}_{osm,+,adv}$ and $\bar{E}_{osm,diff}$ helps to justify $\bar{E}_{osm,+}$ first increasing, then decreasing (in the range from $c_\infty = 10^{-4} - 10^{-3}$ $M$), again increasing (in the range from $c_\infty = 10^{-3} - 10^{-2}$ $M$), and then finally again decreasing (in the range from $c_\infty = 10^{-2} - 10^{-1}$ $M$) with $c_\infty$ [see Fig. 4.4(c)]. We next study the variation of $\bar{E}_{osm,-,adv}$ with $c_\infty$ [see Fig. 4.5(c)].

Given the negative valence of the anion, $\bar{E}_{osm,-,adv}$ is primarily negative. For this case, $Pe \times \bar{n}_{-,\infty} \propto \frac{n_\infty}{n_\infty + n_{H^+,\infty}} \times \frac{n_\infty + n_{H^+,\infty}}{n_\infty} \propto 1$ (neglecting $n_{OH^-,\infty}$). Therefore, $Pe$ has no role to play in the variation of $\bar{E}_{osm,-,adv}$. Accordingly, for smaller $c_\infty$ values $\bar{E}_{osm,-,adv}$ remains constant as $c_\infty$ varies. On the other hand, the strong dependence of $\bar{E}_{osm,-,adv}$ on the velocity profile ($\bar{u}$) starts to get manifested for larger values of $c_\infty$ (since for such $c_\infty$ values, there are distinct changes in $\bar{u}$, see Fig. 4.8). For the case of $pH_\infty = 4$ and $\ell = 60\ nm$, $\bar{u}$ significantly decreases, increases, and decreases for the concentration ranges of $c_\infty = 10^{-4} - 10^{-3}\ M$, $c_\infty = 10^{-3} - 10^{-2}\ M$, and $c_\infty = 10^{-2} - 10^{-1}\ M$ [see Fig. 4.8(c)]; accordingly for the exact same respective concentration ranges, $\bar{E}_{osm,-,adv}$ decreases, increases, and decreases. On the other hand, for $pH_\infty = 3$ and $\ell = 10\ nm$, $\bar{u}$ significantly decreases and increases for the concentration ranges of $c_\infty = 10^{-3} - 10^{-2}\ M$ and $c_\infty = 10^{-2} - 10^{-1}\ M$, respectively [see Fig. 4.8(b)]; accordingly for the exact same respective concentration ranges, $\bar{E}_{osm,-,adv}$ decreases and increases. Finally, for the case of $pH_\infty = 3$ and $\ell = 60\ nm$, there is no such distinctly large increase or decrease of $\bar{u}$ for any concentration range, except for a noticeable decrease in $\bar{u}$ for $c_\infty = 0.1\ M$ [see Fig. 4.8(a)]; accordingly, $\bar{E}_{osm,-,adv}$ remains more or less constant for the entire concentration range, except for a slight decrease for the concentration range of $c_\infty = 10^{-2} - 10^{-1}\ M$. From this variation of $\bar{E}_{osm,-,adv}$ and the variation of $\bar{E}_{osm,diff}$ [see Fig. 4.5(a)], we can explain the corresponding non-monotonic variation of $\bar{E}_{osm,-}$ in Fig. 4.4: for $pH_\infty = 3$ and $\ell = 60\ nm$, $\bar{E}_{osm,-}$ monotonically increases with $c_\infty$ and only decreases slightly for concentration range of $c_\infty = 10^{-2} - 10^{-1}\ M$ [see Fig. 4.4(a)]; for $pH_\infty = 3$ and $\ell = 10\ nm$, $\bar{E}_{osm,-}$ varies monotonically with $c_\infty$ upto $c_\infty = 10^{-3}\ M$ and subse-

quently decreases and increases for the concentration ranges of $c_\infty = 10^{-3} - 10^{-2}\ M$ and $c_\infty = 10^{-2} - 10^{-1}\ M$, respectively [see Fig. 4.4(b)]; for $pH_\infty = 4$ and $\ell = 60\ nm$, $\bar{E}_{osm,-}$ varies monotonically with $c_\infty$ upto $c_\infty = 10^{-4}\ M$ and subsequently decreases, increases, and decreases for the concentration ranges of $c_\infty = 10^{-4} - 10^{-3}\ M$, $c_\infty = 10^{-3} - 10^{-2}\ M$, and $c_\infty = 10^{-2} - 10^{-1}\ M$, respectively [see Fig. 4.4(c)].

We finally study the variation of $\bar{E}_{osm,H^+,adv}$ with $c_\infty$ [see Fig. 4.5(d)]. For this case, $Pe \times \bar{n}_{H^+,\infty} \propto \frac{n_\infty}{n_\infty + n_{H^+,\infty}} \times \frac{n_{H^+,\infty}}{n_\infty} \propto \frac{1}{1+\frac{n_\infty}{n_{H^+,\infty}}}$. Therefore, an increase in $c_\infty$ (or $n_\infty$) for a given $pH_\infty$ (or $n_{H^+,\infty}$) will lead to a progressive decrease in $\bar{E}_{osm,H^+,adv}$, as evident from Fig. 4.5(d). For very small $c_\infty$, the ratio $\frac{n_\infty}{n_{H^+,\infty}}$ is relatively small implying a weak lowering of $\bar{E}_{osm,H^+,adv}$ with $c_\infty$. However, as $c_\infty$ increases this ratio increases making the reduction of $\bar{E}_{osm,H^+,adv}$ more prominent. Of course, for larger $pH_\infty$ (or smaller $n_{H^+,\infty}$), the ratio becomes larger for smaller $c_\infty$ values leading to a much steeper lowering of $\bar{E}_{osm,H^+,adv}$ starting from a much smaller $c_\infty$ value. Of course, the changes in $\bar{u}$ also contribute to this variation, but gets overwhelmed by the effect of the ratio $\frac{n_\infty}{n_{H^+,\infty}}$ at larger $c_\infty$ values. This particular nature of variation of $\bar{E}_{osm,H^+,adv}$ and the corresponding variation of $\bar{E}_{osm,diff}$ [see Fig. 4.5(a)] helps to explain the corresponding variation of $\bar{E}_{osm,H^+}$ in Fig. 4.4: for all combinations of $pH_\infty$ and $\ell$ values, we thus find a monotonic increase of $\bar{E}_{osm,H^+}$ with $c_\infty$ for smaller $c_\infty$ values (for such cases the decrease in $\bar{E}_{osm,H^+,adv}$ with $c_\infty$ is relatively weaker than the corresponding decrease of $\bar{E}_{osm,diff}$ with $c_\infty$) and a monotonic decrease of $\bar{E}_{osm,H^+}$ with $c_\infty$ for larger $c_\infty$ values (for such cases of larger concentration values, the decrease in $\bar{E}_{osm,H^+,adv}$ with $c_\infty$ governs the variation of $\bar{E}_{osm,H^+}$ since $\bar{E}_{osm,diff}$ is nearly constant with $c_\infty$).

$\bar{E}_{osm}$ plotted in Fig. 4.3 for the different combinations of $pH_\infty$ and $\ell$ is simply the sum of different $\bar{E}_{osm,i}$. The particular variation of $E_{osm,i}$, as described in Fig. 4.4 and explained in great details through Fig. 4.5, leads to this highly non-monotonic variation of $\bar{E}_{osm}$ with $c_\infty$ for the different combinations of $pH_\infty$ and $\ell$, as depicted in Fig. 4.3.

In Fig. 4.6, we plot the variation of the $\bar{E}_{ion}$ with $c_\infty$, representing the dimensionless conduction component of the electric field. This is equivalent to the electric field that is generated by the conduction of the mobile EDL ions. Therefore, $\bar{E}_{ion}$ depends on the mobility (or the diffusivity) of the ions and the applied ion concentration gradient. In other words, this conduction component of the electric field results from the interplay of this imposed concentration gradient on the EDL counterions and coions that varies both in diffusivity as well as the number density. Given that the total surface charge density of the brushes is identical to that of the bare nanochannels, the quantity $\int_{-h}^{h}(n_+ - n_-)dy$ should be identical for both the brush-grafted and brush-free nanochannels. However, the ionic diffusivities are different (i.e., $R_+ \neq R_-$). Furthermore, the individual ion number densities for the brush-free and brush-grafted nanochannels are different, i.e., $\left[n_\pm(y)\right]_{Brush} \neq \left[n_\pm(y)\right]_{No\ Brush}$ since the local EDL electrostatic potentials are different for the brush-free and brush-grafted systems. Under such conditions, $\bar{E}_{p,ion}$ (i.e., the contribution of the salt cation on the overall ionic current) and $\bar{E}_{m,ion}$ (i.e., the contribution of the salt anion on the overall ionic current), with $\bar{E}_{ion} = \bar{E}_{p,ion} - \bar{E}_{m,ion}$ (see eqs. 26,27 for the definition of $\bar{E}_{p,ion}$ and $\bar{E}_{m,ion}$), are different between the brush-free and brush-grafted nanochannels (see Fig. 4.6). This difference manifests as

$(\bar{E}_{p,ion})_{No\ Brush} < (\bar{E}_{p,ion})_{Brush}$ and $(\bar{E}_{m,ion})_{No\ Brush} > (\bar{E}_{m,ion})_{Brush}$ for all combinations of grafting density, salt concentrations, and pH. Given that the current due to the migration of the salt anions decreases the overall ionic current, it eventually ensures that $(\bar{E}_{ion})_{Brush} > (\bar{E}_{ion})_{No\ Brush}$ for cases where $E_{ion}$ is positive. Interestingly, unlike $\bar{E}_{osm}$, which is always positive, given the fact that the velocity field, which is driving it is mostly negative causing an accumulation of positive counterions on the left of the nanochannel, $\bar{E}_{ion}$ can becomes negative at different $c_\infty$ ranges depending on the grafting density and pH for both brush-grafted and brush-free nanochannels. Such negative values of $\bar{E}_{ion}$ is encountered when $\bar{E}_{m,ion} > \bar{E}_{p,ion}$ – for such cases, $|(\bar{E}_{ion})_{Brush}| < |(\bar{E}_{ion})_{No\ Brush}|$.

In the inset of each of the subfigures of Fig. 4.7, we separately plot the variation of $\bar{E}_{p,ion,N} = \bar{n}_1' \int_{-1}^{0} \left[R_+ \exp(-\bar{\psi})\right] d\bar{y}$ and $\bar{E}_{m,ion,N} = \bar{n}_1' \int_{-1}^{0} \left[R_- \exp(\bar{\psi})\right] d\bar{y}$. For very weak salt concentration, the EDL thickness is large causing a large EDL overlap. Accordingly, $\psi$ remains uniform. This is manifested as constant value of $\bar{E}_{m,ion,N}$ [that varies linearly with $\exp(\psi)$] and $\bar{E}_{p,ion,N}$ [that varies linearly with $\exp(-\psi)$]. However, a progressive increase in the salt concentration significantly reduces the negative magnitude of $\psi$, which enhances $\exp(\psi)$ and reduces $\exp(-\psi)$. Accordingly, $\bar{E}_{p,ion,N}$ and $\bar{E}_{m,ion,N}$ decreases and increases, respectively.

Such a combination of $\bar{E}_{osm}$ and $\bar{E}_{ion}$ eventually dictates the overall diffusioosmotically induced electric field (see Fig. 4.2). It clearly establishes that for all combinations of $c_\infty$, $\ell$ (quantifying the grafting density), and $pH_\infty$, the electric field induced inside the brush-grafted nanochannels is larger than that inside the brush-free nanochannels. Accordingly, for conditions where the electric field is

positive, $\bar{E}_{Brush} > \bar{E}_{No\ Brush}$ and for conditions where the electric field is negative, $|\bar{E}_{Brush}| < |\bar{E}_{No\ Brush}|$. As has been described above, at different $c_\infty$, $\ell$, $pH_\infty$ values $\bar{E}_{osm}$ and $\bar{E}_{ion}$ contribute differently to ensure this enhancement.

### *4.3.2 Variation of the diffusioosmotically-induced velocity field*

Fig. 4.8 provides the variation of the DOS velocity field in brush-grafted and brush-free nanochannels. The DOS velocity has two contributions: the chemiosmotic (COS) component that is caused by the induced pressure gradient due to the applied salt concentration gradient and the electroosmotic (EOS) component that is triggered by the diffusioosmotically induced electric field. To better understand the impact of these components (COS and EOS) in governing the overall DOS velocity, in Figs. 9-11, we compare the variation of the DOS velocity field (denoted as $u_{total}$) and the COS velocity field (denoted as $u_{COS}$). $u_{COS}$ is obtained by switching off the effect of the induced electric field in the Stokes equation, i.e., by solving the equation:

$$\frac{\partial^2 \bar{u}}{\partial \bar{y}^2} = A\bar{n}_1'(cosh(\bar{\psi}) - 1) + \frac{h^2}{\kappa_d}\bar{u} \quad (-1 \leq \bar{y} \leq -1 + \bar{H}_0),$$
$$\frac{\partial^2 \bar{u}}{\partial \bar{y}^2} = A\bar{n}_1'(cosh(\bar{\psi}) - 1) \quad (-1 + \bar{H}_0 \leq \bar{y} \leq 0). \tag{4.19}$$

$$\frac{\partial^2 \bar{u}}{\partial \bar{y}^2} = A\bar{n}_1'(cosh(\bar{\psi}) - 1) \quad (-1 \leq \bar{y} \leq 0). \tag{4.20}$$

Eqs.(4.19),(4.20) represent the equations for obtaining the dimensionless COS velocity fields in brush-grafted and brush-free nanochannels, respectively. Figs. 4.9-4.11 provide the variation of $u_{total}$ and $u_{COS}$ for brush-free and brush-grafted nanochannels for different combinations of $c_\infty$, $\ell$, and $pH_\infty$. For a positive value of the salt

concentration gradient, as is the condition for the present case, the pressure gradient is positive enforcing a right-to-left pressure-driven or COS flow field. This is true for both the cases of brush-free and brush-grafted nanochannels for all the different parameter choices (see Figs. 4.9-4.11). On the other hand, the direction of the EOS transport, and accordingly whether it aids or reduces the contribution of the COS transport, is determined by the sign of the induced DOS electric field (see Fig. 4.2). A positive (negative) electric field triggers an EOS component from left-to-right (right-to-left), thereby opposing (augmenting) the effect of the COS transport. For both the brush-grafted and brush-free nanochannels, the induced electric field is negative for $c_\infty = 0.1\ M$ for $pH_\infty = 3,\ \ell = 10\ nm$, for $c_\infty = 0.01, 0.1\ M$ for $pH_\infty = 4,\ \ell = 60\ nm$, and for all $c_\infty$ values for $pH_\infty = 3,\ \ell = 60\ nm$ (see Fig. 4.2). Therefore, for all these cases, the EOS component aids the COS component to enhance the overall DOS transport (see Figs. 4.9-4.11). On the other hand, for other values of $c_\infty$, the induced DOS electric field is positive and hence the corresponding EOS component is opposite in direction to the COS component ensuring a reduction in the DOS transport (see Figs. 4.9-4.11). The most interesting facet is that despite the fact that the electric field is comparable for the brush-grafted and brush-free nanochannels, the contribution of the corresponding EOS transport in either aiding or opposing the COS transport is much larger for the case of the brush grafted nanochannels. This stems from our previously hypothesized brush-induced localization of the EDL charge density away from the nanochannel walls enforcing a much larger impact of the EOS body force of similar strengths [30–32].

The above-described interplay of the effects of different factors eventually dic-

tates the overall DOS velocity in the brush-free and brush-grafted nanochannels (see Fig. 4.8): depending on whether the EOS transport augments or opposes the COS velocity component, the extent of this augmentation/opposition, and the enhanced effect of the EOS body force due to the localization effect of the brushes, the DOS flow strength might be enhanced or weakened inside the brush-grafted nanochannels as compared to the brush-free nanochannels. For the parameter space studied here, except for a few cases, we find that the DOS flow strength is always larger in the brush-grafted nanochannels.

### *4.3.3 Comparsion of the DOS transport in two types of Brush-grafted Nanochannels: Backbone-charged Brushes (present study) versus End-Charged Brushes*

In a recent study [31], we had probed the DOS transport in nanochannels grafted with end-charged PE brushes. It is worthwhile to compare the findings of the present study (DOS transport in nanochannels grafted with backbone-charged PE brushes) with findings of this previous study. First and foremost it is critical to point out that in this previous study [31], the brushes were described using the simplistic Alexander-de-Gennes model that considered a uniform density of the monomers along the length of the brushes. On the other hand, in the present study, we apply a much more rigorous augmented SST model, which accounts for the more appropriate distribution of the monomers (larger concentration at near-wall locations as compared to that away from the wall) along the length of the PE brushes.

In Fig. 4.12, we compare the variation of the diffusioosmotically induced electric field for these two different cases: nanochannels grafted with end-charged and backbone charged PE brushes. For ensuring that we are considering identical charge content of the PE brushes for the two cases, the charge density for the end-charged PE brushes is considered to be $\sigma_{c,eq}$ (please see section 4.3.1 for the definition of $\sigma_{c,eq}$). The comparison reveals that most strikingly, for the present case, the electric field varies non-monotonically with the salt concentration, while for the case of nanochannel with end-charged brushes, the electric field decreases monotonically with the salt concentration. This stems for the non-monotonic variation of the $\bar{E}_{osm}$ and $\bar{E}_{ion}$ for the present case (please see Figs. 4.3 and 4.6). The difference in the EDL distribution, dictated by the fact that for the previous study [31] the EDL is localized at the non-grafted brush-tip while for the present case it is distributed along the brush length (as the charged monomers are distributed along the brush length) led to a specific variation of $\bar{E}_{p,ion}$ and $\bar{E}_{m,ion}$ that caused this non-monotonic variation of $\bar{E}_{ion}$ with $c_\infty$ for the present case (please see Fig. 4.6). Additionally, for the present case, there is the non-monotonic variation in $\bar{E}_{osm}$ with $c_\infty$ (please see Fig. 4.3), which is large due to the osmotic contribution of the $H^+$ ions (see Fig. 4.4 and the related discussions). On the other hand, our previous study [31] did not consider the effect of pH (or the migration of $H^+$ ions in dictating the corresponding osmotic component of the diffusioosmotically electric field).

In Fig. 4.13, we compare the DOS velocity field for these two different cases: nanochannels grafted with end-charged and backbone charged PE brushes. This velocity comparison is the key contribution of this subsection, given that we pro-

pose this new design (backbone-charged PE brush grafted nanochannel) to enhance the DOS nanofluidic transport. The central idea is as follows. Firstly, for both the present study and the previous study [31], the body forces (induced EOS body force resulting from the induced electric field and the induced COS body force resulting from the induced pressure-gradient) are localized away from the nanochannel wall (i.e., the location of the maximum wall-induced drag force). This leads to an augmented manifestation of both of these driving forces. Secondly, the previous study considered a uniform monomer distribution along the length of the brush, while the present study considers a more realistic monomer distribution where the monomer concentration is larger concentration at near-wall locations and smaller at locations away from the wall. Therefore, the monomer concentration is much larger (smaller) at the location where the different body forces are localized for the previous (present) study. Given that the drag coefficient varies quadratically with the monomer concentration, such a scenario implies that the PE-brush-induced drag force is much larger (smaller) at the location where the different body forces (COS and EOS) are localized for the previous (present) study. As a consequence, the impact of both the COS and EOS body forces in triggering the corresponding COS and EOS flow components is much smaller (larger) for the previous (present) study. Therefore, for most of the combinations of $c_\infty$ and charge density values, the magnitude of the DOS velocity for the present case (either from left-to-right or right-to-left, depending on the relative direction and strength of the EOS transport with respect to the COS transport) is mostly larger than that for the previous study. This analysis provided in Fig. 4.13, firmly establishes the novelty of the present study over and above that

of our previous study [31] in terms of significantly enhancing the DOS transport in functionalized nanochannels.

## *4.4 Conclusions*

In this paper, we develop a theoretical model to quantify the DOS transport in nanochannels grafted with PE brushes modelled using our recently developed augmented SST. The diffusioosmotically induced electric field and water flow characterize this DOS transport, which is generated in the presence of an axially employed salt concentration gradient. The presence of the brushes leads to an enhanced induced electric field for positive values of the electric field. The presence of the brushes further ensure a larger DOS flow velocity, as compared to the cases of brush-free nanochannels or nanochannels grafted with end-charged brushes for a major combination of salt concentration, pH, and grafting density values. With respect to the brush-free nanochannels, such an enhancement is contributed by the brush-induced localization of the EDL charge density away from the nanochannel walls (or *wall-induced drag force*), which in turn leads a much more enhanced effect of the induced EOS body force caused by the diffusioosmotically induced electric field. On the other hand, with respect to the nanochannel grafted with end-charged brushes, such an enhancement is due to the localization of the *brush-induced drag force* away from the location of where the EDL-induced EOS and COS body forces are localized.

## *4.5 Appendix*

### *Simplification of the y-momentum equation to obtain the starting point of eq.(4.1)*

The present study considers a long nanochannel, such that $L \gg h$. Under such conditions, one can apply the *Space Charge Theory or SCT* (see [183] for details) for describing the EDL electrostatic potential, ion number densities, the fluxes and the local flow fields. The critical issue of the SCT is that for this very long and thin nanochannel, one must have local equilibrium in the transverse direction. The condition of this local transverse equilibrium leads to $v(x, y) = 0$, where $v$ is the transverse velocity field (velocity field in y-direction). We have previously shown (for the case of diffusioosmotic transport in *brush-free* nanochannels), that our problem statement, where we employ a very weak salt concentration gradient along the length of a nanochannel (where $L \gg h$), leads to the case where one can directly apply the SCT (please see the detailed Supplementary Material of Ref. [187]). The present problem is the same as that of the previous study, except that we now have the presence of grafted backbone-charged PE brushes. Therefore, for the present case too, we can consider the existence of local equilibrium in the transverse direction, which in turn will lead to $v(x, y) = 0$.

On the other hand, the Navier Stokes y-momentum equation (in the absence of the effect of the gravitational body force, since we consider very small mass of liquid

confined in a nanochannel) can be expressed as:

$$\rho\left(\frac{\partial v}{\partial t}+u\frac{\partial v}{\partial x}+v\frac{\partial v}{\partial y}\right)=-\frac{\partial p}{\partial y}-e\left(n_{+}-n_{-}+n_{H^{+}}-n_{OH^{-}}\right)\frac{\partial \psi}{\partial y}. \tag{4.21}$$

In the above equation, the last term on the right hand side represents the body force in y-direction resulting from the interaction of the net EDL charge density $[e\left(n_{+}-n_{-}+n_{H^{+}}-n_{OH^{-}}\right)]$ and the EDL transverse electric field $(-\frac{\partial \psi}{\partial y})$. Using the condition of $v(x,y)=0$ in the above equation leads to:

$$\frac{\partial p}{\partial y}+e\left(n_{+}-n_{-}+n_{H^{+}}-n_{OH^{-}}\right)\frac{\partial \psi}{\partial y}=0, \tag{4.22}$$

which is the starting point of eq.(4.1)

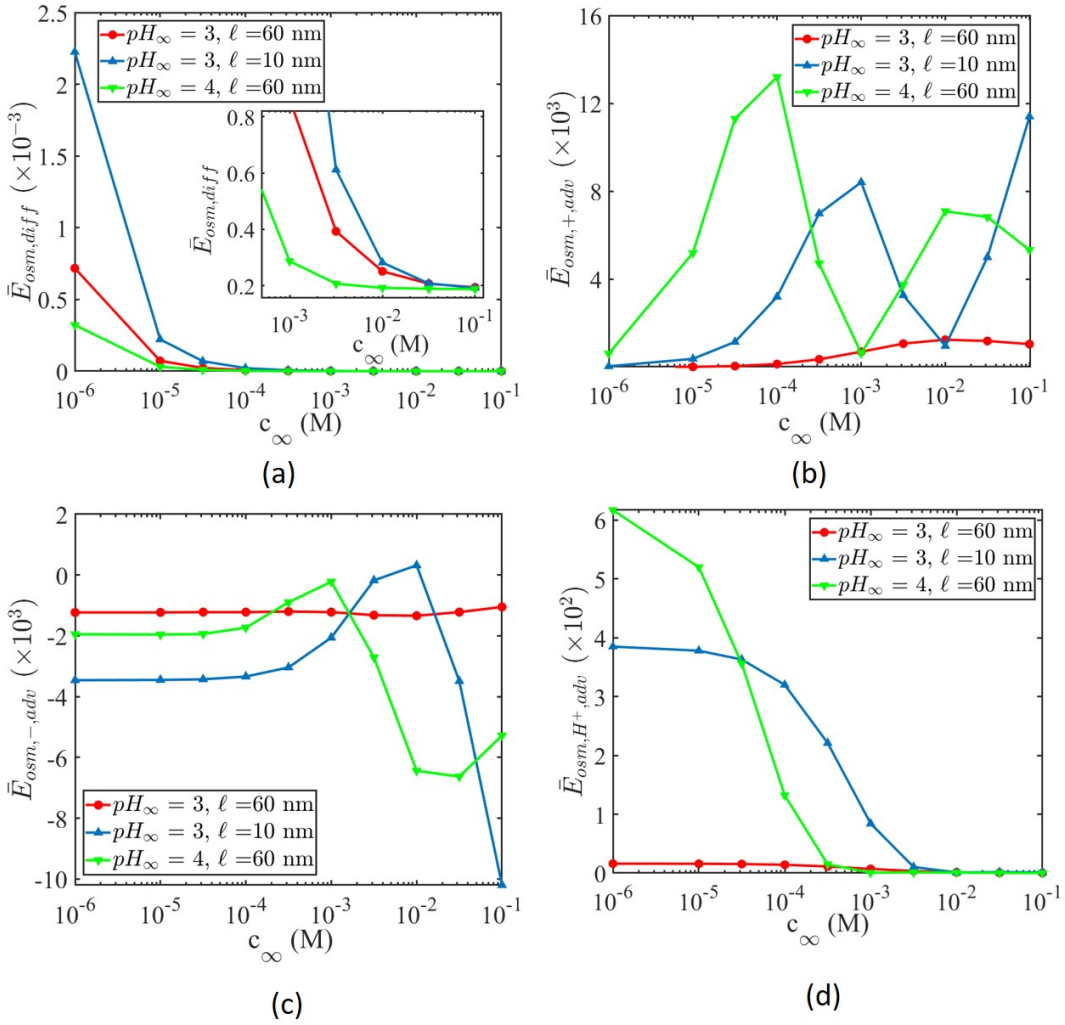


*Fig. 4.5:* Variation of the different components [namely, $\bar{E}_{osm,diff}$ (see (a)) and $\bar{E}_{osm,i,adv}$ (see (b-d))] that constitute $\bar{E}_{osm,i}$ [see eqs.(30-32)] with $c_\infty$. Results are only shown for the brush-grafted nanochannels for different combinations of $pH_\infty$ and $\ell$. Other parameters are identical to those used in Fig. 4.2. Here we do not show $\bar{E}_{osm,OH^-,adv}$ (i.e., the contribution associated with the $OH^-$ ions) as it is very small.

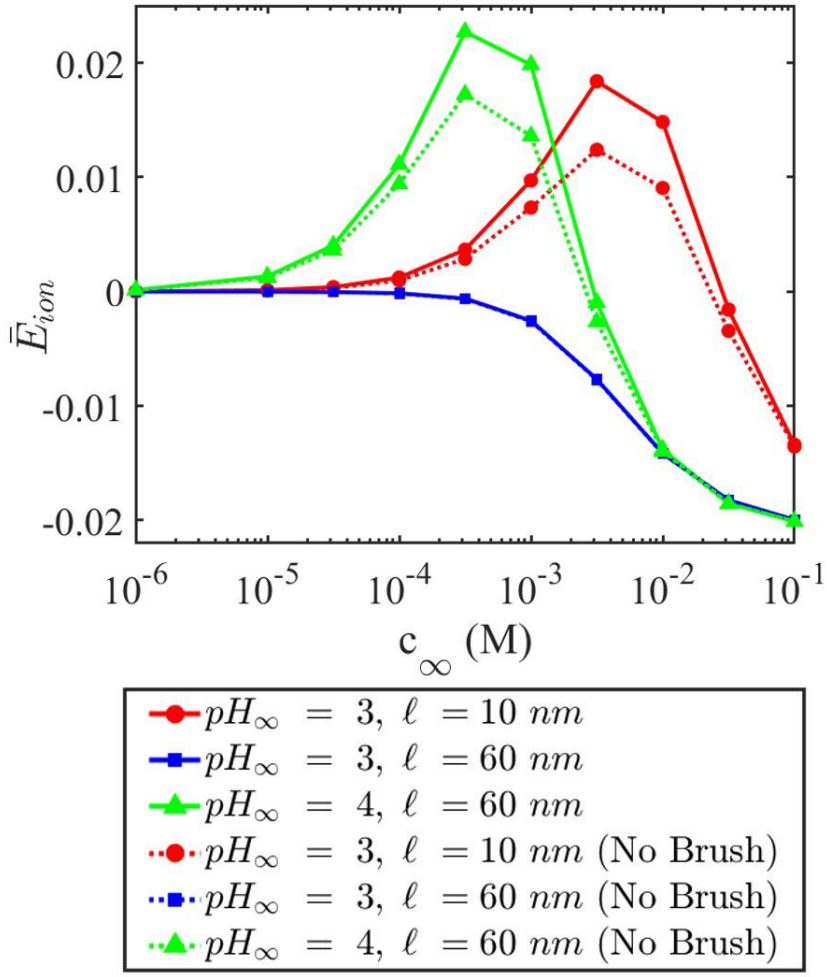


*Fig. 4.6:* Variation of the dimensionless ionic ($\bar{E}_{ion}$) component of the diffusioosmotically-induced electric field with $c_\infty$ in presence of an applied salt number density gradient of $\nabla n_\infty = dn_\infty/dx = 10^4 n_\infty$. for both brush-grafted and brush-free nanochannels for different combinations of $\ell$ and $pH_\infty$ values. Other parameters are identical to those used in Fig. 4.2.

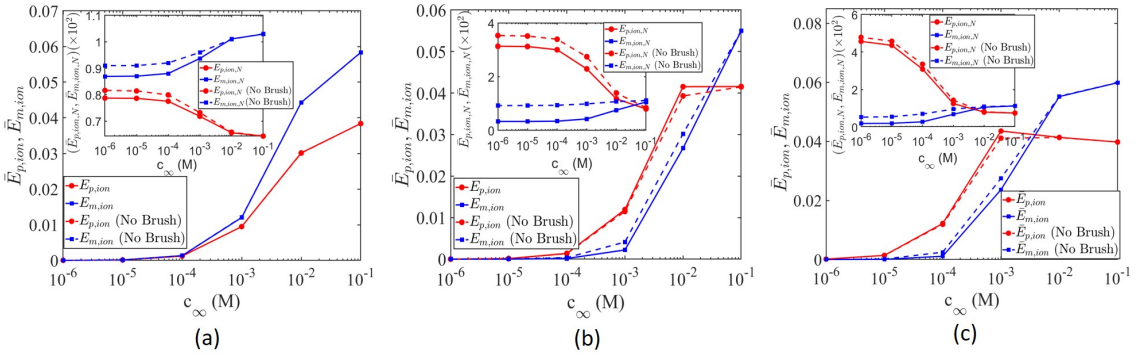


*Fig. 4.7:* Variation of $\bar{E}_{p,ion}$ and $\bar{E}_{m,ion}$ (see the text and eqs. 26,27 for their definitions) components of $\bar{E}_{ion}$ with $c_\infty$ in presence of an applied salt number density gradient of $\nabla n_\infty = dn_\infty/dx = 10^4 n_\infty$ for both brush-grafted and brush-free nanochannels for (a) $pH_\infty = 3,\ \ell = 60\ nm$, (b) $pH_\infty = 3,\ \ell = 10\ nm$, and (c) $pH_\infty = 4,\ \ell = 60\ nm$. In the insets of each figures, the corresponding variations of $\bar{E}_{p,ion,N}$ and $\bar{E}_{m,ion,N}$ (see the text for the definition of these quantities) with $c_\infty$ have been shown. Other parameters are identical to those used in Fig. 4.2.

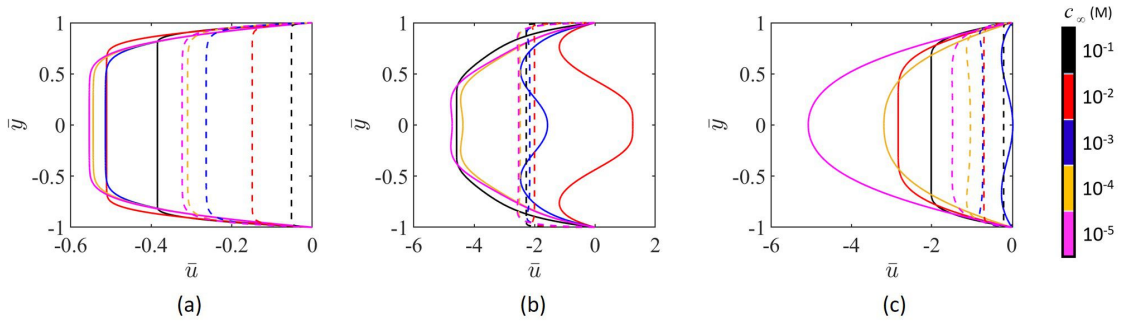


*Fig. 4.8:* DOS velocity field profiles in presence of an applied salt number density gradient of $\nabla n_\infty = dn_\infty/dx = 10^4 n_\infty$. for both brush-grafted (shown by solid lines) and brush-free (shown by dashed lines) nanochannels for different $c_\infty$ for (a) $pH_\infty = 3,\ \ell = 60\ nm$, (b) $pH_\infty = 3,\ \ell = 10\ nm$, and (c) $pH_\infty = 4,\ \ell = 60\ nm$. Other parameters are identical to those used in Fig. 4.2.

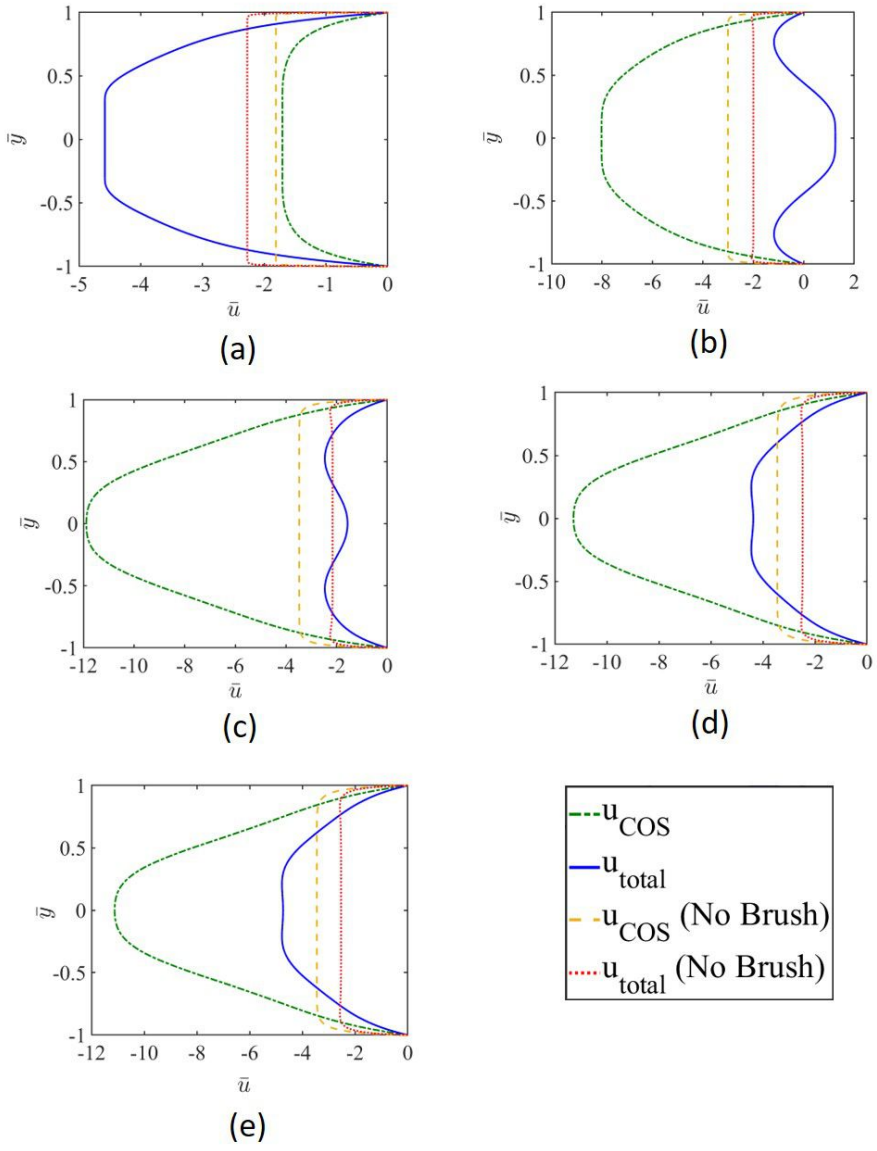


*Fig. 4.9:* DOS velocity field profiles (denoted as $u_{tot}$) and COS velocity profiles [obtained by solving eqs.(4.19) and (4.20)] in presence of an applied salt number density gradient of $\nabla n_\infty = dn_\infty/dx = 10^4 n_\infty$. for both brush-grafted and brush-free nanochannels for $pH_\infty = 3$, $\ell = 10\ nm$ for (a) $c_\infty = 10^{-1}\ M$, (b) $c_\infty = 10^{-2}\ M$, (c) $c_\infty = 10^{-3}\ M$, (d) $c_\infty = 10^{-4}\ M$, and (e) $c_\infty = 10^{-5}\ M$. Other parameters are identical to those used in Fig. 4.2.

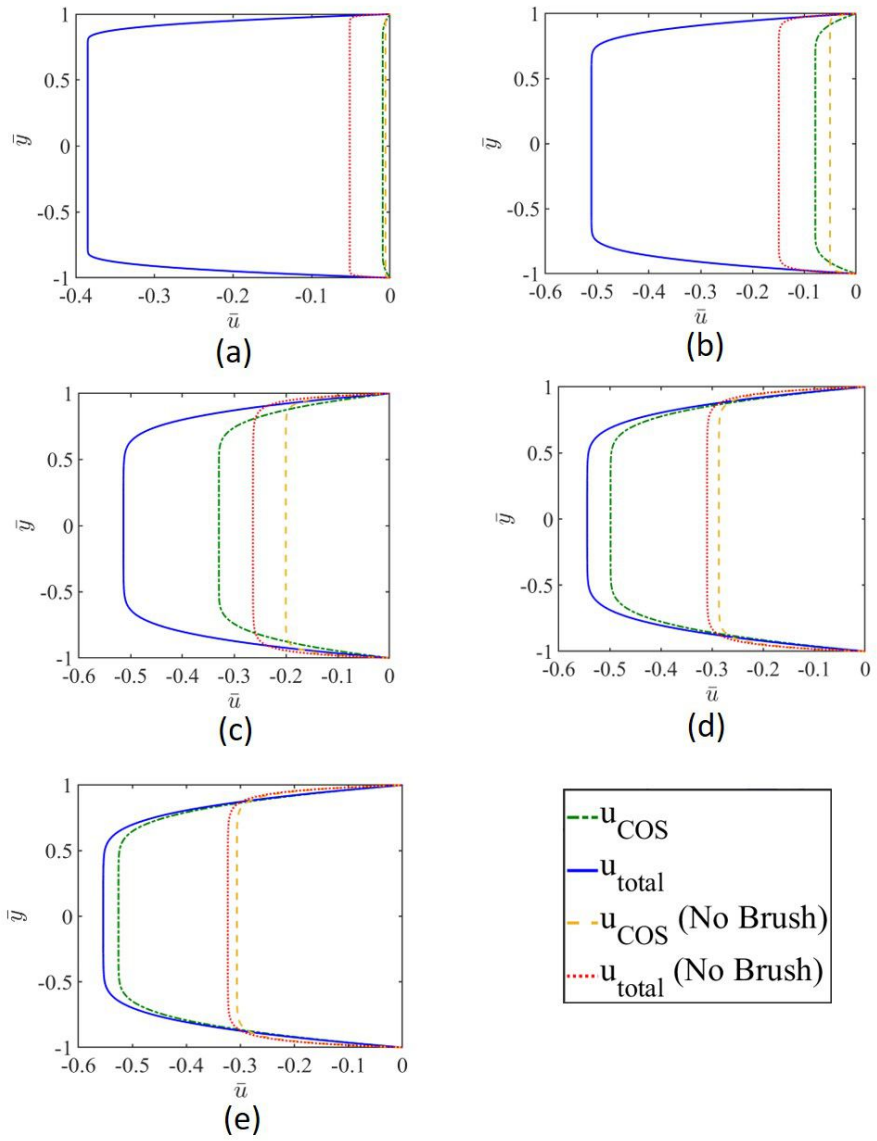


*Fig. 4.10:* DOS velocity field profiles (denoted as $u_{tot}$) and COS velocity profiles [obtained by solving eqs.(4.19) and (4.20)] in presence of an applied salt number density gradient of $\nabla n_\infty = dn_\infty/dx = 10^4 n_\infty$. for both brush-grafted and brush-free nanochannels for $pH_\infty = 3$, $\ell = 60\ nm$ for (a) $c_\infty = 10^{-1}\ M$, (b) $c_\infty = 10^{-2}\ M$, (c) $c_\infty = 10^{-3}\ M$, (d) $c_\infty = 10^{-4}\ M$, and (e) $c_\infty = 10^{-5}\ M$. Other parameters are identical to those used in Fig. 4.2.

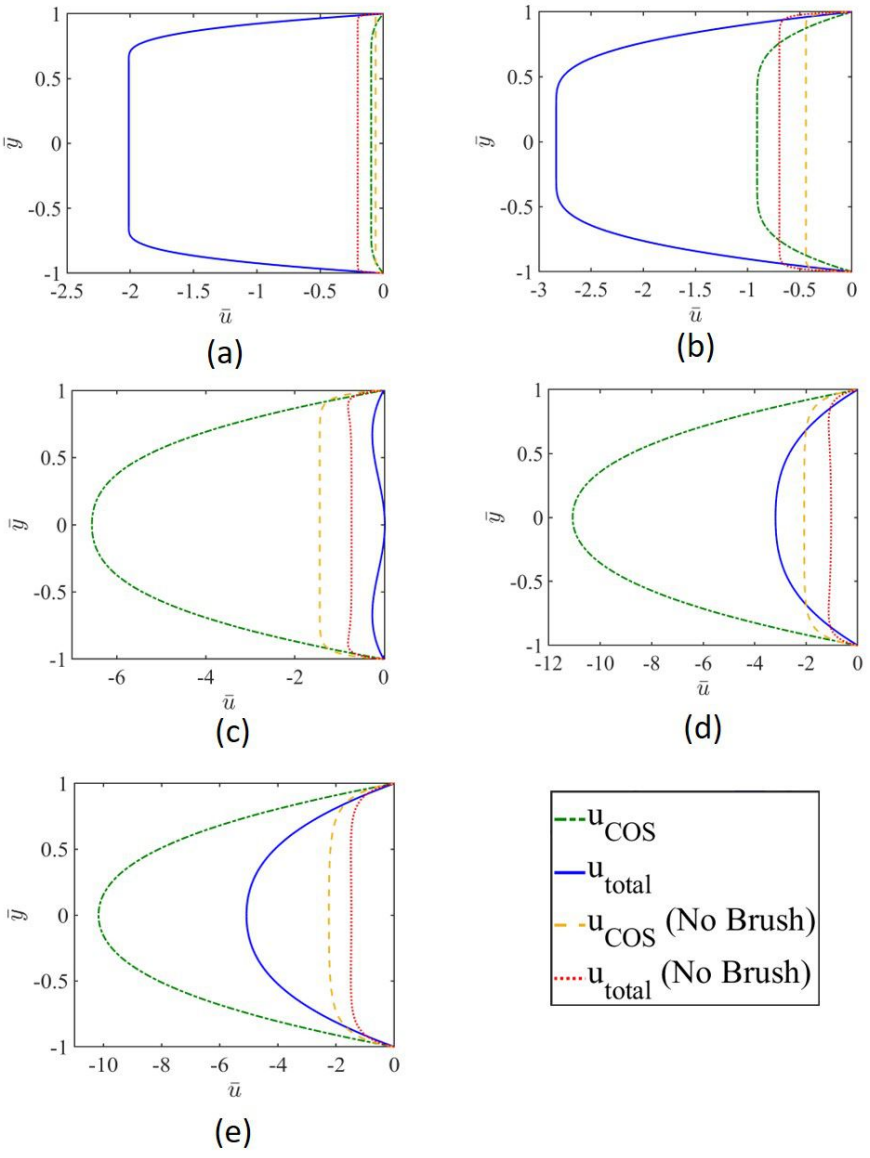


*Fig. 4.11:* DOS velocity field profiles (denoted as $u_{tot}$) and COS velocity profiles [obtained by solving eqs.(4.19) and (4.20)] in presence of an applied salt number density gradient of $\nabla n_\infty = dn_\infty/dx = 10^4 n_\infty$. for both brush-grafted and brush-free nanochannels for $pH_\infty = 4$, $\ell = 60\ nm$ for (a) $c_\infty = 10^{-1}\ M$, (b) $c_\infty = 10^{-2}\ M$, (c) $c_\infty = 10^{-3}\ M$, (d) $c_\infty = 10^{-4}\ M$, and (e) $c_\infty = 10^{-5}\ M$. Other parameters are identical to those used in Fig. 2.

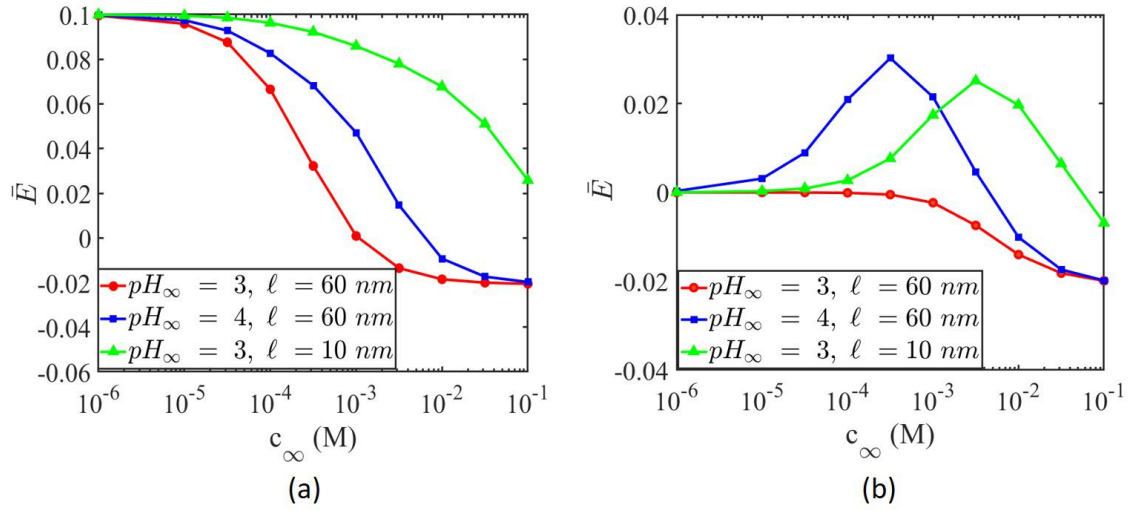


*Fig. 4.12:* Diffusioosmotically induced electric field for (a) End-charged PE brush and (b) Backbone charged PE brush. Parameters are identical to those used in Fig. 4.2.

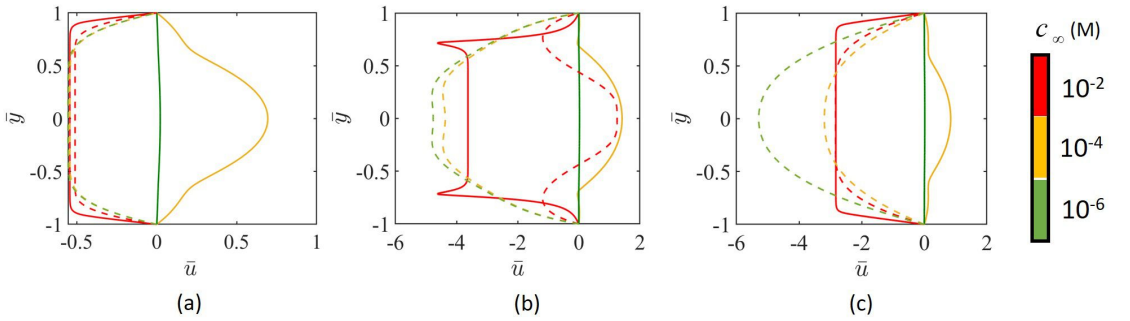


*Fig. 4.13:* Comparison of velocity field of End-charged and backbone charged PE brushes for (a) $pH_\infty = 3$, $\ell = 60$ nm, (b) $pH_\infty = 3$, $\ell = 10$ nm, and (c) $pH_\infty = 4$, $\ell = 60$ nm. The solid line represents end-charged PE brush and the dashed line represents the backbone charged PE brush. Other parameters are identical to those used in Fig. 4.2.

# Chapter 5: Conclusion and Future Scope

## *5.1 Conclusion*

In this thesis, we studied the effect of the PE brush functionalization on the electroosmotic and diffusioosmotic flow in nanochannel. Firstly, we described the modeling of the PE brush in a thermodynamically self-consistent fashion to obtain the equilibrium configuration of the brush. We obtain the brush height, monomer distribution, charge distribution through EDL potential from this framework. Using this description of the PE brush configuration and the brush-induced EDL, we model the electroosmotic transport of the liquid in nanochannels grafted with these PE brushes in the presence of the external axial electric field. The electric field induces a flow due to the EOS body force generated by the interaction of this electric field with the charge imbalance of the brush-induced EDL. We found that the presence of PE brush leads to enhanced liquid transport due to the localization of the EDL charge density and hence the localization of the EOS body force away from the wall where the drag force due to the wall is maximum. Following that we investigate the ionic diffusioosmotic flow in a PE brush grafted nanochannel. The difference in diffusivities in the ions combined with the presence of salt concentration gradient induces an electric field. This electric field results in a electroosmotic flow

and the salt concentration gradient induces a pressure gradient which leads to a chemiosmotic transport. Similarly, we find that the DOS transport is enhanced massively in the presence of PE brushes due to the localization of EDL, as explained above. It is found that both EOS and DOS flow velocity in nanochannel grafted with backbone charged PE brush modeled using augmented SST is much greater than that in nanochannel grafted with end-charged brush modeled using Alexander-de-Gennes model. The EOS body force is localized away from the wall for both the brush models, however the drag force due to brush is much greater for the Alexander-de-Gennes model near the location of the EOS body force. This results in much lesser net force at the location of EOS body force for this model resulting in smaller flow rate in comparison to augmented SST model.

## *5.2 Future Scope*

The present thesis sheds light on two interesting possibilities of significantly enhancing the water transport in nanochannels grafted with backbone-charged PE brushes. Future research endeavors should be directed in two distinct relevant areas. First, attempts should be made in developing experimental frameworks for studying such augmented nanofluidic transport in brush-grafted nanochannels. Various examples of charged PE brushes, such as poly(acrylic acid) brushes, poly(styrene sulfonate) brushes, etc. could be used for functionalizing the nanochannels. Second, detailed all-atom molecular dynamics (MD) simulations could be performed to study the liquid flows in such brush-grafted nanochannels. These simulations

would enable checking issues such as (a) the effect of possible deformation of the brushes due to the induced/applied electric fields and the induced flows, (b) the exact relationships of the grafting density to the brush-induced drag coefficients, etc. and the knowledge about these quantities would eventually ensure a much more rigorous continuum treatment of the fluid flows in nanochannels grafted with backbone-charged PE brushes.

## Bibliography


[1] S. Minko, in Polymer Surfaces and Interfaces, ed. M. Stamm, Springer, Berlin, Heidelberg, 2008, ch. 11, pp 215-234.

[2] Y. Uyama, K. Kato, Y. Ikada, in Grafting/Characterization Techniques/Kinetic Modeling, ed H. Galina et al., Advances in Polymer Science, vol. 137. Springer, Berlin, Heidelberg, 1998, pp 1-39

[3] S. Das, M. Banik, G. Chen, S. Sinha, and R. Mukherjee, Soft Matt., **11**, 8550 (2015).

[4] S. Alexander, J. Phys., **38**, 977 (1977).

[5] P.-G. de Gennes, J. Phys., **37**, 1443 (1976).

[6] P.-G. de Gennes, Macromolecules, **13**, 1069 (1980).

[7] R. R. Netz and D. Andelman, Phys. Rep. **380**, 1 (2003).

[8] S. T. Milner, Science **251**, 905 (1991).

[9] S. T. Milner, T. A. Witten and M. E. Cates, Europhys. Lett. **5**, 413 (1988).

[10] S. T. Milner, T. A. Witten and M. E. Cates, Macromolecules **21**, 610 (1988).

[11] A. M. Skvortsov, I. V. Pavlushkov, A. A. Gorbunov, Y. B. Zhulina, O. V. Borisov and V. A. Pryamitsyn, J. Polym. Sci., Part B: Polym. Phys. **30**, 1706 (1988).

[12] Y. B. Zhulina, V. A. Pryamitsyn and O. V. Borisov, Pol. Sci. U.S.S.R. **31**, 205 (1989).

[13] E. B. Zhulina, O. Borisov, V. A. Pryamitsyn and T. M. Birshtein, Macromolecules **24**, 140 (1991).

[14] W. Sparreboom, A. van den Berg, and J. C. Eijkel, New J. Phys. **12**, 015004 (2010).

[15] W. Sparreboom, A. van den Berg, and J. C. Eijkel, Nat. Nanotechnol., **4,** 713 (2009).

[16] E. N. Fung and E. S. Yeung, Anal. Chem. **67**, 1913 (1995).

[17] M. Monteferrante, L. Sola, M. Cretich, M. Chiari, U. Marini Bettolo Marconi, and S. Melchionna, J. Chem. Phys. **143**, 184907 (2015).

[18] R. Qiao, Langmuir **22**, 7096 (2006).

[19] S. P. Adiga and D. W. Brenner, Nano Lett. **5**, 2509 (2005).

[20] F. Tessier and G. W. Slater, Macromolecules **39**, 1250 (2006).

[21] G. Chen and S. Das, J. Phys. Chem. B **120**, 6848 (2016).

[22] G. Chen and S. Das, J. Appl. Phys. **117**, 185304 (2015).

[23] S. Chanda, S. Sinha, and S. Das, Soft Matt. **10**, 7558 (2014).

[24] G. Chen and S. Das, J. Colloid Interface Sci. **445**, 357 (2015).

[25] J. Patwary, G. Chen, and S. Das, Microfluid. Nanofluid. **20**, 37 (2016).

[26] A. Poddar, D. Maity, A. Bandopadhyay, and S. Chakraborty, Soft Matt. **12**, 5968 (2016).

[27] Z. Zeng, L. H. Yeh, M. Zhang, and S. Qian, Nanoscale **7**, 17020 (2015).

[28] Z. Milne, L. H. Yeh, T. H. Chou, and S. Qian, J. Phys. Chem. C **118**, 19806 (2014).

[29] L-H. Yeh, M. Zhang, S. Qian, J-P. Hsu, and S. Tseng, J. Phys. Chem. C **116**, 8672 (2012).

[30] G. Chen and S. Das, J. Phys. Chem. B **121**, 3130 (2017).

[31] R. S., Maheedhara, H. S., Sachar, H. Jing, and S. Das, J. Phys. Chemi. B **122**, 7450 (2018).

[32] R. S. Maheedhara, H. Jing, H. S. Sachar, and S. Das, Phys. Chem. Chem. Phys. **20**, 24300 (2018).

[33] G. W. de Groot, M. G. Santonicola, K. Sugihara, T. Zambelli, E. Reimhult, J. Voros, G. J. Vancso, ACS Appl. Mater. Interface. **5**, 1400 (2013).

[34] B. Yameen, M. Ali, R. Neumann, W. Ensinger, W. Knoll, O. Azzaroni, J. Am. Chem. Soc. **131**, 131, 2070 (2009).

[35] M. Ali, B. Yameen, R. Neumann, W. Ensinger, W. Knoll, O. Azzaroni, J. Am. Chem. Soc., **130**, 16351 (2008).

[36] M. Ali, B. Schiedt, R. Neumann, W. Ensinger,Macromol. Biosci. **10**, 28 (2010).

[37] S. Umehara, M. Karhanek, R. W. Davis, N. Pourmand, Proc. Natl. Acad. Sci. **106**, 4611 (2009).

[38] B. Vilozny, A. L. Wollenberg, P. Actis, D. Hwang, B. Singaram, N.; Pourmand, Nanoscale **5**, 9214 (2013).

[39] M. Ali, P. Ramirez, S. Mafe, R. Neumann, W. Ensinger, ACS Nano **3**, 603 (2009).

[40] M. Ali, B. Yameen, J. Cervera, P. Ramirez, R. Neumann, W. Ensinger, W. Knoll, J. Am. Chem. Soc. **132**, 8338 (2010).

[41] S. Moya, O. Azzaroni, T. Farhan, V. L. Osborne, W. T. S. Huck, Angewand. Chem. Int. Ed. **44**, 4578 (2005).

[42] B. Xin, J. Hao, Chem. Soc. Rev. **39**, 769 (2010).

[43] S. Mura, J. Nicolas, P. Couvreur, Nature Mater. **12**, 991 (2013).

[44] H. ShamsiJazeyi, C. A. Miller, J. S. Wong, J. M. Tour, R. Verduzco, J. Appl. Pol. Sci. **131**, 40576 (2014).

[45] E. B. Zhulina, O. V. Borisov, Langmuir **27**, 10615 (2011).

[46] G. Chen, S. Das, J. Phys. Chem. B **119**, 12714 (2015).

[47] G. Chen, S. Das, RSC Adv. **5**, 4493 (2015).

[48] P. A. Pincus, Macromolecules **24**, 2912 (1991).

[49] R. Ross, P. A. Pincus, Macromolecules **25**, 2177 (1992).

[50] O. V. Borisov, T. M. Birshtein, E. B. Zhulina, J. Phys. II **1**, 521 (1991).

[51] J. Wittmer, J. F. Joanny, Macromolecules **26**, 2691 (1993).

[52] O. V. Borisov, E. B. Zhulina, T. M. Birshtein, Macromolecules **27**, 4795 (1994).

[53] E. B. Zhulina, T. M. Birshtein, O. V. Borisov, Macromolecules **28**, 1491 (1995).

[54] E. B. Zhulina, M. Rubinstein, Soft Matt. **8**, 9376 (2012).

[55] R. Israëls, F. A. M. Leermakers, G. J. Fleer, E. B. Zhulina, Macromolecules **27**, 3249 (1994).

[56] S. Misra, S. Varanasi, P. P. Varanasi, Macromolecules **22**, 4173 (1989).

[57] G. Chen, H. S. Sachar, S. Das, Soft Matt. **14**, 5246 (2018).

[58] P. M. Biesheuvel, W. M. de Vos, V. M. Amoskov, Macromolecules **41**, 6254 (2008).

[59] E. B. Zhulina, O. V. Borisov, J. Chem. Phys. **107**, 5952 (1997).

[60] Y. V. Lyatskaya, F. A. M. Leermakers, G. J. Fleer, E. B. Zhulina, T. M. Birshtein, Macromolecules **28**, 3562 (1995).

[61] I. O. Lebedeva, E. B. Zhulina, O. V. Borisov, J. Chem. Phys. **146**, 214901 (2017).

[62] E. B. Zhulina, J. K. Wolterink, O. V. Borisov, Macromolecules **33**, 4945 (2000).

[63] J. P. Mahalik, Y. Yang, C. Deodhar, J. F. Ankner, B. S. Lokitz, S. M. Kilbey II, B. G. Sumpter, R. Kumar, J. Pol. Sci. B **54**, 956 (2016).

[64] T. Wu, P. Gong, I. Szleifer, P. Vlcek, V. Subr, J. Genzer, Macromolecules **40**, 8756 (2007).

[65] Y. Ito, Y. S. Park, Y. Imanishi, J. Am. Chem. Soc. **119**, 2739 (1997).

[66] D. Li, Q. He, Y. Yang, H. Möhwald, J. Li, Macromolecules **41**, 7254 (2008).

[67] M. Wang, S. Zou, G. Guerin, L. Shen, K. Deng, M. Jones, G. C. Walker, G. D. Scholes, M. A. Winnik, Macromolecules **41**, 6993 (2008).

[68] J. T. Murdoch, J. D. Willott, W. M. de Vos, A. Nelson, S. W. Prescott, E. J. Wanless, G. B. Webber, Macromolecules **49**, 9605 (2016).

[69] B. T. Cheesman, A. J. G. Neilson, J. D. Willott, G. B. Webber, S. Edmondson, E. J. Wanless, Langmuir **29**, 6131 (2013).

[70] J. D. Willott, T. J. Murdoch, B. A. Humphreys, S. Edmondson, E. J. Wanless, G. B. Webber, Langmuir **31**, 3707 (2015).

[71] E. B. Zhulina, V. A. Pryamitsyn, O. V. Borisov, Pol. Sci. USSR **1989**, 31, 205–216.

[72] J. D. Willott, T. J. Murdoch, F. A. M. Leermakers, W. M. de Vos, Macromolecules **51**, 1198 (2018).

[73] R. Hariharan, C. Biver, W. B. Russel, Macromolecules **31**, 7514 (1998).

[74] M .J. Uline, Y. Rabin, I. Szleifer, Langmuir **27**, 4679 (2011).

[75] G. S. Longo, M. O. de la Cruz, I. Szleifer, Macromolecules **44**, 147 (2011).

[76] S. Morochnik, R. J. Nap, G. A. Ameer, I. Szleifer, Soft Matt. **13**, 6332 (2017).

[77] G. S. Longo, I. Szleifer, J. Phys. D. Appl. Phys. **49**, 323001 (2016).

[78] F. M. Gilles, M. Tagliazucchi, O. Azzaroni, I. Szleifer, J. Phys. Chem. C **120**, 4789 (2016).

[79] E. B. Zhulina, M. Rubinstein, Macromolecules **47** , 5825 (2014).

[80] N. A. Kumar, C. Seidel, Macromolecules **38**, 9348 (2005).

[81] A. Naji, R. R. Netz, C. Seidel, Eur. Phys. J. E **12**, 223 (2003).

[82] B. Niu, K. Xiao, X. Huang, Z. Zhang, X-Y. Kong, Z.; Wang, L. Wen, L. Jiang, ACS Appl. Mater. Interfaces **10**, 22632 (2018).

[83] M. Liu, H. Zhang, K. Li, L. Heng, S. Wang, Y. Tian, L. Jian, Adv. Func. Mater. **25**, 421 (2015).

[84] L. G. Lopez, R. J. Nap, Phys. Chem. Chem. Phys. **20**, 16657 (2018).

[85] M. Zhang, X. Hou, J. Wang, Y. Tian, X. Fan, J. Zhai, L. Jiang, Adv. Mater. **24**, 2424 (2012).

[86] O. Azzaroni, A. A. Brown, W. T. S. Huck, Adv. Mater. **19**,151 (2007).

[87] G. Chen, J. Patwary, H. S. Sachar, S. Das, Microfluid. Nanofluid. **22**,112 (2018).

[88] H. Li, G. Chen, S. Das, Colloid. Surf. B **147**, 180 (2016).

[89] M. Motornov, T. K. Tam, M. Pita, I. Tokarev, E. Katz, S. Minko, Nanotechnology **20**, 434006 (2009).

[90] S. Wang, K. Chen, L. Li, X. Guo, Biomacromolecules **14**, 818 (2013).

[91] Y. Zhu, K. Chen, X. Wang, X. Guo, Nanotechnology **23**, 265601 (2012).

[92] R. Kumar, B. G. Sumpter, S. M. Kilbey, J. Chem. Phys. **136**, 234901 (2012).

[93] A. Deshkovski, S. Obukhov, M. Rubinstein, Phys. Rev. Lett. **86**, 2341 (2001).

[94] M. S. Kilic, M. Z. Bazant, A. Ajdari, Phys. Rev. E **75**, 021502 (2007).

[95] S. Chanda, S. Das, Phys. Rev. E **89**, 012307 (2014).

[96] R. P. Misra, S. Das, S. K. Mitra, J. Chem. Phys. **138**, 114703 (2013).

[97] B. D. Storey, M. Z. Bazant, Phys. Rev. E **86**, 056303 (2012).

[98] V. S. Rathee, B. J. Sikora, H. Sidky, J. K. Whitmer, Mater. Res. Exp. **5**, 014010 (2018).

[99] A. Alexander-Katz, A. G. Moreira, G. H. Fredrickson, J. Chem. Phys. **118**, 9030 (2003).

[100] C. Deodhar, E. Soto-Cantu, D. Uhrig, P. Bonnesen, B. S. Lokitz, J. F. Ankner, S. M. Kilbey, ACS Macro Lett. **2**, 398 (2013) .

[101] M. Moglianetti, J. R. Webster, S. Edmondson, S. P. Armes, S. Titmuss, Langmuir **26**, 12684 (2010).

[102] J. Gao *et al.*, Chem. Soc. Rev. **46**, 5400 (2017).

[103] J. C. T. Eijkel and A. van den Berg, Microfluid. Nanofluid. **1**, 249 (2005).

[104] A. R. Koltonow and J. X. Huang, Science **351**, 1395 (2016).

[105] Y. Zhu, K. Zhan, and X. Zhu, ACS Nano **12**, 908 (2018).

[106] R. Li *et al.*, Adv. Mater. **29**, 1702983 (2017).

[107] B. M. Venkatesan and R. Bashir, Nat. Nanotechnol. **6**, 615 (2011).

[108] B. N. Miles *et al.*, Chem. Soc. Rev. **42**, 15 (2013).

[109] R. C. Fang *et al.*, J. Am. Chem. Soc. **138**, 16372 (2016).

[110] X. Huang *et al.*, Adv. Funct. Mater. **28**, 1801079 (2018).

[111] Z. Zhang, L. P. Wen, and L. Jiang, Chem. Soc. Rev. **47**, 322 (2018).

[112] M. Ali *et al.*, Anal. Chem. **83**, 1673 (2011).

[113] M. Ali *et al.*, J. Phys. Chem. C **117**, 18234 (2013).

[114] B. Yameen *et al.*, Chem. Comm. **46**, 1908 (2010).

[115] G. J. M. Bruin, J. P. Chang, R. H. Kuhlman, K. J. C. K. Zegers, J. C. Kraak, and H. Poppe, J. Chromatogr. A **471**, 429 (1989).

[116] Z. Zhang, C. Zuo, Q. Cao, Y. Ma, and S. Chen, Macromol. Theory Simul. **21**, 145 (2012).

[117] Y. Zuo, G. Wang, Y. Yu, C. Zuo, Z. Liu, D. Hu, and Y. Wang, Microfluid. Nanofluid. **17**, 923 (2014).

[118] H. S. Sachar, V. S. Sivasankar, and S. Das, Soft Matt. **15**, 559 (2019).

[119] H. S. Sachar, V. S. Sivasankar, and S. Das, Soft Matt. **15**, 5973 (2019).

[120] Pennathur, S. and Santiago, J. G. Anal. Chem. **77**, 6782-6789 (2005).

[121] J. Y. Chong, B. Wang, and K. Li, Chem. Comm. **54**, 2554 (2018).

[122] K.-G. Zhou *et al.*, Nature **559**, 236 (2018).

[123] J. Y. Chong *et al.*, J. Mem. Sci. **549**, 385 (2018).

[124] H. Liu, H. Wang, and X. Zhang, Adv. Mater. **27**, 249 (2015).

[125] Y. Han, Y. Jiang, and C. Gao, ACS Appl. Mater. Interface. **7**, 8147 (2015).

[126] H. Huang *et al.*, Nature Comm. **4**, 2979 (2013).

[127] Q. Yang *et al.*, Nature Mater. **16**, 1198 (2017).

[128] C. Y. Tang *et al.*, Heliyon **5**, e01142 (2019).

[129] C. Chen *et al.*, Nature Comm. **9**, 1902 (2018).

[130] M. Yang *et al.*, RSC Adv. **4**, 26729 (2014).

[131] X. Peng *et al.*, Nat. Nanotechnol. **4**, 353 (2009).

[132] K. P. Lee, H. Leese, and D. Mattia, Nanoscale **4**, 2621 (2012).

[133] M. Whitby *et al.*, Nano Lett. **8**, 2632 (2008).

[134] K. Mathwig *et al.*, Phys. Rev. Lett. **109**, 118302 (2012).

[135] C. Lee *et al.*, Phys. Rev. Lett. **112**, 244501 (2014).

[136] S. P. Surwade*et al.*, Nat. Nanotechnol. **10**, 459 (2015).

[137] M. Majumder *et al.*, Nature **438**, 44 (2005).

[138] P. G. de Gennes, Macromolecules **9**, 594 (1976).

[139] K. F. Freed and S. F. Edwards, J. Chem. Phys. **61**, 3626 (1974).

[140] Z. Zhu, D. Wang, Y. Tian, and L. Jiang. J. Am. Chem. Soc. **141**, 8658 (2019).

[141] A. Ziemys, M. Kojic, M. Milosevic, and M. Ferrari, Phys. Rev. Lett. **108**, 236102 (2012).

[142] K. M. Weerakoon-Ratnayake, C. E. O'Neil, F. I. Uba, and S A. Soper, Lab Chip **17**, 362 (2017).

[143] R. L. Hood G. D. Hood M. Ferrari, and A. Grattoni, WIRE Nanomed. Nanobiotechnol. **9**, e1455 (2017).

[144] S. Bhattacharya, and N. Bag, Phys. Fluids **31**, 072007 (2019).

[145] R. Sarma *et al.*, Phys. Fluids, **30**, 062001 (2018).

[146] M. Sadeghi, M. H. Saidi, and A. Sadeghi, Phys. Fluids, **29** , 062002 (2017).

[147] J-Y. Lin, C-Y. Lin, J-P. Hsu, and S, Tseng, Anal. Chem. **88**, 1176 (2016).

[148] A. Sadeghi, Phys. Fluids, **30**, 032004 (2018).

[149] K. Binder, A. Milchev and J. Baschnagel, Annu. Rev. Mater. Sci. **26**, 107 (1996).

[150] O. Azzaroni, J. Polym. Sci. **50**, 3225 (2012).

[151] Y. Jian, F. Li, Y. Liu, L. Chang, Q. Liu and L. Yang, Colloid. Surf. B **156**, 405 (2017).

[152] L.-H. Yeh, M. Zhang, N. Hu, S. W. Joo, S. Qian and J.-P. Hsu, Nanoscale **4**, 5169 (2012).

[153] L.-H. Yeh, M. Zhang, N. Hu, S. W. Joo, S. Qian and J.-P. Hsu, Anal. Chem. **84**, 9615 (2012).

[154] L. Benson, L.-H. Yeh, T.-H. Chou and S. Qian, Soft Matter **9**, 9767 (2013).

[155] C. Zhou, L. Mei, Y.-S. Su, L.-H. Yeh, X. Zhang and S. Qian, Sens. Actuators B **229**, 305 (2016).

[156] F. Li, Y. Jian, L. Chang, G. Zhao and L. Yang, Colloid. Surf. B **147**, 234 (2016).

[157] Q. Cao and H. You, Polymers **8**, 438 (2016).

[158] F. Li, Y. Jian, Z. Xie, Y. Liu and Q. Liu, RSC Adv. **7**, 782 (2017).

[159] J.-S. Sin and U.-H. Kim, Phys. Chem. Chem. Phys. **20**, 22961 (2018).

[160] H. S. Sachar, V. S. Sivasankar, S. A. Etha, G. Chen, and S. Das, Electrophoresis $DOI$ : 10.1002/$elps$.201900248 (2019).

[161] H. J. Keh, Curr. Opin. Colloid Interface Sci. **24**, 13 (2016).

[162] H. J. Keh and H. C. Ma, Langmuir **21**, 5461 (2005).

[163] L. Y. Hsu, and H. J. Keh, Ind. Eng. Chem. Res. **48**, 2443 (2009).

[164] H. C. Ma and H. J. Keh, J. Colloid Interface Sci. **298**, 476 (2006).

[165] H. C. Ma and H. J. Keh, J. Colloid Interface Sci. **313**, 686 (2007).

[166] S. Qian, B. Das, and X. Luo, J. Colloid Interface Sci. **315**, 721 (2007).

[167] H. J. Keh and H. C. Ma, Colloids Surf. A **233**, 87 (2004).

[168] V. Hoshyargar and S. N. Ashrafizadeh, Phys. Chem. Chem. Phys. **17**, 29193 (2015).

[169] V. Hoshyargar, S. N. Ashrazadeh, and A. Sadeghi, Electrophoresis **37**, 809 (2015).

[170] H. J. Keh and H. C. Ma, Langmuir **23**, 2879 (2007).

[171] I. Cho, W. Kim, J. Kim, H.-Y. Kim, H. Lee, and S. J. Kim, Phys. Rev. Lett. **116**, 254501 (2016).

[172] H. J. Keh and L. Y. Hsu, Microfluid. Nanofluid. **5**, 347 (2008).

[173] J. L. Anderson, M. E. Lowell, and D. C. Prieve, J. Fluid Mech. **117**, 107 (1982).

[174] C. Lee, C. Cottin-Bizonne, R. Fulcrand, L. Joly, and C. Ybert, J. Phys. Chem. Lett. **8**, 478 (2017).

[175] M. Shen, F. Ye, R. Liu, K. Chen, M. Yang, and M. Ripoll, J. Chem. Phys. **145**, 124119 (2016).

[176] S. Marbach, H. Yoshida, and L. Bocquet, J. Chem. Phys. **146**, 194701 (2017).

[177] H. Yoshida, S. Marbach, and Bocquet, J. Chem. Phys. **146**, 194702 (2017).

[178] A. Ajdari and L. Bocquet, Phys. Rev. Lett. **96**, 186102 (2006).

[179] I. Ortiz-Rivera, H. Shum, A. Agrawal, A. Sen, and A. C. Balazs, Proc. Natl. Acad. Sci. U. S. A. **113**, 2585 (2016).

[180] V. Hoshyargar, S. N. Ashrafizadeh, and A. Sadeghi, Phys. Fluid. **29**, 012001 (2017).

[181] D. Feldmann, S. R. Maduar, M. Santer, N. Lomadze, O. I. Vinogradova, and S. Santer, Sci. Rep. **6**, 36443 (2016).

[182] R. J. Gross and H. J. Osterle, J. Chem. Phys. **49**, 228 (1968).

[183] P. B. Peters, R. van Roij, M. Z. Bazant, and P. M. Biesheuvel, Phys. Rev. E **93**, 053108 (2016).

[184] I. I. Ryzhkov, D. V. Lebedev, V. S. Solodovnichenko, A. V. Shiverskiy, and M. M. Simunin, M. M. Phys. Rev. Lett. **119**, 226001 (2017).

[185] I. I. Ryzhkov, D. V. Lebedev, V. S. Solodovnichenko, A. V. Minakov, and M. M. Simunin, J. Mem. Sci. **549**, 616 (2018).

[186] W. M. Haynes, CRC Handbook of Chemistry and Physics 93rd Edition, 2012. Chemical Rubber Company.

[187] H. Jing and S. Das, Phys. Chem. Chem. Phys. **20**, 10204 (2018).